A molecular switch between mammalian MLL complexes dictates response to Menin-MLL inhibition

Yadira M. Soto-Feliciano[1, †], Francisco J. Sánchez-Rivera[2, †], Florian Perner[3,4,5, †], Douglas W. Barrows[1,6], Edward R. Kastenhuber[2], Yu-Jui Ho[2], Thomas Carroll[6], Yijun Xiong[3,4], Alexey Soshnev[1], Leah Gates[1], Mary Clare Beytagh[1], David Cheon[1], Shengqing Gu[7,8], X. Shirley Liu[7,8], Andrei V. Krivtsov[3,4], Maximiliano Meneses[9], Elisa de Stanchina[9], Richard M. Stone[10], Scott A. Armstrong[3,4, *], Scott W. Lowe[2, *], C. David Allis[1, *]

[1]Laboratory of Chromatin Biology & Epigenetics, The Rockefeller University, New York, NY 10065, USA.

[2]Cancer Biology and Genetics, MSKCC New York, NY 10065, USA.

[3]Department of Pediatric Oncology, Dana-Farber Cancer Institute, Boston, MA., 02215, USA.

[4]Division of Hematology/Oncology, Boston Children's Hospital and Harvard Medical School, Boston, MA, 02215, USA.

[5]Internal Medicine C, Greifswald University Medical Center, Greifswald, 17475, Germany.

[6]Bioinformatics Resource Center, The Rockefeller University, New York, NY 10065, USA.

[7]Department of Biostatistics and Computational Biology, Dana-Farber Cancer Institute, Harvard School of Public Health, Boston, 02215, MA, USA.

[8]Center for Functional Cancer Epigenetics, Dana-Farber Cancer Institute, Boston, 02215, MA, USA.

[9]Department of Molecular Pharmacology, MSKCC New York, NY 10065, USA.

[10]Leukemia Division, Department of Medical Oncology, Dana-Farber Cancer Institute, Boston, MA, 02215, USA.

† Co-first authors

* Co-corresponding authors

Correspondence:

C. David Allis: The Rockefeller University, Allis Lab, Box #78, 1230 York Avenue, New York, NY 10065, USA. Email: alliscd@rockefeller.edu

Scott W. Lowe: Memorial Sloan Kettering Cancer Center (MSKCC), Sloan Kettering Institute, Cancer Biology & Genetics Program, New York, NY, 10065, USA. Email: lowes@mskcc.org

Scott A. Armstrong: Harvard Medical School, Dana-Farber Cancer Institute, Department of Pediatric Oncology, Boston, MA, 02115, USA. Email: Scott_Armstrong@dfci.harvard.edu

Keywords: Menin, MLL, UTX, chromatin, epigenetics, leukemia, CRISPR

ABSTRACT

The chromatin adaptor Menin interacts with oncogenic fusion proteins encoded by *MLL1*-rearrangements (*MLL1*-r), and small molecules that disrupt these associations are currently in clinical trials for the treatment of leukemia. Here, we delineate a molecular switch between the MLL1-Menin and MLL3/4-UTX chromatin modifying complexes that dictates response to Menin-MLL inhibitors. We show that Menin safeguards leukemia cell fitness by impeding binding of the histone demethylase UTX at a subset of non-canonical target gene promoters. Disrupting the interaction between Menin and MLL1 leads to UTX-dependent transcriptional activation of genes with tumor suppressive function. We show that this epigenetic mechanism is operative in murine and human models of AML, and clinical responses to Menin-MLL inhibition in primary human leukemia are accompanied by induction of tumor suppressive gene expression at Menin-UTX targets. These findings shed light on the context-dependent and often antagonistic roles that chromatin regulators exhibit in development and disease and provide mechanistic insight for rational design of targeted epigenetic therapies.

INTRODUCTION

Menin is an evolutionarily conserved nuclear factor that associates with chromatin to recruit (adapt) interacting proteins[1], including the Trithorax (*Trx*)-related MLL1 (KMT2A) and MLL2 (KMT2B) histone methyltransferase complexes[2, 3] and the MLL1 oncogenic fusion proteins[4], transcription factors (e.g., c-MYC[5], JUND[6, 7], SMADs[8, 9]), and other chromatin-bound proteins (e.g. LEDGF[10] (reviewed in ref. 11)). However, the detailed underlying molecular mechanisms and functional interactions associated with Menin remain elusive.

Menin is a core subunit of the MLL1 (ref. 12) and MLL2 complexes[2] and is responsible for targeting these to chromatin[3]. Menin is required for MLL1/MLL2-dependent H3K4 trimethylation of *HOX*

genes and their stable long-term expression during development[2, 13]. Menin has context-specific functions in human diseases, acting as a tumor suppressor in neuroendocrine malignancies[14, 15] and in certain skin[16], lung[17], and CNS tumors[18], and as an oncogenic cofactor in other cancers, including hepatocellular carcinoma[19] and *MLL1*-rearranged (*MLL1*-r) leukemias[4, 20]. Furthermore, over 1000 germline and somatic *MEN1* variants have been identified, some of which are linked to cancer predisposition[21]. Owing to its pro-oncogenic roles in mixed lineage leukemia and other malignancies, small molecule inhibitors targeting the Menin-MLL1 and Menin-MLL2 protein-protein interactions have shown great promise for intercepting and treating different types of cancers[19, 22-27]. Notably, three structurally different Menin-MLL inhibitors have recently entered clinical trials (NCT04065399, NCT04067336, NCT04811560) and at least one has been granted fast track designation by the FDA for treatment of relapsed/refractory acute leukemias[26-28]. Thus, an understanding of the molecular mechanisms of action of these drugs would facilitate the development of biomarkers to predict therapeutic response and resistance and lead to rational design of more effective combination treatments.

RESULTS

Functional interplay between MLL1-Menin and MLL3/4-UTX chromatin modifying complexes

We performed a series of CRISPR-based genetic screens to molecularly dissect the dependency of *MLL1*-r leukemias to Menin and identify factors that dictate response and resistance to Menin inhibitors (see Methods). First, we screened a chromatin-focused CRISPR library in Cas9-expressing Menin-dependent mouse leukemia cells driven by a human MLL-AF9 transgene (hereafter referred to as MLL-AF9 cells)[29] (**Fig.1A, Extended Fig. 1A-D, Supplementary Table 1**). Library-transduced cells were cultured in media with DMSO (vehicle) or the Menin-MLL inhibitor MI-503 (ref. 23) for 12 cell population doublings (CPDs), followed by screen

deconvolution using next-generation sequencing (**Fig.1A**, **Extended Fig. 1E-F**). A gene score (mean $\log_2$ fold-change) was calculated for each gene included in the library by assessing the change in abundance of sgRNAs during the culture period (**Fig.1B**). As expected, sgRNAs targeting known *MLL1*-r leukemia dependencies, such as *Dot1l* (refs. 29-32), *Brd4* (ref. 33), and *Myb* (ref. 34) were strongly depleted in both treatments while control sgRNAs remained largely neutral, thereby validating our screening platform (**Supplementary Table 2**).

Among the sgRNAs that were enriched or depleted in the absence and presence of drug, sgRNAs targeting the histone H3 lysine 27 (H3K27) demethylase *Utx* (*Kdm6a*) and the histone H3 lysine 4 (H3K4) mono-methyltransferases *Mll3* (*Kmt2c*) and *Mll4* (*Kmt2d*) were the most enriched in the Menin-MLL inhibitor context (**Fig.1B**, red circles). This result was unexpected, since the canonical activity of the MLL1/2-Menin complex (disrupted by MI-503) is to catalyze the di/tri-methylation of H3K4 (H3K4me2/3) at *promoters*, resulting in loading of the transcriptional machinery at such sites[13, 35, 36], while the MLL3/4-UTX complex regulates *enhancer* states by serving as the major H3K4 mono-methyltransferase (H3K4me1) (refs. 37-41).

To assess whether these results were idiosyncratic of the cell line, library, or inhibitor used, we performed a genome-wide CRISPR screen in an independently derived MLL-AF9 cell line using VTP-50469, a more potent, selective, and orally bioavailable Menin-MLL inhibitor that led to the development of SNDX-5613, which is currently under investigation in a phase 1/2 clinical trial for treatment of relapsed/refractory acute leukemia (NCT04065399) (refs. 26-28). Remarkably, sgRNAs targeting *Utx* (*Kdm6a*), *Mll3* (*Kmt2c*), and *Mll4* (*Kmt2d*) were also among the most significantly enriched candidate genes identified in this genome-wide screen (**Fig.1C, Extended Fig. 2A-C, Supplementary Table 2**). Interestingly, shared subunits between the two types of MLL complexes scored similarly in both vehicle and Menin-MLL inhibitor conditions (**Fig.1B-D, Extended Fig. 1G, Extended Fig. 2D**). This suggests that core subunits of the MLL3/4-UTX complex[42] modulate therapeutic responses to Menin-MLL inhibition and have context-specific

tumor suppressive functions[43, 44], a result that is consistent with their haploinsufficient tumor suppressor activity in some cancers[45].

Utx or *Mll3* loss-of-function did not affect cell proliferation *in vitro*, while *Mll4* inactivation decreased cell growth, consistent with previous work[43] (**Extended Fig. 3A-D**). However, in agreement with our screening results, *Utx* disruption using three distinct sgRNAs significantly increased the viability of MI-503-treated leukemia cells, confirming that inactivation of *Utx* confers resistance to Menin-MLL inhibition (**Fig.1E, Extended Fig. 3E**). In addition, *Mll3*- and *Mll4*-deficient cells treated with MI-503 exhibited a proliferative advantage over wild-type cells only in the treatment context (**Extended Fig. 3F-G**). These orthogonal results establish the MLL3/4-UTX complex as a central modulator of therapy response to Menin-MLL inhibition.

UTX was among the most significantly enriched chromatin factors in our screen (**Fig.1B-C, Extended Fig. 1G, Extended Fig. 2D**). As this factor is shared by both MLL3 and MLL4 complexes[40, 46, 47], we focused on UTX disruption to functionally probe the molecular mechanisms linked to resistance to Menin inhibition. We first tested whether genetic *Utx* inactivation could rescue the effects of Menin-specific ablation in MLL-AF9 leukemia cells. While CRISPR-mediated deletion of *Men1* led to robust inhibition of proliferation (**Extended Fig. 4A**), co-deletion of *Utx* suppressed this phenotype, such that *Men1*-deficient MLL-AF9 cells were able to robustly proliferate (**Fig.1F, Extended Fig. 4B-C**). Importantly, deletion of *Utx*, *Mll3*, or *Mll4* in isolation did not confer any significant fitness advantage to cells, further validating our findings obtained with pharmacologic inhibition of Menin-MLL (**Extended Fig. 3**).

To determine if the genetic interaction between Menin and UTX depends on the MLL-fusion protein (MLL-FP), we ablated the human *MLL1-AF9* transgene expressed in MLL-AF9 leukemia cells using sgRNAs selectively targeting exons 3 or 5 of the human *MLL1* gene (preceding the breakpoint cluster region (exons 9-11) in *MLL1*-translocations)[48, 49] (**Extended Fig. 5A**). Cells

deficient for *MLL-AF9* and *Utx* are equally unfit to cells lacking *MLL-AF9*, validating the exquisite dependency of leukemia cells to the pleiotropic gene regulatory activity of this oncogenic fusion (*20*) (**Extended Fig. 5B-C**). However, MLL-AF9 leukemia cells deficient for *Men1* and *Utx*, or those deficient for *Utx* and treated with Menin-MLL inhibitor, are able to proliferate without reactivation of canonical fusion targets like *Meis1* (ref. 27), (**Extended Fig. 6**) demonstrating that this genetic interaction is not entirely dependent on the oncogenic activity of this fusion. Similarly, co-deletion of *UTX* and *MEN1* in a Menin-dependent non *MLL1*-r human leukemia cell line driven by *DNMT3A* and *NPM1* mutations[50, 51] also rescued the decreased fitness associated with loss of *MEN1* alone (**Extended Fig. 5D-E**), suggesting that the functional Menin-UTX interactions observed in our models are conserved in human cells. Similar results were obtained in non *MLL1*-r AML1-ETO9a mouse leukemia cells treated with MI-503 (**Extended Fig. 5F-G**). These data suggest that the phenotype of Menin-MLL inhibition is evolutionarily conserved and acts in part through a pathway that involves crosstalk between Menin and UTX and is downstream or independent of MLL-FPs.

Menin is needed for expression of canonical MLL-FP target genes, such as *Meis1*, whose function is required for leukemia maintenance[26, 35, 36, 52, 53], and *Meis1* over-expression was recently shown to partially rescue the leukemic stem cell transcriptional program suppressed by Menin-MLL inhibition[27]. We confirmed that treatment of mouse MLL-AF9 leukemia cells with MI-503 led to robust downregulation of *Meis1* (**Extended Fig. 6A**). However, to our surprise, cells genetically deficient for both *Men1* and *Utx* showed a similar reduction in *Meis1* levels (**Extended Fig. 6B**), yet were able to proliferate *in vitro* (**Fig.1F, Extended Fig. 4B**). We further confirmed these findings in an additional Menin-dependent mouse MLL-AF9 cell line (**Extended Fig. 6C-D**) and a human MLL-AF4-driven leukemia line[54] (**Extended Fig. 6E-F**). These experiments reveal an epistatic relationship between Menin and UTX in Menin-dependent mammalian cells and

suggest that factors beyond *Meis1* can sustain the proliferative potential of *MLL1*-r and non *MLL1*-r leukemia cells.

Menin and NF-Y restrict chromatin occupancy of UTX at promoter regions

Menin is generally associated with chromatin-modifying and transcriptional complexes at promoter regions[6, 55], while UTX canonically resides in complexes that regulate enhancers[40]. To determine the genomic distribution of Menin and UTX in the absence or presence of the Menin-MLL inhibitor, we performed chromatin immunoprecipitation followed by sequencing (ChIP-Seq). Menin showed strong enrichment at promoter regions (here defined as transcription start sites (TSSs) ± 2kb), which was substantially decreased when its canonical interactions with MLL1/2 were disrupted by MI-503 (**Fig.2A**). Genome-wide enrichment of Menin was also decreased, as evidenced by a >10-fold reduction in the number of ChIP peaks post MI-503 treatment (**Extended Fig. 7A**). Conversely, while only a very minor fraction of UTX appeared to be enriched on chromatin at basal conditions, the genome-wide enrichment of UTX dramatically increased upon treatment with MI-503, as evidenced by a ~70-fold increase in the number of peaks (**Extended Fig. 7A**). UTX canonically resides in complexes that regulate enhancers[40, 41] yet, contrary to expectation, more than 70% of UTX binding peaks in MI-503 treated cells were localized at promoters and proximal regions (**Fig.2B, Extended Fig. 7A**)[56]. Importantly, the enhanced enrichment of UTX on chromatin was not merely the result of increased expression and/or protein stability (**Fig.2C-D**). These data show that disruption of the Menin-MLL1/2 interaction leads to dynamic and robust recruitment of UTX to promoter regions (**Fig.2B**), suggesting a previously unrecognized role for the core MLL3/4-UTX complex in promoter regulation and gene transcription[41].

Not only did Menin depletion lead to recruitment of UTX to promoter regions, the loci that accumulated UTX significantly overlapped with those where Menin was lost (**Fig.2E-F**, **Extended**

Fig. 7B). Specifically, correlation analysis suggested that reduction of Menin binding by MI-503 coincided with increased UTX chromatin occupancy at the same genomic loci (*Pearson coefficient (r)* = -0.49) (**Fig.2G**). This molecular switch was specific to Menin-dependent cells, as MI-503 treatment of Menin-independent mouse fibroblasts did not lead to UTX redistribution to promoters (**Extended Fig. 8A-E**). Therefore, Menin excludes UTX from binding to promoters in Menin-dependent cell types, and this antagonism can be reversed by MI-503-mediated displacement of Menin-MLL1/2 complexes from chromatin.

Given that Menin lacks a defined DNA binding domain[57], we hypothesized that a sequence-specific DNA binding factor regulates the switch between Menin and UTX occupancy at specific promoters. To test this hypothesis, we performed motif analysis on genomic regions bound by Menin and UTX, uncovering NF-Y sequence motifs[58] as the most significantly enriched (P=1e^{-130}) (**Extended Fig. 9A**). These motifs were specific to leukemia cells, as motif enrichment analysis identified a different subset of sequences in mouse fibroblasts (**Extended Fig. 9B-C**). ChIP-Seq of NF-YA (the DNA binding and transactivation subunit of the NF-Y complex[58]) confirmed these observations, showing that NF-YA co-occupies sites bound by Menin and UTX (**Extended Fig. 9D-E**). Consistent with our hypothesis, sites bound by UTX in the context of Menin-MLL inhibition also had lower NF-YA occupancy (**Extended Fig. 9D-E**), which was not due to decreased protein levels (**Extended Fig. 9F**). Moreover, CRISPR-mediated disruption of *Nfya* in MLL-AF9 leukemia cells significantly decreased the viability of MI-503-treated leukemia cells relative to control cells (**Extended Fig. 10A-C**). This observation led us to hypothesize that NF-YA depletion could lead to a concomitant decrease of Menin and increase of UTX occupancy at target genomic regions. Supporting this model, treatment of *Nfya*^{KO} cells with MI-503 led to a substantial increase in UTX occupancy at genomic regions normally bound by Menin and NF-Y at steady-state (**Extended Fig. 10D-F**). These results are also consistent with co-essentiality analyses in human cells[59] showing that a subset of *MEN1*-dependent cells are co-dependent on members of the NF-Y

complex for survival (**Extended Fig. 10G-J)**. Collectively, these results implicate NF-Y in restricting the occupancy of UTX at promoter regions and further suggest that Menin binding to these sites is mediated by the sequence-specific DNA binding activity of the NF-Y transcription factor.

Promoter regulation by the MLL3/4 complex dictates outcome of Menin inhibition

Inhibition of Menin-MLL1 leads to displacement of this complex from gene promoters, allowing UTX to bind and potentially regulate target gene expression (**Fig.2**). To further understand the molecular switch between Menin and UTX at promoters, we examined the chromatin-binding profiles of their cognate H3K4 methyltransferases and their enzymatic histone modifications (MLL1 and H3K4me3 for Menin, and MLL3/4 and H3K4me1 for UTX) (**Fig.3A-B**). Disruption of the Menin-MLL1 interaction led to a substantial decrease in MLL1 chromatin binding and a concomitant decrease of its enzymatic product, H3K4me3, (**Fig.3C**, **Extended Fig. 11A-B**). In contrast, Menin-MLL1 inhibition led to increased binding of the MLL3/4 enzymes at promoter regions co-occupied by UTX and a concomitant increase in H3K4me1 signal at these same loci (**Fig.3D**, **Extended Fig. 11C-D**). These data suggest that disruption of the MLL1-Menin complex induces targeting of the enzymatic subunits of the MLL3/4-UTX complex to non-canonical sites that are normally bound by the MLL1-Menin complex and are distinct from those bound by the MLL-FP (**Extended Fig. 12A-C**). These results provide additional evidence for the existence of a molecular switch between the MLL complexes that is induced by Menin-MLL inhibition.

The above results are provocative, as promoter-associated H3K4me1 facilitates transcriptional repression in other cellular settings[60], suggesting that deposition of H3K4me1 at gene promoters could depend on context[61]. Nevertheless, our finding that *Utx*^{KO}, *Mll3*^{KO}, and *Mll4*^{KO} cells are resistant to Menin-MLL inhibition (**Fig.1**, **Extended Fig. 3E-G**) – combined with the colocalization of UTX, MLL3, MLL4, and H3K4me1 at the promoters of target genes – led us to hypothesize that

the MLL3/4-UTX complex co-regulates gene expression in the context of leukemia. To test this hypothesis, we leveraged H3 lysine-4-to-methionine (K4M) 'oncohistone' mutants as orthogonal molecular tools to destabilize the MLL3/4-UTX complex[62] (**Extended Fig. 13A**). Supporting our model, expression of H3.1K4M in MLL-AF9 leukemia cells led to a substantial proliferative advantage only in the context of Menin-MLL inhibition (**Extended Fig. 13B-E**), demonstrating that destabilization of the MLL3/4-UTX complex (**Extended Fig. 13F**) can phenocopy the intrinsic resistance of *Utx*-, *Mll3*-, and *Mll4*-deficient cells to Menin-MLL1 inhibition (**Fig.1E-F, Extended Fig. 3E-G**). These results further support a model whereby the MLL3/4-UTX complex serves as a central modulator of therapy response to Menin-MLL inhibition.

Reciprocal transcriptional regulation of tumor suppressive pathways by Menin and UTX

The above results support a model whereby a molecular switch between Menin and UTX at gene promoters dictates responses to Menin-MLL inhibition. We hypothesized that this switch acts through transcriptional regulation of genes involved in pathways that control cellular proliferation and survival. To test this, we performed transcriptional profiling of MLL-AF9 leukemia cells in the absence and presence of MI-503 and identified pathways that are reciprocally regulated by Menin and UTX (**Extended Fig. 14A-C**). Although the catalytic activity of the MLL1/2-Menin histone methyltransferase complex is canonically associated with actively transcribed developmental genes[2, 13], disruption of the complex by MI-503 resulted in both up- and down-regulation of gene expression, with slight skewing towards gene activation (**Fig.4A**). Remarkably, the majority of significantly upregulated genes were reciprocally bound by Menin and UTX, suggesting that their expression is tightly co-regulated by these chromatin factors and gene repression mechanisms might be operative in this context (**Fig.4B**). Consistent with this observation, ChIP-Seq against H4K16ac (associated with gene activation) showed that the levels of this mark increased in the context of Menin-MLL inhibition (**Extended Fig. 15A-B**). These results support a model whereby Menin-MLL inhibition leads to dynamic changes in gene expression due to loss of MLL-dependent

repressive activity and a concomitant increase in histone acetylation marks associated with gene activation (e.g., H4K16ac)[63, 64].

To determine if UTX was necessary for the activation of these genes, we generated *Utx*-deficient (*Utx*^{KO}) MLL-AF9 leukemia cells (**Extended Fig. 14D**), treated these with MI-503, and profiled by RNA-Seq (**Extended Fig. 14E**). UTX bound genes induced by MI-503 failed to get activated in *Utx*^{KO} cells, suggesting that UTX function is necessary for their transcriptional activation when Menin is displaced from chromatin (we refer to these genes as 'Menin-UTX targets') (**Fig.4C**, **Supplementary Table 4**). We also confirmed that transcriptional targets of the MLL-AF9 fusion were downregulated in the MI-503 context (**Extended Fig. 16A-B**), as reported by others[23, 26, 27]. As shown earlier, *Utx*^{KO} leukemia cells treated with MI-503 are able to proliferate without re-expression of *Meis1*, a critical Menin-MLL-FP target[26, 27, 52, 53] (**Fig.1E**, **Extended Fig. 6B, Extended Fig. 16C-D**). These data suggest a new paradigm whereby the effects of Menin-MLL inhibition on MLL-FP target genes are independent of its effects on Menin-UTX transcriptional targets, and that induction of a tumor suppressive gene expression program alongside repression of canonical MLL-FP targets is required for the anti-leukemic activity of Menin-MLL1 inhibitors.

To gain insight into pathways directly regulated by Menin and UTX, we performed gene ontology (GO) analysis[65, 66] of Menin-UTX targets (**Supplementary Table 4**) and found significant evidence for their association with transcriptional programs related to proliferation, differentiation, and survival (**Extended Fig. 14C**). To further evaluate the relevance of these GO terms, we performed Gene Set Enrichment Analysis (GSEA)[67] on RNA-Seq data from *Utx*^{WT} and *Utx*^{KO} cells ± MI-503 and observed a highly significant correlation between the presence of UTX and the expression of senescence-associated genes following MI-503 treatment[68] (**Fig.4D**, **Extended Fig. 17A-F**, **Supplementary Table 4**). This correlation was independently confirmed using a curated list of genes involved in cell cycle arrest and therapy-induced senescence[69] (**Fig.4E**) and is consistent with the fact that Menin-MLL inhibition induces a combination of cell cycle arrest, apoptosis, and

differentiation[23], as well as our observation that the senescence-associated H4K16ac mark increases with MI-503 treatment[70] (**Extended Fig. 1E-F, Extended Fig. 15**). The cellular senescence program is highly complex and is characterized in part by induction of permanent cell cycle arrest and a senescence-associated secretory phenotype (SASP)[71]. Consistent with a direct role for the Menin-UTX switch in regulating cellular senescence, secretion of prototypical SASP cytokines like IL-6, IFNβ-1, IL-3, and IL-15 was induced upon Menin-MLL inhibition in a *Utx*-dependent manner (**Fig.4F-G, Extended Fig. 18**). These results demonstrate that Menin-MLL inhibition engages a potent tumor suppressive network that is transcriptionally regulated in large part by the MLL3/4-UTX complex.

Combinatorial targeting of Menin and CDK4/6 to overcome resistance associated with loss of MLL3/4-UTX function

Given that cellular senescence can be regulated at both transcriptional and post-transcriptional levels, and chromatin regulation has been functionally implicated in modulating this program[70, 72, 73], we hypothesized that the Menin-UTX molecular switch directly regulates the expression of cell cycle arrest- and senescence-associated genes by direct binding to their promoters[56, 74]. Consistent with our hypothesis, we found that Menin is bound to the promoters of the cyclin-dependent kinase (CDK) inhibitors *Cdkn2c/Ink4c* and *Cdkn2d/Ink4d* at basal conditions[75], and that binding is abrogated upon Menin-MLL inhibition, leading to induction of their expression (**Fig.4H**, **Extended Fig. 19A-B, Extended Fig. 20**). Conversely, we found that UTX binds to these promoters only in the context of Menin-MLL inhibition, leading to UTX-dependent upregulation of both CDK inhibitors (**Fig.4H**, **Extended Fig. 19A-B**). These data show that the Menin-UTX molecular switch regulates the expression of these CDK inhibitors by direct chromatin regulation.

Since the proteins encoded by these two genes are natural inhibitors of the CDK4 and 6 kinases[75], we hypothesized that pharmacological inhibition of CDK4/6 would bypass the intrinsic resistance

of *Utx*^{KO} cells to MI-503 while retaining the therapeutic effects of Menin-MLL inhibition on MLL-FP targets (**Fig.4I**). We therefore combined MI-503 with the FDA-approved CDK4/6 inhibitor Palbociclib[76], which has been shown to trigger durable cell cycle arrest and senescence[69, 77, 78]. *Utx*^{KO} cells were more resistant to either MI-503 or Palbociclib alone when compared to *Utx*^{WT} cells, likely due to higher basal levels of both *Cdk4* and *Cdk6* transcripts (**Fig.4J, Extended Fig. 19C-D**) (refs. 74, 79). However, combined inhibition of Menin-MLL and CDK4/6 resulted in a synergistic effect (CD=0.4) (ref. 80) on inhibiting cell proliferation to similar levels achieved by MI-503 treatment of *Utx*^{WT} cells (**Fig.4J**). These proof-of-concept data demonstrate that targeting pathways regulated by Menin and UTX can produce combinatorial therapeutic effects and further suggest that the anti-leukemic effects of MI-503 (ref. 23) are primarily through reactivation of tumor suppressor pathways and not solely through dampening transcription of MLL-FP targets like *Meis1* (refs. 23, 26, 27, 53). Thus, combination of Palbociclib with Menin-MLL inhibitors may represent a novel and more effective therapeutic strategy for Menin-dependent cancers[22, 24, 25, 81, 82].

Response to Menin-MLL inhibitors in primary human AML is accompanied by transcriptional induction of MLL3/4-UTX-dependent tumor suppressive programs

Small molecule inhibitors of the Menin-MLL interaction have shown promise in preclinical models of acute lymphoid and myeloid leukemias[26, 27, 83] and are currently in Phase I/II clinical trials for treatment of patients with acute leukemia (SNDX-5613 (NCT04067336), KO-539 (NCT04065399), and JNJ-75276617 (NCT04811560)). Notably, SNDX-5613 was recently granted fast track designation by the FDA for treatment of relapsed/refractory acute leukemias. We hypothesized that the Menin-UTX molecular switch described above would be operative in leukemia patients treated with these Menin-MLL inhibitors. Consistent with our hypothesis, longitudinal RNA-Seq analysis of AML cells derived from two patients with *NPM1c*-mutated (Patient 1) and *MLL*-rearranged (Patient 2) leukemia treated with SNDX-5613 as part of the

AUGMENT-101 clinical trial (NCT04065399) showed concomitant suppression of canonical MLL-FP target genes (e.g., *MEIS1*) and induction of CDK inhibitors (e.g., *CDKN2C*) (**Fig.5A-E, Extended Fig. 21**).

As an orthogonal approach, we analyzed a panel of genetically-annotated patient-derived xenografts (PDXs) of *MLL*-rearranged acute leukemia for response and resistance to VTP-50469 (a close analog of SNDX-5613) *in vivo*[26] (**Fig.5F, Extended Fig. 22A**). Mice transplanted with an *MLL3* wild type PDX showed a potent response to VTP-50469 and significant induction of Menin-UTX targets (**Fig.5G-H, Extended Fig. 23A-B**), reflecting the activation of the tumor suppressive gene expression program defined in this study (**Fig.4**). Conversely, an *MLL3* mutant PDX exhibited primary resistance to VTP-50469 and failed to induce this gene expression program (**Fig.5I-J, Extended Fig. 23A and S23C**), thereby linking the induction of Menin-UTX-targets to preclinical drug response. DNA sequencing confirmed that the resistant PDX harbored a missense mutation in the *MLL3* gene (**Extended Fig. 22B**). Thus, the gene expression programs regulated by the epistatic relationship between the MLL1/2-Menin and MLL3/4-UTX complexes are at play in patients and patient-derived xenografts treated with orally bioavailable Menin-MLL inhibitors that are currently under clinical investigation. Somatic mutations in members of the MLL3/4-UTX complex that impact catalytic activity or protein complex composition may impact the induction of tumor suppressive gene expression programs induced by Menin-MLL-inhibitors, thereby blunting clinical responses.

DISCUSSION

The Menin chromatin adaptor protein exhibits profound context-specific functions in different tissues, acting as a tumor suppressor gene in neuroendocrine[14, 15], lung[17, 84], skin[16], and CNS malignancies[18] and as an oncogenic cofactor in hepatocellular[19] and hematologic cancers[4, 20]. Given that Menin can interact with similar cofactors in disparate settings, the basis for these

apparently paradoxical findings has remained largely unclear. For example, Menin functionally cooperates with MLL proteins to activate transcription of the *Cdkn1b/p27^{Kip1}* and *Cdkn2d/Ink4d* CDK inhibitors as a tumor suppressive mechanism in neuroendocrine tumors and lung cancer[3, 17, 85, 86], yet the same protein-protein interaction is critical for leukemia maintenance[4, 10, 20]. These contrasting observations suggest that Menin employs unique molecular mechanisms to regulate chromatin and gene expression depending on the context.

Our study sheds light on these paradoxical observations by providing the first evidence for a functional interaction between the mammalian histone methyltransferase complexes MLL1/2-Menin and MLL3/4-UTX and challenges the paradigm that these complexes are restricted to certain genomic compartments (**Fig.6**). We show that the Menin-MLL and NF-Y complexes coordinately inhibit the expression of a tumor suppressive network that involves the *Cdkn2c/Ink4c* and *Cdkn2d/Ink4d* tumor suppressor genes in leukemia by direct binding to gene promoters. Disruption of Menin-MLL or NF-Y complexes using genetic or pharmacological approaches triggers a molecular switch that leads to recruitment of the MLL3/4-UTX complex to the promoters of tumor suppressive genes, including the *Cdkn2c/Ink4c and Cdkn2d/Ink4d* CDK inhibitors[75]. This molecular switch leads to UTX-dependent activation of gene expression and is associated with a concomitant increase in the levels of the H4K16ac histone mark, resulting in robust induction of tumor suppressive programs like cellular senescence[70, 73]. Thus, the molecular choreography between the MLL1/2-Menin and MLL3/4-UTX complexes dictates cellular survival in leukemia.

Based on our observation that UTX directly binds to and activates the expression of *Cdkn2c/Ink4c and Cdkn2d/Ink4d* (which are natural inhibitors of the CDK4/6 kinases)[75], we combined Menin-MLL inhibition with the FDA-approved CDK4/6 kinase inhibitor Palbociclib[76] and showed that this combinatorial approach leads to a strong synergistic effect on inhibiting leukemia cell proliferation. As Palbociclib and other CDK4/6 inhibitors are already FDA-approved[77], our proof-of-concept studies suggest that this combinatorial approach could be a viable therapeutic option to both boost

the effectiveness of Menin inhibitors as monotherapies while potentially overcoming the intrinsic resistance to Menin-MLL inhibition conferred by loss-of-function of the MLL3/4-UTX complex.

Our study demonstrates — in murine and human systems — that the functional interplay between MLL1/2-Menin and MLL3/4-UTX is critical for Menin-inhibitor responses due to induction of Menin-UTX target genes. Notably, we were able to show that the induction of this gene expression program is at play upon oral delivery of VTP-50469 to leukemia PDX models and SDNX5613 to human AML subjects in the context of the AUGMENT-101 clinical trial (NCT04065399). Importantly, the Menin-UTX signature was absent in a non-responsive PDX harboring a missense mutation in *MLL3*, providing the first evidence supporting the concept that somatic variants in genes encoding for members of the MLL3/4 complex may blunt Menin-MLL inhibitor responses in the clinic.

FIGURE LEGENDS

Fig. 1. CRISPR screens uncover functional interplay between the mammalian MLL1/2 and MLL3/4 chromatin modifying complexes. (A) CRISPR-Cas9-based screening strategy to identify chromatin regulators that modulate response to Menin inhibition. CPD, cell population doublings; sgRNA, single guide RNA; TF, final timepoint; T0, initial timepoint. **(B)** Top 20 most significantly enriching (red) and depleting (blue) genes in the MI-503-treated CRISPR screen. The histone demethylase *Utx* and the histone methyltransferases *Mll3* and *Mll4* emerged as top hits in the MI-503-treated screen (red circles). Gene scores are shown as the mean $\log_2$ fold-change in abundance of the 6 sgRNAs targeting each gene in each condition. **(C)** Genome-wide screening data showing gene-level ranking based on differential enrichment of sgRNAs under Menin-MLL inhibitor treatment (VTP-50469) relative to vehicle (DMSO). Differential (Δ) beta-score between VTP-50469 and DMSO conditions was calculated using MaGeCK. A positive Δ beta-score denotes enrichment of specific gene-targeting sgRNAs. A negative Δ beta-score denotes

depletion of specific gene-targeting sgRNAs. Red circles denote MLL3/4-UTX complex subunits. Yellow circles denote PRC1.1 complex subunits. **(D)** Schematic representation of the top scoring chromatin regulators in chromatin-focused MI-503 screen and their corresponding protein complexes. Red denotes enriching subunits. Blue denotes depleting subunits. Color scale represents the $\log_2$ fold-change in MI-503. **(E)** Cell viability assay from cells treated with DMSO (vehicle, black) or MI-503 (red) after 96 hours (mean±SEM, n=3 infection replicates, *P*-value calculated by Student's t-test). sgCtrl, control sgRNA targeting a non-genic region on chromosome 8. **(F)** Differential fitness is shown as the relative fitness of double positive cells (sgMen1-RFP + sgUtx-BFP or sgMen1-RFP + sgCtrl-BFP) to single positive cells (sgMen1-RFP) 16 days post-infection measured by flow cytometry (mean±SEM, n=3 infection replicates, *P*-value calculated by Student's t-test).

Fig. 2. Menin restricts chromatin occupancy of UTX at promoter regions. (A) Average chromatin occupancy of Menin at transcription start sites (TSS), and 2kb upstream and downstream of the TSS are also included. Signals corresponding to cells treated with MI-503 (solid) compared to cells treated with DMSO (dotted) after 96 hours are shown. RPM, reads per million. **(B)** Average chromatin occupancy of UTX at transcription start sites (TSS), and 2kb upstream and downstream of the TSS are also included. Signals corresponding to cells treated with MI-503 (solid) after 96 hours compared to cells treated with DMSO (dotted) after 96 hours are shown. RPM, reads per million. **(C)** Relative *Utx* mRNA levels determined by qPCR in MLL-AF9 cells treated with MI-503 (red) versus DMSO (black) after 96 hours (mean ± SEM, n=3 replicates, *P*-value calculated by Student's t-test). **(D)** Western blot analysis of Menin, UTX, and HSP90 proteins (loading control) upon MI-503 treatment of MLL-AF9 cells after 96 hours. **(E)** Heatmaps displaying Menin (black) and UTX (purple) ChIP-Seq signals mapping to a 4kb window around TSSs. Data is shown for DMSO and MI-503-treated cells after 96 hours. Metaplot represents the average ChIP-Seq signal for Menin or UTX at promoters that are UTX+ (green) or

UTX- (black). **(F)** Genome browser representation of ChIP-Seq normalized reads for Menin (black) and UTX (purple) in MLL-AF9 leukemia cells treated with either vehicle or MI-503 after 96 hours. **(G)** ChIP-Seq normalized reads per 10-kb bin for Menin (MI-503 vs DMSO, y-axis) and UTX (MI-503 vs DMSO, x-axis). Pearson's correlation coefficient is indicated.

Fig. 3. Promoter regulation by the MLL3/4 complex dictates outcome of Menin inhibition. (A) Schematic representation of the mammalian MLL1/2 histone methyltransferase complex. Highlighted in red are the enzymatic subunits of the complex. Yellow denotes shared subunits with the MLL3/4 complex. **(B)** Schematic representation of the mammalian MLL3/4 histone methyltransferase complex. Highlighted in pink and purple are the enzymatic subunits of the complex. Yellow denotes shared subunits with the MLL1/2 complex. Green denotes non-enzymatic subunits of the MLL3/4 complex. **(C)** Heatmaps displaying MLL1 (red) and H3K4me3 (blue) ChIP-Seq signals mapping to a 4-kb window around TSSs. Data is shown for DMSO and MI-503-treated cells for 96 hours. Metaplot represents the average ChIP-Seq signal for each protein at promoters that are UTX+ (green) or UTX- (black). **(D)** Heatmaps displaying MLL3/4 (pink) and H3K4me1 (grey) ChIP-Seq signals mapping to a 4-kb window around TSSs. Data is shown for DMSO and MI-503-treated cells for 96 hours. Metaplot represents the average ChIP-Seq signal for each protein at promoters that are UTX+ (green) or UTX- (black).

Fig. 4. Reciprocal transcriptional regulation of tumor suppressive pathways by Menin and UTX. (A) Volcano plot of differentially expressed genes in mouse MLL-AF9 cells treated with Menin inhibitor (MI-503) or vehicle (DMSO) after 96 hours. Significantly ($P<0.05$) downregulated (DN) genes are shown on the left (n=921 genes). Significantly ($P<0.05$) upregulated (UP) genes are shown on the right (n=1030). **(B)** Upset plot showing significant overlap (red) between genes that undergo replacement of Menin by UTX at their respective promoters and MI-503-induced genes. *P*-value for overlap is shown. **(C)** Boxplot showing expression levels of genes that are induced by MI-503 treatment and are bound by UTX at their promoters in this condition and by

Menin at steady-state. Expression levels are shown for *Utx*^{WT} and *Utx*^{KO} leukemia cells. **(D)** Gene set enrichment analysis (GSEA) showing that Menin-UTX target genes induced by MI-503 are significantly enriched for genes and pathways regulating cellular senescence. FDR, false discovery rate; NES, normalized enrichment score. **(E)** Heat map denoting relative gene expression levels of senescence-associated cell cycle and SASP genes measured by RNA-Seq from *Utx*^{WT} and *Utx*^{KO} MLL-AF9 leukemia cells treated with Menin inhibitor (MI-503) or vehicle (DMSO) after 96 hours. Senescence-associated cell cycle and SASP gene list was manually curated from[69]. **(F)** Secreted levels of IL-6 and (G) IFNβ-1 in *Utx*^{WT} (black) and *Utx*^{KO} (red) MLL-AF9 leukemia cells treated with Menin inhibitor (MI-503) or vehicle (DMSO) after four or six days. Data are quantified as pg/mL of secreted cytokine per million cells and represent the mean of three biological replicates. *P*-value calculated by Student's t-test. **(H)** Genome browser representation of ChIP-Seq (top) and RNA-Seq (bottom) normalized reads (average RPKM) for *Cdkn2c* and *Cdkn2d* loci from *Utx*^{WT} or *Utx*^{KO} MLL-AF9 leukemia cells treated with DMSO or MI-503 for 96 hours. **(I)** Proposed model and rationale for combination therapies based on Menin-MLL and CDK4/6 inhibitors. Our data support a model whereby **(1)** Menin restricts UTX-mediated transcriptional activation of tumor suppressor genes, including *Cdkn2c* and *Cdkn2d*, which are natural inhibitors of the CDK4 and CDK6 kinases, which in turn inhibit cell cycle arrest and senescence. Our model predicts that CDK4/6 inhibition using Palbociclib should boost the anti-cancer activity of Menin-MLL inhibitors, which we show induces a MLL3/4-UTX tumor suppressive axis, by more potently inhibiting these downstream kinases. On the other hand, Menin is known to be required for activation of MLL-FP targets like *Meis1* and *Cdk6* itself to sustain leukemia **(2)**. Thus, our model predicts that combination therapies based on Menin-MLL and CDK4/6 inhibitors should act synergistically to suppress leukemia proliferation by potently engaging two parallel pathways that converge on regulation of cell cycle progression. **(J)** Relative viability of *Utx*^{WT} and *Utx*^{KO} MLL-AF9 leukemia cells treated with either DMSO, MI-503, Palbociclib, or a combination of both inhibitors for 6 days (mean±SEM, n=3 replicates, *P*-value calculated by Student's t-test).

Fig. 5. Reciprocal transcriptional regulation of tumor suppressive pathways by Menin and UTX. (A) Longitudinal flow cytometry analysis measuring the fraction of CD45low, cKIT+ leukemia cells in the peripheral blood of a *NPM1c* mutant patient (Patient 1) during treatment cycle 1 of SDNX-5613 as part of the AUGMENT-101 clinical trial (NCT04065399). **(B)** Heatmap denoting temporal gene expression changes among MLL-FP targets in FACS-sorted AML blasts cells from Patient 1. Plotted are all MLL-FP targets that are differentially expressed at day 14 vs. day 0 of treatment cycle 1. **(C)** Temporal expression levels of genes involved in cell cycle arrest and senescence (*CDKN1A*, *CDKN2B*, and *CDKN2C*) and MLL-FP targets (*HOXA9*, *CDK6*, *PBX3*, and *MEIS1*) in AML cells from Patient 1 treated with SDNX-5613. **(D)** Heatmap denoting temporal gene expression level changes among MLL-FP targets in FACS-sorted AML blasts cells from Patient 2 treated with SDNX-5613 as part of the AUGMENT-101 clinical trial (NCT04065399). Plotted are all MLL-FP targets that are differentially expressed at day 10 vs. day 0 of treatment cycle 1. **(E)** Temporal expression levels of genes involved in cell cycle arrest and senescence (*CDKN1A*, *CDKN1B*, and *CDKN3*) and MLL-FP targets (*HOXA7*, *CDK6*, *MEF2C*, and *MEIS1*) in AML cells from Patient 2 treated with SDNX-5613. **(F)** Schematic of *in vivo* treatment experiments using genetically-defined patient-derived xenografts (PDXs). NSG mice were transplanted with either *MLL3*-WT or *MLL3*-Mutant AML PDXs and, upon disease engraftment, were randomized into VTP-50469 (0.03% in rodent diet) or normal chow for a duration of four weeks. Disease progression was monitored weekly by bleeding and AML cells were sorted at 7 days post initiation of treatment using magnetic mouse cell depletion from the bone marrow of animals to perform RNA-Seq. **(G)** Disease progression as measured by the percentage of human CD45+ cells in the peripheral blood of mice harboring *MLL3*-WT leukemia treated with vehicle (blue) or VTP-50469 (red). **(H)** Boxplot denoting gene expression levels of Menin-UTX targets in AML cells isolated from mice harboring *MLL3*-WT leukemia treated with vehicle (grey) or VTP-50469 (blue). **(I)** Disease progression as measured by the percentage of human CD45+ cells in the peripheral blood of mice harboring *MLL3*-Mutant leukemia treated with vehicle (blue) or VTP-50469 (red).

(J) Boxplot denoting gene expression levels of Menin-UTX targets in AML cells isolated from mice harboring *MLL3*-Mutant leukemia treated with vehicle (grey) or VTP-50469 (blue).

Fig. 6. A molecular switch between mammalian MLL complexes dictates response to Menin-MLL inhibition.

ACKNOWLEDGEMENTS

We thank all members of the Allis, Lowe, and Armstrong laboratories for their help and support; Richard Phillips, Robert G. Roeder, Tom W. Muir, Benjamin A. Garcia, Ross Levine, Sheng Cai, and Charles J. Sherr for scientific discussions; David Chen (Chun-Wei Chen) for mouse MLL-AF9 cells, Zhaohui Feng for human leukemia cells, and Laura Whitman (Agilent) for OLS support. C.D.A. was supported by US National Institutes of Health (NIH) grants (P01CA196539 and 5R01CA204639-03), the Leukemia and Lymphoma Society (LLS-SCOR 7006-13), and the Rockefeller University and St. Jude Children's Research Hospital Collaborative on Chromatin Regulation in Pediatric Cancer. S.W.L was supported by a NIH/NCI grant (R01 CA190261) and an Agilent Thought Leader Award, as well as the MSKCC cancer center support grant (P30 CA008748). S.W.L. is the Geoffrey Beene Chair of Cancer Biology and a Howard Hughes Medical Institute Investigator. S.A.A was supported by NIH grants CA176745, CA206963, CA204639 and CA066996. Y.M.S.F was supported by the Damon Runyon-Sohn Pediatric Cancer Fellowship (DRSG-21-17) and NIGMS-MOSAIC K99/R00 Career Development Award (1K99GM140265-01). F.J.S.R. was partially supported by the MSKCC TROT program (5T32CA160001), a MSKCC GMTEC Postdoctoral Researcher Innovation Grant, and is a HHMI Hanna Gray Fellow. F.P. was supported by the German Research Foundation (DFG, PE 3217/1-1) and a Momentum Fellowship award by the Mark Foundation for Cancer Research. D.W.B. was supported by a Ruth L. Kirschstein National Research Service Award (5F32CA217068). E.R.K. was supported by an F31 NRSA predoctoral fellowship from the NIH/NCI (F31CA192835).

AUTHOR CONTRIBUTIONS

Y.M.S.F., F.J.S.R., F.P, S.A.A, S.W.L., and C.D.A. conceived the study and wrote the manuscript with input from all the authors; Y.M.S.F., F.J.S.R., F.P., Y.X., L.G., M.C.B., and D.C. conducted experiments; D.W.B., T.C., and Y.J.H. analyzed RNA-Seq and ChIP-Seq data; Y.J.H. and E.R.K. analyzed CRISPR-screen data. S.G. and X.S.L. provided genome-wide CRISPR library. A.V.K., M.M., and E.dS. provided patient-derived xenograft samples. R.M.S. provided primary AML samples from patients in the Syndax trial A.S. provided conceptual advice. S.A.A, S.W.L., and C.D.A. supervised the study and secured funding.

DECLARATION OF INTERESTS

C.D.A. is a co-founder of Chroma Therapeutics and Constellation Pharmaceuticals and a Scientific Advisory Board member of EpiCypher. S.W.L. is an advisor for and has equity in the following biotechnology companies: ORIC Pharmaceuticals, Faeth Therapeutics, Blueprint Medicines, Geras Bio, Mirimus Inc., and PMV Pharmaceuticals. S.W.L. also acknowledges receiving funding and research support from Agilent Technologies for the purposes of massively parallel oligo synthesis. S.A.A. has been a consultant and/or shareholder for Vitae/Allergan Pharmaceuticals, Epizyme Inc., Imago Biosciences, Cyteir Therapeutics, C4 Therapeutics, Syros Pharmaceuticals, OxStem Oncology, Accent Therapeutics, and Mana Therapeutics. S.A.A. has received research support from Janssen, Novartis, and AstraZeneca. The remaining authors declare no competing interests.

MATERIALS AND METHODS

<u>Plasmids and sgRNA cloning</u>

To generate stable Cas9-expressing cell lines, we used lentiCas9-Blast (Addgene, 52962). Human wild-type or mutant (K4M) histone H3.1 were cloned into pCDH-EF1-MCS-IRES-RFP (System Biosciences, CD531A-2). To express sgRNAs, we generated the pUSEPR (U6-sgRNA-EFS-Puro-P2A-TurboRFP) and pUSEPB (U6-sgRNA-EFS-Puro-P2A-TagBFP) lentiviral vectors by Gibson assembly of the following DNA fragments: (i) PCR-amplified U6-sgRNA (improved scaffold)[87] cassette, (ii) PCR-amplified EF1s promoter, (iii) PCR-amplified Puro-P2A-TurboRFP or -TagBFP gene fragment (IDT), and (iv) BsrGI/PmeI-digested pLL3-based lentiviral backbone[88]. For sgRNA cloning, pUSEPR and pUSEPB vectors were linearized with BsmBI (NEB) and ligated with BsmBI-compatible annealed and phosphorylated oligos encoding sgRNAs using high concentration T4 DNA ligase (NEB). All sgRNA sequences used are listed in Supplementary Table 1.

Cell culture

Mouse MLL-AF9 leukemia cells were kindly shared by David Chen (Chun-Wei Chen) and were originally generated by transformation of female mouse bone marrow Lin-Sca1+cKit+ (LSK) cells with an MSCV-IRES-GFP (pMIG) retrovirus expressing the human MLL-AF9 fusion protein and transplanted into sub-lethally irradiated recipient mice as described previously[29, 89]. Leukemic blasts were harvested from moribund mice and cultured in vitro in IMDM (Gibco) supplemented with 15% FBS (Gibco), mouse IL-6 (10ng/μL, PeproTech), mouse IL-3 (10ng/μL, PeproTech), mouse SCF (20ng/μL, PeproTech), penicillin (100U/mL, Gibco), streptomycin (100μg/uL, Gibco), L-glutamine (2mM, Gibco), and plasmocin (5μg/mL, InvivoGen). Human leukemia cell lines MV4;11 and OCI-AML3 were kindly shared by Zhaohui Feng and were cultured in RPMI 1640 (Corning) supplemented with 10% FBS (Gibco), penicillin (100U/mL, Gibco), streptomycin (100μg/uL, Gibco), L-glutamine (2mM, Gibco), and plasmocin (5μg/mL, InvivoGen). Mouse NIH-3T3 cells were maintained in DMEM (Corning) supplemented with 10% FCS (ATCC), penicillin (100U/mL, Gibco), streptomycin (100μg/uL, Gibco), and plasmocin (5μg/mL, InvivoGen). Human

HEK293 cells were maintained in DMEM (Corning) supplemented with 10% FBS (Gibco), penicillin (100U/mL, Gibco), streptomycin (100µg/uL, Gibco), and plasmocin (5µg/mL, InvivoGen). Cas9-expressing cells were generated by lentiviral transduction of lentiCas9-Blast followed by Blasticidin (InvivoGen) selection and validation of Cas9 expression and activity. All cells were confirmed to be free of Mycoplasma contamination and cultured at 37°C and 5% CO2.

Virus production

Lentiviruses were produced by co-transfection of HEK293T (ATCC) cells with pUSEPR-EpiV2.0 sgRNA library, individual sgRNA plasmids, or lentiCas9-Blast, and packaging vectors psPax2 (Addgene, 12260) and pMD2.G (Addgene, 12259) using Lipofectamine 2000 (Invitrogen). Viral supernatants were collected at 48 and 72 hours post transfection and stored at -80°C.

Transduction of cell lines

Leukemia cells were seeded at a density of 2.5 x 10^5 cells/well of a non TC-treated 12-well plate in complete medium containing polybrene (10µg/mL, EMD Millipore), and then transduced with lentivirus by centrifugation at 2,500rpm for 90 minutes at 37°C. After a 24-hour incubation, cells were transferred to a new plate containing fresh culture medium. Antibiotic selection or cell sorting was done 48 hours post transduction.

Drug treatments

For MI-503 (Active Biochem) treatments, leukemia cells were seeded at a density of 4 x 10^5 cells/mL, treated with limiting dilutions of the inhibitor as indicated or 0.25% DMSO (vehicle). Cells were re-plated every 4 days to the initial density and re-treated. Viability was assessed at various time points by using the CellTiter-Glo Luminescent Cell Viability assay (Promega) following the manufacturer's guidelines. Ratio of luminescence signal from metabolically active cells in MI-503 versus DMSO were plotted to calculate IC50 values (Prism 8, GraphPad). For MI-503 (Active

Biochem) and Palbociclib HCl (Selleckchem) combination treatments, 25,000 leukemia cells in 250µL of drug-containing medium were seeded in a 48-well plate and viability was assessed every 4 days by using the CellTiter-Glo Luminescent Cell Viability assay (Promega). For RNA-Seq and ChIP-Seq experiments, cells were cultured at 4 x 10^5 cells/mL, treated with MI-503 (concentrations as indicated in Fig.legends) or 0.25% DMSO for 4 days. Cells were collected, washed with PBS, pelleted, and flash-frozen before RNA or chromatin isolation. For VTP-50649, XYZ, chow

Flow cytometric analyses

Immunophenotyping of leukemia cells treated with MI-503 (or vehicle), was done by collecting cells post treatment and staining using the indicated conjugated primary antibodies. Stained samples were analyzed on an LSRFortessa (BD Biosciences) flow cytometer. Data analysis was performed using FlowJo (BD Biosciences) software. Intracellular antigens detection was done by using the Foxp3/Transcription Factor Staining Buffer Set (eBioscience) following the manufacturer's guidelines. Conjugated primary antibodies used were: Pacific Blue anti-CD11b (Biolegend, 101224), Alexa Fluor 647 anti-Cas9 (CST, 48796).

Xenograft models of AML

All animal experiments were performed with the approval of Dana-Farber Cancer Institute's Institutional Animal Care and Use Committee (IACUC). NOD.Cg-*Prkdcscid Il2rgtm1Sug*/JicTac (NOG) mice were obtained from Taconic Biosciences (Rensselaer, NY, USA). Non-irradiated 8-12-week-old adult mice were transplanted with previously established patient derived xenografts (PDXs)[26, 90] via tail vein injection (250,000 cells/mouse). Engraftment of human cells ($hCD45^+$) was analyzed and monitored longitudinally by weekly bleeding to quantify $hCD45^+$ cells in the peripheral blood by flow cytometry with human CD45-PE and anti-mouse CD45-APC-Cy7 antibodies (Biolegend, San Diego, CA, USA). Mice were monitored closely to detect disease

onset and treatment started when hCD45$^+$ cells were detectable in the peripheral blood. Mice were randomly assigned to either normal or 0.1% VTP-50469 rodent special diet[26]. Mice were bled weekly to monitor leukemia burden as described above and euthanized when showing clinical signs of disease (experimental endpoint). Leukemia cells from a subset of these animals were harvested after seven days of treatment to perform RNA-seq (see methods section on RNA-seq).

Longitudinal analysis of AML patient treated with SNDX-5613

Peripheral blood of patients was taken under informed consent according to the Declaration of Helsinki during routine blood draws at screening and different timepoints during the first cycle of treatment with SDNX-5613 within the AUGMENT-101 clinical trial (NCT04065399). Peripheral blood mononuclear cells (PBMCs) were subsequently isolated using Ficoll (BD Bioscience, Franklin Lakes, NJ, USA) gradient centrifugation, viably frozen, and banked at the Dana-Farber Cancer Institute, Boston, MA (approved institutional protocol, IRB: #01-206). For longitudinal analysis, samples were thawed, washed twice in PBS, and stained with anti-CD45 (PE) and anti-CD117 (APC) (Biolegend, San Diego, CA, USA). CD45-low/CD117+ leukemia cells were FACS sorted (MA900 sorter, Sony Biotechnology, San Jose, CA, USA) and subsequently processed for RNA-seq (see methods section on RNA-seq).

Immunoblotting

Whole cell lysates were separated by SDS-PAGE, transferred to a PVDF membrane (EMD Millipore), blocked in 5% non-fat milk in TBS plus 0.5% Tween-20 (Sigma-Aldrich), probed with primary antibodies, and detected with HRP-conjugated anti-rabbit or anti-mouse secondary antibodies (GE Healthcare). Primary antibodies used included: anti-Cas9 (CST, 14697), anti-UTX (CST, 33510), anti-Menin (Bethyl, A300-105A), anti-NF-YA (Santa Cruz Biotechnology, sc-

17753), anti-Actin (abcam, ab8224), anti-HSP90 (BD Biosciences, 610418), anti-HA (Biolegend, 901501), anti-H3K4me1 (abcam, ab8895), anti-H3K4me3 (CST, 9751), anti-H3 (abcam, ab1791).

Locus-specific DNA sequencing

To determine the mutational status of the Men1 and Utx loci in cells targeted by CRISPR-Cas9, we performed next generation sequencing of PCR-amplified target regions. Genomic DNA (gDNA) was isolated using the DNeasy Blood & Tissue Kit (Qiagen) following the manufacturer's guidelines. Amplification of target regions was performed from 500ng of gDNA using Q5 High-Fidelity 2X Master Mix (NEB) and primers listed in Supplementary Table 1. PCR products were purified using the QIAquick PCR Purification Kit (Qiagen) and sequenced on Illumina instruments at GENEWIZ (Amplicon-EZ service).

RNA isolation, qRT-PCR analyses, and RNA sequencing

Total RNA was isolated from cells using the RNeasy kit (Qiagen, Hilden, Germany). RNA was reverse transcribed with High-Capacity cDNA Reverse Transcription kits (Applied Biosystems) following the manufacturer’s instructions. Quantitative PCRs (qRT-PCRs) were performed using the TaqMan Gene Expression Master Mix (Applied Biosystems) with the StepOne Real-Time System (Applied Biosystems). TaqMan gene expression assays were used. ActB was used as the endogenous control for normalization and relative gene expression was calculated by using the comparative CT method. The mouse gene probes used were: *ActB* (Mm02619580_g1), *Hoxa9* (Mm00439364_m1), *Meis1* (Mm00487664_m1), *Utx* (*Kdm6a*) (Mm00801998_m1), *Men1* (Mm00484957_m1). Quality of extracted RNA for sequencing was assessed by RIN using a Bioanalyzer (Agilent) and quantified by TapeStation (Agilent). Poly(A) mRNA enrichment and library preparation was performed using the NEBNext Poly(A) mRNA Magnetic Isolation Module and NEBNext Ultra II RNA Library Prep kit (NEB). Sequencing was done using the Illumina

NextSeq500 to obtain >20 million 75bp single-end or 37bp paired-end reads per sample or at Genewiz (HiSeq, 150bp, paired end) (Illumina, South Plainfield, NJ, USA).

Cloning of sgRNA library targeting mouse chromatin regulators

sgRNA sequences (six per gene) targeting 616 mouse chromatin regulators (for a total of 3,696 sgRNAs) (Supplementary Table 1) were designed using the Broad Institute sgRNA Designer tool[91]. We also included 36 non-targeting control sgRNAs obtained from the GeCKOv2 Mouse CRISPR library[92] (for a total of 3,732 sgRNAs). This library was divided into 6 pools (each composed of 616 targeting and 6 non-targeting sgRNAs), synthesized by Agilent Technologies, and cloned into the pUSEPR lentiviral vector[93] using a modified version of the protocol published by Doench et al[91] to ensure a library representation of >10,000X. Briefly, each sub-pool was selectively amplified using barcoded forward and reverse primers that append cloning adapters at the 5' and 3' ends of the sgRNA insert (Supplementary Table 1), purified using the QIAquick PCR Purification Kit (Qiagen), and ligated into BsmBI-digested and dephosphorylated pUSEPR vector using high-concentration T4 DNA ligase (NEB). A minimum of 1.2 ug of ligated pUSEPR plasmid DNA per sub-pool was electroporated into Endura electrocompetent cells (Lucigen), recovered for one hour at 37°C, plated across four 15cm LB-Carbenicillin plates (Teknova), and incubated at 37°C for 16 hours. The total number of bacterial colonies per sub-pool was quantified using serial dilution plates to ensure a library representation of >10,000X (>6.2 million colonies per sub-pool). The next morning, bacterial colonies were scraped and briefly expanded for 4 hours at 37°C in 500mL of LB-Carbenicillin. Plasmid DNA was isolated using the Plasmid Plus Maxi Kit (Qiagen).

To assess sgRNA distribution in each of the sub-pools, as well as the master pool (composed of equimolar amounts of plasmid DNA from each individual sub-pool), we amplified the sgRNA target region using primers that append Illumina sequencing adapters on the 5' and 3' ends of the

amplicon, as well as a random nucleotide stagger and unique demultiplexing barcode on the 5' end (Supplementary Table 1). Library amplicons were size-selected on a 2.5% agarose gel, purified using the QIAquick Gel Extraction Kit (Qiagen), and sequenced on an Illumina NextSeq instrument (75nt single end reads).

Chromatin-focused CRISPR-Cas9 genetic screening

To ensure that most cells harbor a single sgRNA integration event, we determined the volume of viral supernatant that would achieve an MOI of ~0.3 upon spinfection of a population of Cas9-expressing leukemia cells. Briefly, cells were plated at a concentration of $2.5x10^5$ per well in 12-well plates along with increasing volumes of master pool viral supernatant (0, 25, 100, 200, 500, 1000, and 2000µL) and polybrene (10 µg/mL, EMD Millipore). Cells were then centrifuged at 1,500rpm for 2 hours at 37°C and incubated at 37°C overnight. Viral infection efficiency was determined by the percentage of tRFP+ cells assessed by flow cytometry on an LSRFortessa (BD Biosciences) instrument 72 hours post infection.

Each step of the screen - from infection to sequencing - was optimized to achieve a minimum representation of 1000X. To ensure a representation of 1000X at the transduction step, we spinfected a total of 20 million cells across seven 12-well plates in triplicate (for a total of twenty one 12-well plates) using the volume of viral supernatant that would achieve a 30% infection rate (6 million transduced cells per technical replicate).

24 hours after infection, cells were pooled into 2 x T225 flasks (Corning) per infection replicate and selected with 2.5µg/mL puromycin (Gibco) for 4 days. Subsequently, 6 million puromycin-selected cells were pelleted and stored at -20°C (T0/Input population) while the rest were plated into either DMSO- or MI-503-containing media (at an IC50 concentration) and cultured until the population reached 12 cumulative population doublings (TF/Final). At least 6 million cells were

harvested and pelleted for this final time point. Genomic DNA from MLL-AF9 cells was isolated using the DNeasy Blood & Tissue Kit (Qiagen) following the manufacturer's guidelines.

As previously published[94], we assumed that each cell contains approximately 6.6 pg of genomic DNA (gDNA). Therefore, deconvolution of the screen at 1000X required sampling ~4 million x 6.6 pg of gDNA, or ~26.4 ug. We employed a modified 2-step PCR version of the protocol published by Doench et al[91]. Briefly, we perform an initial “enrichment” PCR, whereby the integrated sgRNA cassettes are amplified from gDNA, followed by a second PCR to append Illumina sequencing adapters on the 5’ and 3’ ends of the amplicon, as well as a random nucleotide stagger and unique demultiplexing barcode on the 5’ end. Each “PCR1” reaction contains 25μL of Q5 High-Fidelity 2X Master Mix (NEB), 2.5μL of Nuc PCR#1 Fwd Primer (10μM), 2.5μL of Nuc PCR#1 Rev Primer (10μM), and 5μg of gDNA in 20μL of water (for a total volume of 50μL per reaction). The number of PCR1 reactions is scaled accordingly; therefore, we performed six PCR1 reactions per technical replicate, per time point (T0 or TF), and per condition (DMSO or MI-503). PCR1 amplicons were purified using the QIAquick PCR Purification Kit (Qiagen) and used as template for “PCR2” reactions. Each PCR2 reaction contains 25μL of Q5 High-Fidelity 2X Master Mix (NEB), 2.5μL of a unique Nuc PCR#2 Fwd Primer (10μM), 2.5μL of Nuc PCR#2 Rev Primer (10μM), and 300ng of PCR1 product in 20μL of water (for a total volume of 50μL per reaction). We performed two PCR2 reactions per PCR1 product. Library amplicons were size-selected on a 2.5% agarose gel, purified using the QIAquick Gel Extraction Kit (Qiagen), and sequenced on an Illumina NextSeq500 instrument (75nt single end reads). All primer sequences are available in Supplementary Table 1. PCR Program for PCR1 and PCR2: 1) 98°C x 30s; 2) 98°C x 10s; 3) 65°C x 30s; 4) 72°C x 30s; 5) Go to step 2 x 24 cycles; 6) 72°C x 2 min; 7) 4°C forever.

<u>Genome-wide CRISPR-Cas9 genetic screening</u>

Paired mouse genome-scale CRISPR-Cas9 screening libraries (M1/M2) were provided by Shengqing Gu and Xiaole Shirley Liu (Addgene Pooled Library #1000000173). The M1 and M2 libraries cover protein coding genes of the genome with a total of 10 guide RNAs per gene. Lentivirus was produced using each separate library pool and used to transduce each $5x10^8$ MLL-AF9 cells at low MOI. 48 hours after library transduction, cells were selected with blasticidin (5ug/ml). After 5 days of antibiotic selection, a baseline (T0) sample was collected, and cells were cultured in duplicate before harvest of terminal samples after 12 days (TF). Subsequently, genomic DNA was isolated using phenol-chloroform extraction and sgRNA libraries were deconvoluted using next-generation sequencing essentially as described above.

Analysis of CRISPR-Cas9 genetic screen data

FASTQ files were processed and trimmed to retrieve sgRNA target sequences followed by alignment to the reference sgRNA library file. Sequencing read counts were summarized at gene level per sample and used as input to run differential analysis using DESeq2 package. The log2 fold change values were used as 'Gene Score' for the final visualization. Genome-wide screening data was analyzed using MAGeCK MLE essentially as described in the original publication[95]. See Supplementary Table 2 for all raw screening data.

Growth competition assays

Cas9-expressing cells were virally transduced with the designated constructs (pUSEPR-sgRNA, pUSEPB-sgRNA, pCDH-cDNA) in 12-well plates at 30-40% infection rate (three infection replicates). Cells were monitored by flow cytometry over time using an LSRFortessa (BD Biosciences) flow cytometer and relative growth of sgRNA-containing cells was assesed. Flow cytometry data was analyzed with FlowJo software (BD Biosciences). The percentage of single positive (SP) (tRFP+ or BFP+) or double positive (DP) (tRFP+/BFP+) cells was normalized to their respective "T0" time-point values (assessed on day 2 or 3 post transduction, as indicated in

the Fig.legend). Normalized values were log2-transformed, and the differential fitness of cells was calculated as follow:

Differential Fitness = log2(Normalized DP) - log2(Normalized SP)

Chromatin immunoprecipitation (ChIP)

Cross-linking ChIP in mouse leukemia and NIH-3T3 cells was performed with 10-20x10^7 cells per immunoprecipitation. After drug (or vehicle) treatment, cells were collected, washed once with ice-cold PBS, and flash-frozen. Cells were resuspended in ice-cold PBS and cross-linked using 1% paraformaldehyde (PFA) (Electron Microscopy Sciences) for 5 minutes at room temperature with gentle rotation. Unreacted PFA was quenched with glycine (final concentration 125mM) for 5 minutes at room temperature with gentle rotation. Cells were washed once with ice-cold PBS and pelleted by centrifugation (800g for 5 minutes). To obtain a soluble chromatin extract, cells were resuspended in 1mL of LB1 (50mM HEPES pH 7.5, 140mM NaCl, 1mM EDTA, 10% glycerol, 0.5% NP-40, 0.25% Triton X-100, 1X complete protease inhibitor cocktail) and incubated at 4°C for 10 minutes while rotating. Samples were centrifuged (1400g for 5 minutes), resuspended in 1mL of LB2 (10mM Tris-HCl pH 8.0, 200mM NaCl, 1mM EDTA, 0.5mM EGTA, 1X complete protease inhibitor cocktail), and incubated at 4°C for 10 minutes while rotating. Finally, samples were centrifuged (1400g for 5 minutes) and resuspended in 1mL of LB3 (10mM Tris-HCl pH 8.0, 100mM NaCl, 1mM EDTA, 0.5mM EGTA, 0.1% sodium deoxycholate, 0.5% N-Lauroylsarcosine, 1X complete protease inhibitor cocktail). Samples were homogenized by passing 7-8 times through a 28-gauge needle and Triton X-100 was added to a final concentration of 1%. Chromatin extracts were sonicated for 14 minutes using a Covaris E220 focused ultrasonicator. Lysates were centrifuged at maximum speed for 10 minutes at 4°C and 5% of supernatant was saved as input DNA. Beads were prepared by incubating in 0.5% BSA in PBS and antibodies overnight (100µL of Dynabeads Protein A or Protein G (Invitrogen) plus 20µL of

antibody). Antibodies used were: anti-Menin (Bethyl, A300-105A), anti-UTX (Bethyl, A302-374A), anti-MLL1 (N-term-specific, Bethyl, A300-086A), anti-MLL3/4 (kindly provided by the Wysocka laboratory[41], anti-NF-YA (Santa Cruz Biotechnology, sc-17753), anti-H3K4me1 (abcam, ab8895), anti-H3K4me3 (Active Motif, 39159), and anti-H4K16ac (Active Motif, 39167). Antibody-Beads mixes were washed with 0.5% BSA in PBS and then added to the lysates overnight while rotating at 4°C. Beads were then washed six times with RIPA buffer (50mM HEPES pH 7.5, 500mM LiCl, 1mM EDTA, 0.7% sodium-deoxycholate, 1% NP-40) and once with TE-NaCl Buffer (10mM Tris-HCl pH 8.0, 50mM NaCl, 1mM EDTA). Chromatin was eluted from beads in Elution buffer (50mM Tris-HCl pH 8.0, 10mM EDTA, 1% SDS) by incubating at 65°C for 30 minutes while shaking, supernatant was removed by centrifugation, and crosslinking was reversed by further incubating chromatin overnight at 65°C. The eluted chromatin was then treated with RNase A (10mg/mL) for 1 hour at 37°C and with Proteinase K (Roche) for 2 hours at 55°C. DNA was purified by using phenol-chloroform extraction followed with ethanol precipitation. The NEBNext Ultra II DNA Library Prep kit was used to prepare samples for sequencing on an Illumina NextSeq500 (75bp read length, single-end, or 37bp read length, paired-end).

ChIP-Seq analysis

ChIP-sequencing samples were sequenced using the Illumina NextSeq500. ChIP-seq reads were aligned using Rsubread's align method and predicted fragment lengths calculated by the ChIPQC R Bioconductor package[96, 97]. Normalized, fragment extended signal bigWigs were created using the rtracklayer R Bioconductor package. Peak calls were made in MACS2 software[98]. Read counts in peaks were calculated using the featureCounts method in the Rsubread library[97]. Differential ChIP-seq signal were identified using the binomTest from the edgeR R Bioconductor package[99]. Annotation of genomic regions to genes, biological functions, and pathways were performed using the ChIPseeker R Bioconductor package[100]. Meta-peak plots were produced using the soGGi package and ChIP-seq signal heatmaps generated using the Deeptools and

profileplyr software[101]. Plots showing ChIP-Seq read signal over transcription start sites (TSSs) were made with the ngs.plot software package (v2.61) (ref. 102). Overlaps between peak sets were determined using the ChIPpeakAnno R Bioconductor package with a maximum gap between peaks set to 1kb (ref. 103). Peaks were annotated with both genes and the various types of genomic regions using the ChIPseeker R Bioconductor package[100]. Range-based heatmaps showing signal over genomic regions were generated using the soGGi and profileplyr R Bioconductor package to quantify read signal and group the peak ranges and the deepTools software package (v3.3.1) to generate the heatmaps[101]. Any regions included in the ENCODE blacklisted regions of the genome were excluded from all region-specific analyses[104]. For some ChIP-seq experiments, raw Illumina NextSeq BCL files were converted to FASTQs using Illumina bcl2fastq v02.14.01.07 and reads trimmed using Trimmomatic v0.36 (phred quality threshold 33) and uploaded to the to the Basepair-server (basepairtech.com). Alignment and ChIP-seq QC was performed on the basepair platform (Bowtie2). Peak calling was performed using MACS (v.1.4) within the basepair platform utilizing the default parameters.

RNA-Seq analysis

RNA-Seq samples were sequenced using the Illumina NextSeq500. Transcript abundance was computed from FASTQ files using Salmon and the GENCODE reference transcript sequences, transcript counts were imported into R with the tximport R Bioconductor package, and differential gene expression was determined with the DESeq2 R Bioconductor package[105-107]. The data was visualized using the ggplot2 R package. Normalized counts were extracted from the DESeq2 results and z-scores for the indicated gene sets were visualized using both heatmaps and boxplots. Heatmaps showing gene expression changes across samples were generated using the pheatmap R package and boxplots were made with the ggplot2 R package. Gene ontology analysis using the KEGG 2019 database was performed using the Enrichr tool[56],[65].

Statistical analyses

Statistical tests were used as indicated in Figure legends. Generation of plots and statistical analyses were performed using Prism 8 (GraphPad). Error bars represent standard deviation, unless otherwise noted. We used Student's t-test (unpaired, two-tailed) to assess significance between treatment and control groups, and to calculate P values. $P<0.05$ was considered statistically significant.

Source data availability

Data supporting the findings of this study are reported in Extended Figures 1-23 and Supplementary Tables 1-4. All raw data corresponding to high-throughput approaches (CRISPR screens, RNA-Seq, and ChIP-Seq) will be available through NCBI GEO. All reagents and materials generated in this study will be available to the scientific community through Addgene and/or MTAs. Further information and requests for resources and reagents should be directed to and will be fulfilled by the Lead Contacts: C. David Allis (alliscd@rockefeller.edu), Scott W. Lowe (lowes@mskcc.org), and Scott. A. Armstrong (Scott_Armstrong@dfci.harvard.edu).

REFERENCES

1. Guru, S.C. et al. Menin, the product of the MEN1 gene, is a nuclear protein. *Proceedings of the National Academy of Sciences* **95**, 1630-1634 (1998).
2. Hughes, C.M. et al. Menin associates with a trithorax family histone methyltransferase complex and with the Hoxc8 locus. *Mol Cell* **13**, 587-597 (2004).
3. Milne, T.A. et al. Menin and MLL cooperatively regulate expression of cyclin-dependent kinase inhibitors. *Proceedings of the National Academy of Sciences* **102**, 749-754 (2005).
4. Yokoyama, A. et al. The menin tumor suppressor protein is an essential oncogenic cofactor for MLL-associated leukemogenesis. *Cell* **123**, 207-218 (2005).

5. Bres, V., Yoshida, T., Pickle, L. & Jones, K.A. SKIP interacts with c-Myc and Menin to promote HIV-1 Tat transactivation. *Mol Cell* **36**, 75-87 (2009).

6. Agarwal, S.K. & Jothi, R. Genome-wide characterization of menin-dependent H3K4me3 reveals a specific role for menin in the regulation of genes implicated in MEN1-like tumors. *PLoS ONE* **7**, e37952 (2012).

7. Huang, J. et al. The same pocket in menin binds both MLL and JUND but has opposite effects on transcription. *Nature 2018* **482**, 542-546 (2012).

8. Kaji, H., Canaff, L., Lebrun, J.J., Goltzman, D. & Hendy, G.N. Inactivation of menin, a Smad3-interacting protein, blocks transforming growth factor type beta signaling. *Proceedings of the National Academy of Sciences* **98**, 3837-3842 (2001).

9. Sowa, H. et al. Inactivation of menin, the product of the multiple endocrine neoplasia type 1 gene, inhibits the commitment of multipotential mesenchymal stem cells into the osteoblast lineage. *J Biol Chem* **278**, 21058-21069 (2003).

10. Yokoyama, A. & Cleary, M.L. Menin critically links MLL proteins with LEDGF on cancer-associated target genes. *Cancer Cell* **14**, 36-46 (2008).

11. Balogh, K., Rácz, K., Patócs, A. & Hunyady, L. Menin and its interacting proteins: elucidation of menin function. *Trends Endocrinol. Metab.* **17**, 357-364 (2006).

12. Yokoyama, A. et al. Leukemia proto-oncoprotein MLL forms a SET1-like histone methyltransferase complex with menin to regulate Hox gene expression. *Mol Cell Biol* **24**, 5639-5649 (2004).

13. Wang, P. et al. Global analysis of H3K4 methylation defines MLL family member targets and points to a role for MLL1-mediated H3K4 methylation in the regulation of transcriptional initiation by RNA polymerase II. *Mol Cell Biol* **29**, 6074-6085 (2009).

14. Chandrasekharappa, S.C. et al. Positional cloning of the gene for multiple endocrine neoplasia-type 1. *Science* **276**, 404-407 (1997).

15. Jiao, Y. et al. DAXX/ATRX, MEN1, and mTOR pathway genes are frequently altered in pancreatic neuroendocrine tumors. *Science* **331**, 1199-1203 (2011).

16. Asgharian, B. et al. Cutaneous tumors in patients with multiple endocrine neoplasm type 1 (MEN1) and gastrinomas: prospective study of frequency and development of criteria with high sensitivity and specificity for MEN1. *J. Clin. Endocrinol. Metab.* **89**, 5328-5336 (2004).

17. Pei, X.-H., Bai, F., Smith, M.D. & Xiong, Y. p18Ink4c collaborates with Men1 to constrain lung stem cell expansion and suppress non-small-cell lung cancers. *Cancer Res* **67**, 3162-3170 (2007).

18. Falchetti, A. et al. Multiple endocrine neoplasia type 1 (MEN1): not only inherited endocrine tumors. *Genet. Med.* **11**, 825-835 (2009).

19. Xu, B. et al. Menin promotes hepatocellular carcinogenesis and epigenetically up-regulates Yap1 transcription. *Proc Natl Acad Sci USA* **110**, 17480-17485 (2013).

20. Krivtsov, A.V. & Armstrong, S.A. MLL translocations, histone modifications and leukaemia stem-cell development. *Nat Rev Cancer* **7**, 823-833 (2007).

21. Lemos, M.C. & Thakker, R.V. Multiple endocrine neoplasia type 1 (MEN1): analysis of 1336 mutations reported in the first decade following identification of the gene. *Hum. Mutat.* **29**, 22-32 (2008).

22. Grembecka, J. et al. Menin-MLL inhibitors reverse oncogenic activity of MLL fusion proteins in leukemia. *Nat Meth* **8**, 277-284 (2012).

23. Borkin, D. et al. Pharmacologic inhibition of the Menin-MLL interaction blocks progression of MLL leukemia in vivo. *Cancer Cell* **27**, 589-602 (2015).

24. Malik, R. et al. Targeting the MLL complex in castration-resistant prostate cancer. *Nature Medicine* **21**, 344-352 (2015).

25. Dreijerink, K.M.A. et al. Enhancer-Mediated Oncogenic Function of the Menin Tumor Suppressor in Breast Cancer. *Cell Rep* **18**, 2359-2372 (2017).

26. Krivtsov, A.V. et al. A Menin-MLL Inhibitor Induces Specific Chromatin Changes and Eradicates Disease in Models of MLL-Rearranged Leukemia. *Cancer Cell* **36**, 660-673.e611 (2019).

27. Uckelmann, H.J. et al. Therapeutic targeting of preleukemia cells in a mouse model of NPM1 mutant acute myeloid leukemia. *Science* **367**, 586-590 (2020).

28. Kurmasheva, R.T. et al. Evaluation of VTP-50469, a menin-MLL1 inhibitor, against Ewing sarcoma xenograft models by the pediatric preclinical testing consortium. *Pediatr Blood Cancer* **67**, e28284 (2020).

29. Chen, C.-W. et al. DOT1L inhibits SIRT1-mediated epigenetic silencing to maintain leukemic gene expression in MLL-rearranged leukemia. *Nature Medicine* **21**, 335-343 (2015).

30. Chang, M.-J. et al. Histone H3 lysine 79 methyltransferase Dot1 is required for immortalization by MLL oncogenes. *Cancer Res* **70**, 10234-10242 (2010).

31. Bernt, K.M. et al. MLL-rearranged leukemia is dependent on aberrant H3K79 methylation by DOT1L. *Cancer Cell* **20**, 66-78 (2011).

32. Mueller, D. et al. Misguided transcriptional elongation causes mixed lineage leukemia. *PLoS Biol* **7**, e1000249 (2009).

33. Zuber, J. et al. RNAi screen identifies Brd4 as a therapeutic target in acute myeloid leukaemia. *Nature 2018* **478**, 524-528 (2011).

34. Zuber, J. et al. An integrated approach to dissecting oncogene addiction implicates a Myb-coordinated self-renewal program as essential for leukemia maintenance. *Genes & Development* **25**, 1628-1640 (2011).

35. Milne, T.A. et al. MLL targets SET domain methyltransferase activity to Hox gene promoters. *Mol Cell* **10**, 1107-1117 (2002).

36. Nakamura, T. et al. ALL-1 is a histone methyltransferase that assembles a supercomplex of proteins involved in transcriptional regulation. *Mol Cell* **10**, 1119-1128 (2002).

37. Herz, H.-M. et al. Enhancer-associated H3K4 monomethylation by Trithorax-related, the Drosophila homolog of mammalian Mll3/Mll4. *Genes & Development* **26**, 2604-2620 (2012).

38. Hu, D. et al. The MLL3/MLL4 branches of the COMPASS family function as major histone H3K4 monomethylases at enhancers. *Mol Cell Biol* **33**, 4745-4754 (2013).

39. Lee, J. et al. A tumor suppressive coactivator complex of p53 containing ASC-2 and histone H3-lysine-4 methyltransferase MLL3 or its paralogue MLL4. *Proc Natl Acad Sci USA* **106**, 8513-8518 (2009).

40. Wang, S.-P. et al. A UTX-MLL4-p300 Transcriptional Regulatory Network Coordinately Shapes Active Enhancer Landscapes for Eliciting Transcription. *Mol Cell* **67**, 308-321.e306 (2017).

41. Dorighi, K.M. et al. Mll3 and Mll4 Facilitate Enhancer RNA Synthesis and Transcription from Promoters Independently of H3K4 Monomethylation. *Mol Cell* **66**, 568-576.e564 (2017).

42. Issaeva, I. et al. Knockdown of ALR (MLL2) reveals ALR target genes and leads to alterations in cell adhesion and growth. *Mol Cell Biol* **27**, 1889-1903 (2007).

43. Santos, M.A. et al. DNA-damage-induced differentiation of leukaemic cells as an anti-cancer barrier. *Nature 2018* **514**, 107-111 (2014).

44. Sun, Y. et al. HOXA9 Reprograms the Enhancer Landscape to Promote Leukemogenesis. *Cancer Cell* **34**, 643-658.e645 (2018).

45. Chen, C. et al. MLL3 is a haploinsufficient 7q tumor suppressor in acute myeloid leukemia. *Cancer Cell* **25**, 652-665 (2014).

46. Kooistra, S.M. & Helin, K. Molecular mechanisms and potential functions of histone demethylases. *Nat Rev Mol Cell Biol* **13**, 297-311 (2012).

47. Gažová, I., Lengeling, A. & Summers, K.M. Lysine demethylases KDM6A and UTY: The X and Y of histone demethylation. *Molecular Genetics and Metabolism* **127**, 31-44 (2019).

48. Thirman, M.J. et al. Rearrangement of the MLL gene in acute lymphoblastic and acute myeloid leukemias with 11q23 chromosomal translocations. *N Engl J Med* **329**, 909-914 (1993).

49. Meyer, C. et al. The MLL recombinome of acute leukemias in 2017. *Leukemia* **32**, 273-284 (2018).

50. Tiacci, E. et al. The NPM1 wild-type OCI-AML2 and the NPM1-mutated OCI-AML3 cell lines carry DNMT3A mutations. *Leukemia* **26**, 554-557 (2012).

51. Kuhn, M.W. et al. Targeting Chromatin Regulators Inhibits Leukemogenic Gene Expression in NPM1 Mutant Leukemia. *Cancer Discov* **6**, 1166-1181 (2016).

52. Kumar, A.R. et al. A role for MEIS1 in MLL-fusion gene leukemia. *Blood* **113**, 1756-1758 (2009).

53. Chen, Y. et al. Distinct pathways affected by menin versus MLL1/MLL2 in MLL-rearranged acute myeloid leukemia. *Exp Hematol* **69**, 37-42 (2019).

54. Lange, B. et al. Growth-Factor Requirements of Childhood Acute-Leukemia - Establishment of Gm-Csf Dependent Cell-Lines. *Blood* **70**, 192-199 (1987).

55. Scacheri, P.C. et al. Genome-wide analysis of menin binding provides insights into MEN1 tumorigenesis. *PLoS Genet* **2**, e51 (2006).

56. Wang, J.K. et al. The histone demethylase UTX enables RB-dependent cell fate control. *Genes & Development* **24**, 327-332 (2010).

57. La, P. et al. Direct binding of DNA by tumor suppressor menin. *J Biol Chem* **279**, 49045-49054 (2004).

58. Oldfield, A.J. et al. NF-Y controls fidelity of transcription initiation at gene promoters through maintenance of the nucleosome-depleted region. *Nat Commun* **10**, 3072 (2019).

59. Tsherniak, A. et al. Defining a Cancer Dependency Map. *Cell* **170**, 564-576 e516 (2017).

60. Cheng, J. et al. A role for H3K4 monomethylation in gene repression and partitioning of chromatin readers. *Mol Cell* **53**, 979-992 (2014).

61. Morgan, M.A.J. & Shilatifard, A. Reevaluating the roles of histone-modifying enzymes and their associated chromatin modifications in transcriptional regulation. *Nat Genet* **52**, 1271-1281 (2020).

62. Jang, Y. et al. H3.3K4M destabilizes enhancer H3K4 methyltransferases MLL3/MLL4 and impairs adipose tissue development. *Nucleic Acids Res* **47**, 607-620 (2019).

63. Shogren-Knaak, M. et al. Histone H4-K16 acetylation controls chromatin structure and protein interactions. *Science* **311**, 844-847 (2006).

64. Taylor, G.C., Eskeland, R., Hekimoglu-Balkan, B., Pradeepa, M.M. & Bickmore, W.A. H4K16 acetylation marks active genes and enhancers of embryonic stem cells, but does not alter chromatin compaction. *Genome Res* **23**, 2053-2065 (2013).

65. Chen, E.Y. et al. Enrichr: interactive and collaborative HTML5 gene list enrichment analysis tool. *BMC Bioinformatics* **14**, 128-114 (2013).

66. Kuleshov, M.V. et al. Enrichr: a comprehensive gene set enrichment analysis web server 2016 update. *Nucleic Acids Res* **44**, W90-97 (2016).

67. Subramanian, A. et al. Gene set enrichment analysis: a knowledge-based approach for interpreting genome-wide expression profiles. *Proceedings of the National Academy of Sciences* **102**, 15545-15550 (2005).

68. Fridman, A.L. & Tainsky, M.A. Critical pathways in cellular senescence and immortalization revealed by gene expression profiling. *Oncogene* **27**, 5975-5987 (2008).

69. Ruscetti, M. et al. NK cell-mediated cytotoxicity contributes to tumor control by a cytostatic drug combination. *Science* **362**, 1416-1422 (2018).

70. Dang, W. et al. Histone H4 lysine 16 acetylation regulates cellular lifespan. *Nature 2018* **459**, 802-807 (2009).

71. Faget, D.V., Ren, Q. & Stewart, S.A. Unmasking senescence: context-dependent effects of SASP in cancer. *Nat Rev Cancer* **19**, 439-453 (2019).

72. Tasdemir, N. et al. BRD4 Connects Enhancer Remodeling to Senescence Immune Surveillance. *Cancer Discov* **6**, 612-629 (2016).

73. Kuilman, T., Michaloglou, C., Mooi, W.J. & Peeper, D.S. The essence of senescence. *Genes & Development* **24**, 2463-2479 (2010).

74. Placke, T. et al. Requirement for CDK6 in MLL-rearranged acute myeloid leukemia. *Blood* **124**, 13-23 (2014).

75. Hirai, H., Roussel, M.F., Kato, J.Y., Ashmun, R.A. & Sherr, C.J. Novel INK4 proteins, p19 and p18, are specific inhibitors of the cyclin D-dependent kinases CDK4 and CDK6. *Mol Cell Biol* **15**, 2672-2681 (1995).

76. Fry, D.W. et al. Specific inhibition of cyclin-dependent kinase 4/6 by PD 0332991 and associated antitumor activity in human tumor xenografts. *Molecular Cancer Therapeutics* **3**, 1427-1437 (2004).

77. Sherr, C.J., Beach, D. & Shapiro, G.I. Targeting CDK4 and CDK6: From Discovery to Therapy. *Cancer Discovery* **6**, 353-367 (2016).

78. Ruscetti, M. et al. Senescence-Induced Vascular Remodeling Creates Therapeutic Vulnerabilities in Pancreas Cancer. *Cell* **181**, 424-441.e421 (2020).

79. Yang, C. et al. Acquired CDK6 amplification promotes breast cancer resistance to CDK4/6 inhibitors and loss of ER signaling and dependence. *Oncogene* **36**, 2255-2264 (2017).

80. Chen, L. et al. Autophagy inhibition contributes to the synergistic interaction between EGCG and doxorubicin to kill the hepatoma Hep3B cells. *PLoS ONE* **9**, e85771 (2014).

81. Kempinska, K. et al. Pharmacologic Inhibition of the Menin-MLL Interaction Leads to Transcriptional Repression of PEG10 and Blocks Hepatocellular Carcinoma. *Molecular Cancer Therapeutics* **17**, 26-38 (2018).

82. Svoboda, L.K. et al. Menin regulates the serine biosynthetic pathway in Ewing sarcoma. *The Journal of pathology* **245**, 324-336 (2018).

83. Klossowski, S. et al. Menin inhibitor MI-3454 induces remission in MLL1-rearranged and NPM1-mutated models of leukemia. *J Clin Invest* **130**, 981-997 (2020).

84. Qiu, H. et al. MEN1 deficiency leads to neuroendocrine differentiation of lung cancer and disrupts the DNA damage response. *Nat Commun* **11**, 1009 (2020).

85. Schnepp, R.W. et al. Menin induces apoptosis in murine embryonic fibroblasts. *J Biol Chem* **279**, 10685-10691 (2004).

86. Karnik, S.K. et al. Menin regulates pancreatic islet growth by promoting histone methylation and expression of genes encoding p27Kip1 and p18INK4c. *Proceedings of the National Academy of Sciences* **102**, 14659-14664 (2005).

87. Chen, B. et al. Dynamic imaging of genomic loci in living human cells by an optimized CRISPR/Cas system. *Cell* **155**, 1479-1491 (2013).

88. Akama-Garren, E.H. et al. A Modular Assembly Platform for Rapid Generation of DNA Constructs. *Sci. Rep.* **6**, 16836-16839 (2016).

89. Krivtsov, A.V. et al. Transformation from committed progenitor to leukaemia stem cell initiated by MLL-AF9. *Nature 2018* **442**, 818-822 (2006).

90. Krivtsov, A.V. et al. Patient Derived Xenograft (PDX) Models Faithfully Recapitulate The Genetic Composition Of Primary AML. *Blood* **122**, 1328-1328 (2013).

91. Doench, J.G. et al. Optimized sgRNA design to maximize activity and minimize off-target effects of CRISPR-Cas9. *Nat Biotechnol* **34**, 184-191 (2016).

92. Sanjana, N.E., Shalem, O. & Zhang, F. Improved vectors and genome-wide libraries for CRISPR screening. *Nat Meth* **11**, 783-784 (2014).

93. Phillips, R.E. et al. Target identification reveals lanosterol synthase as a vulnerability in glioma. *Proc Natl Acad Sci USA* **116**, 7957-7962 (2019).

94. Strezoska, Ž. et al. Optimized PCR conditions and increased shRNA fold representation improve reproducibility of pooled shRNA screens. *PLoS ONE* **7**, e42341 (2012).

95. Li, W. et al. Quality control, modeling, and visualization of CRISPR screens with MAGeCK-VISPR. *Genome Biol* **16**, 281 (2015).

96. Carroll, T.S., Liang, Z., Salama, R., Stark, R. & de Santiago, I. Impact of artifact removal on ChIP quality metrics in ChIP-seq and ChIP-exo data. *Front. Genet.* **5** (2014).

97. Liao, Y., Smyth, G.K. & Shi, W. The R package Rsubread is easier, faster, cheaper and better for alignment and quantification of RNA sequencing reads. *Nucleic Acids Res* **47**, e47 (2019).

98. Zhang, Y. et al. Model-based analysis of ChIP-Seq (MACS). *Genome Biol* **9**, R137-139 (2008).

99. Nikolayeva, O. & Robinson, M.D. edgeR for differential RNA-seq and ChIP-seq analysis: an application to stem cell biology. *Methods Mol. Biol.* **1150**, 45-79 (2014).

100. Yu, G., Wang, L.-G. & He, Q.-Y. ChIPseeker: an R/Bioconductor package for ChIP peak annotation, comparison and visualization. *Bioinformatics* **31**, 2382-2383 (2015).

101. Ramírez, F., Dündar, F., Diehl, S., Grüning, B.A. & Manke, T. deepTools: a flexible platform for exploring deep-sequencing data. *Nucleic Acids Res* **42**, W187-191 (2014).

102. Shen, L., Shao, N., Liu, X. & Nestler, E. ngs.plot: Quick mining and visualization of next-generation sequencing data by integrating genomic databases. *BMC Genomics* **15**, 284-214 (2014).

103. Zhu, L.J. et al. ChIPpeakAnno: a Bioconductor package to annotate ChIP-seq and ChIP-chip data. *BMC Bioinformatics* **11**, 10 (2010).

104. Amemiya, H.M., Kundaje, A. & Boyle, A.P. The ENCODE Blacklist: Identification of Problematic Regions of the Genome. *Sci. Rep.* **9**, 9354-9355 (2019).

105. Patro, R., Duggal, G., Love, M.I., Irizarry, R.A. & Kingsford, C. Salmon provides fast and bias-aware quantification of transcript expression. *Nat Meth* **14**, 417-419 (2017).

106. Love, M.I., Huber, W. & Anders, S. Moderated estimation of fold change and dispersion for RNA-seq data with DESeq2. *Genome Biol* **15**, 550 (2014).

107. Soneson, C., Love, M.I. & Robinson, M.D. Differential analyses for RNA-seq: transcript-level estimates improve gene-level inferences. *F1000Research* **4**, 1521 (2015).

FIGURE 1 - CRISPR screens uncover functional interplay between the mammalian MLL1/2 and MLL3/4 chromatin modifying complexes

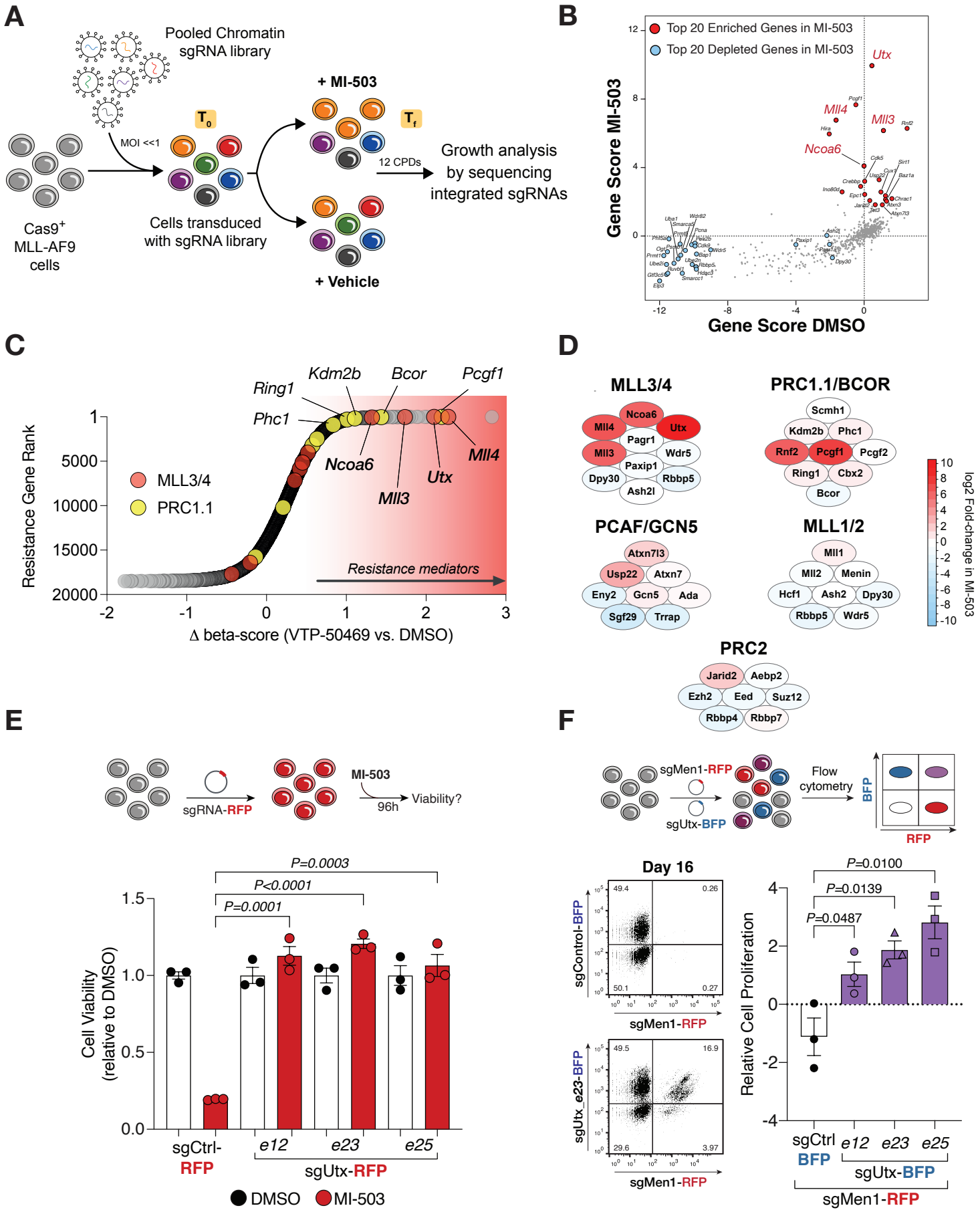

FIGURE 2 - Menin restricts chromatin occupancy of UTX at promoter regions

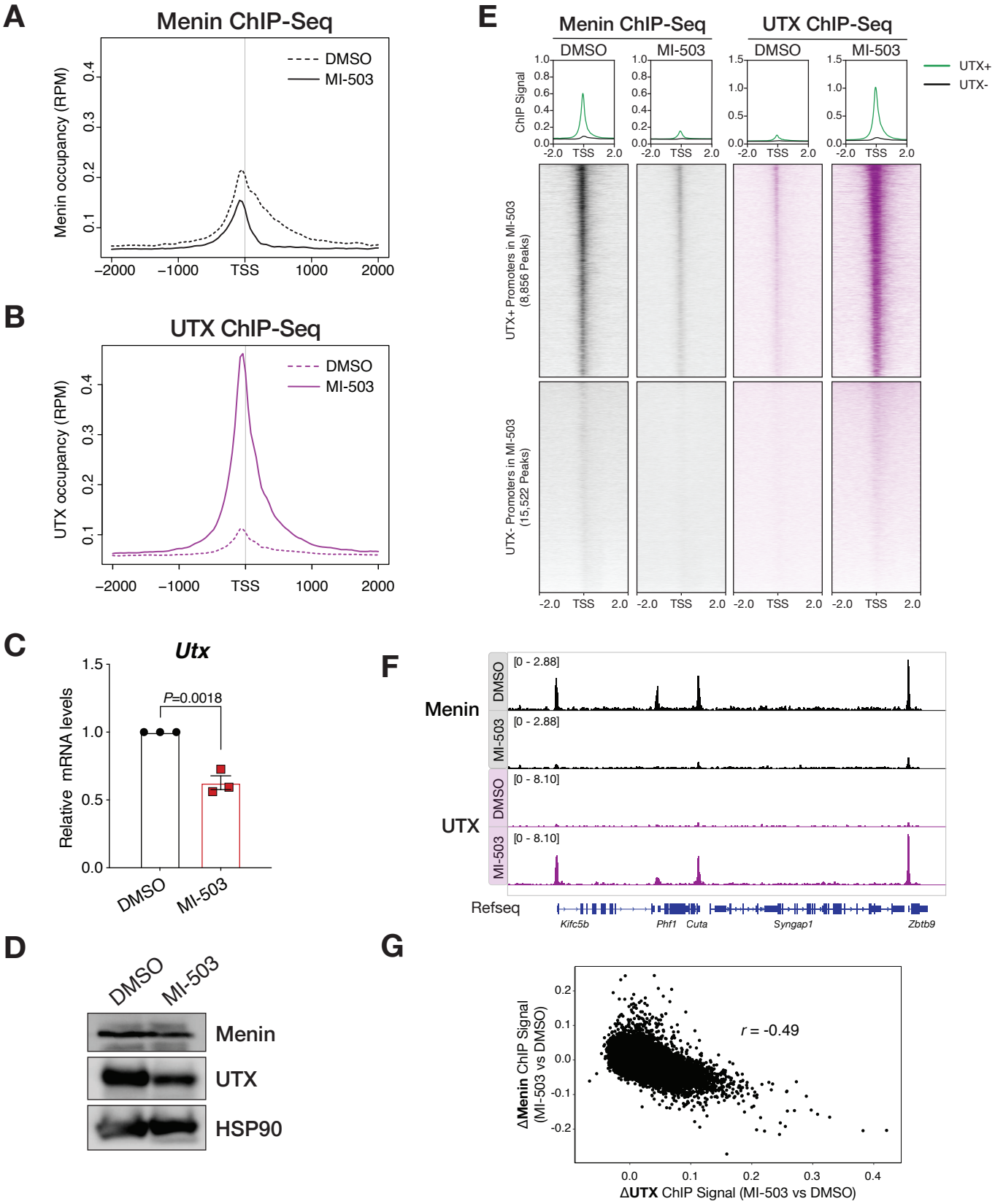

FIGURE 3 - Promoter regulation by the MLL3/4 complex dictates outcome of Menin inhibition

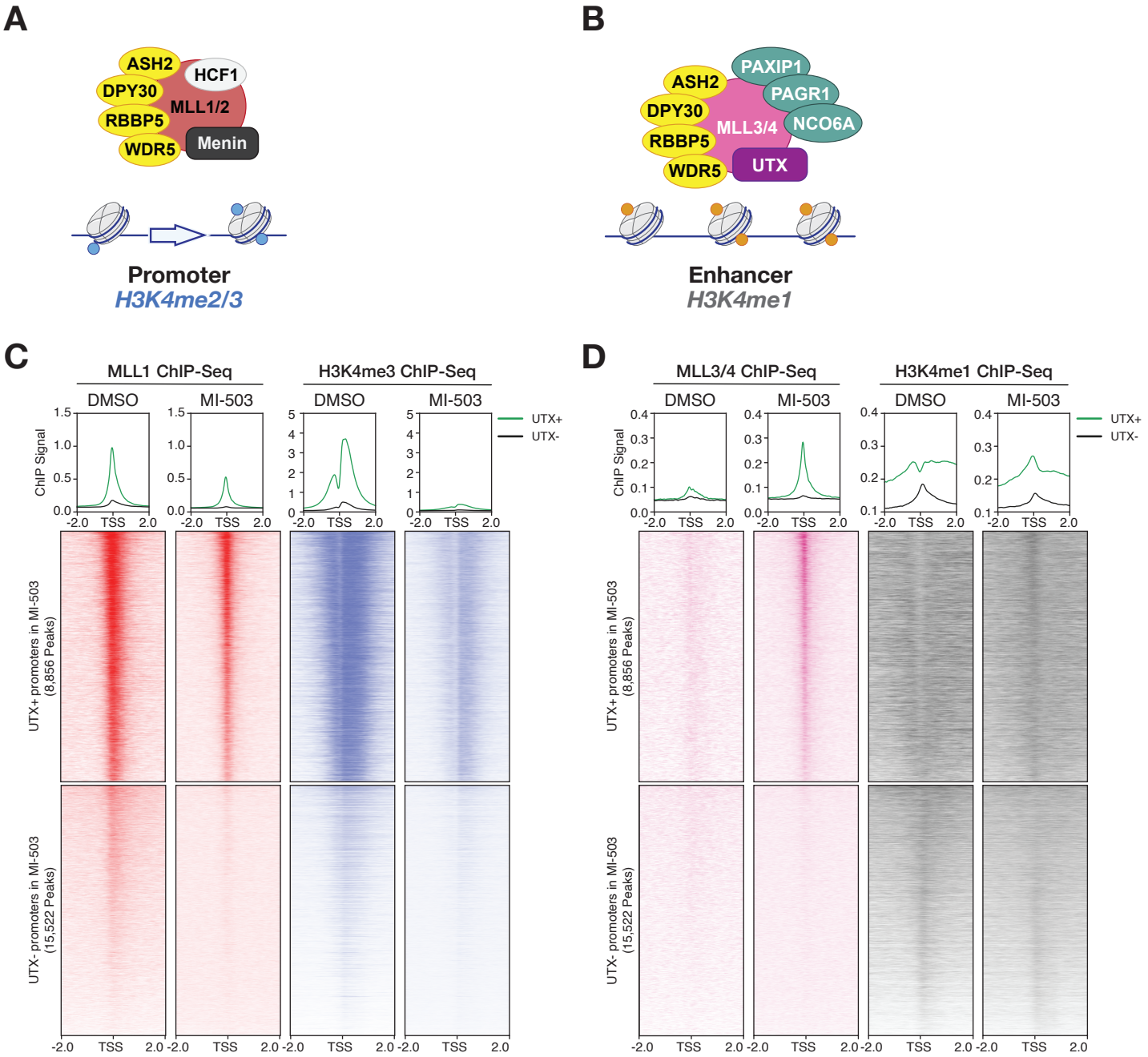

FIGURE 4 - Reciprocal transcriptional regulation of tumor suppressive pathways by Menin and UTX

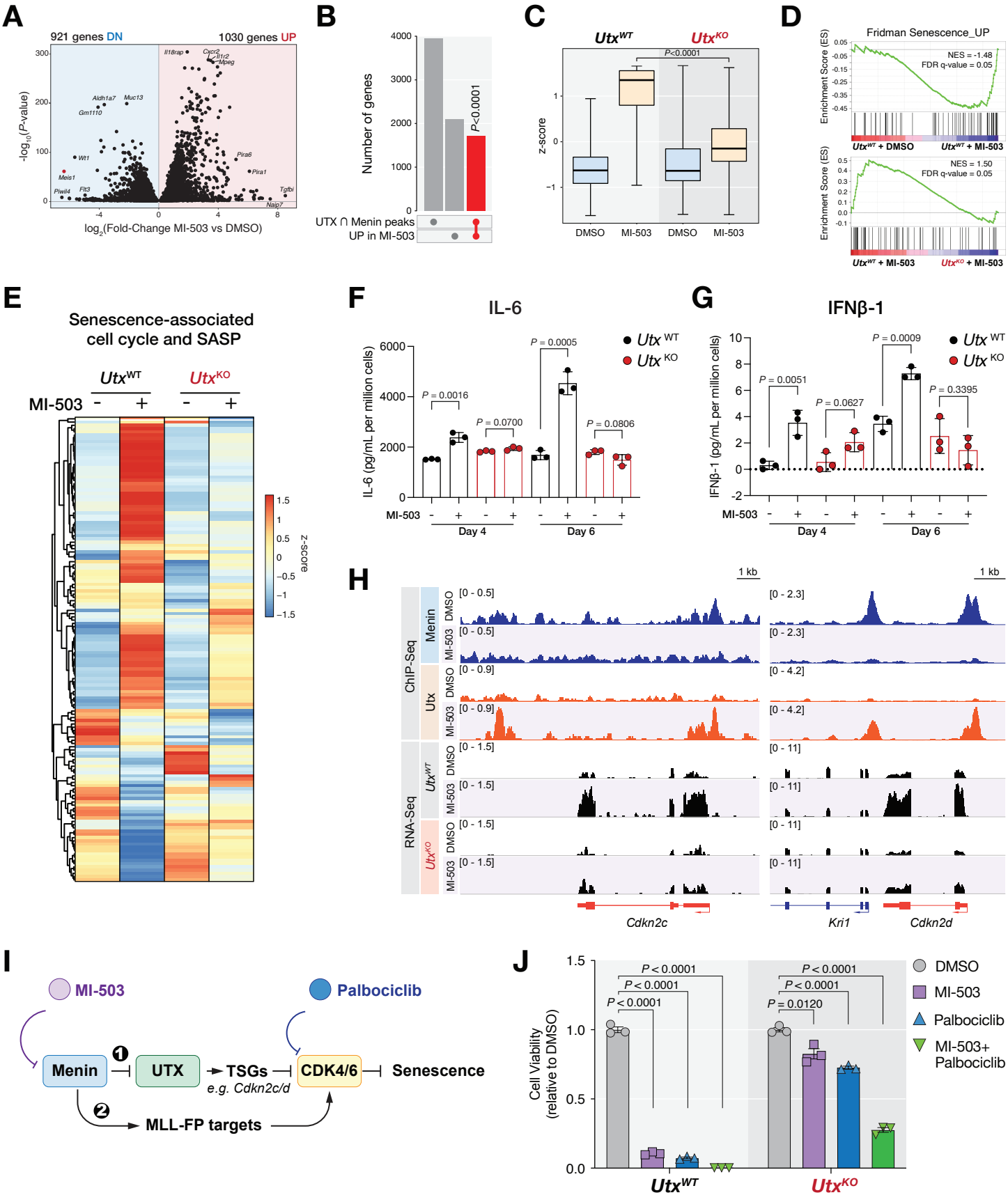

FIGURE 5 - *In vivo* response to Menin-MLL inhibition is accompanied by induction of MLL3/4-UTX-dependent tumor suppressive programs

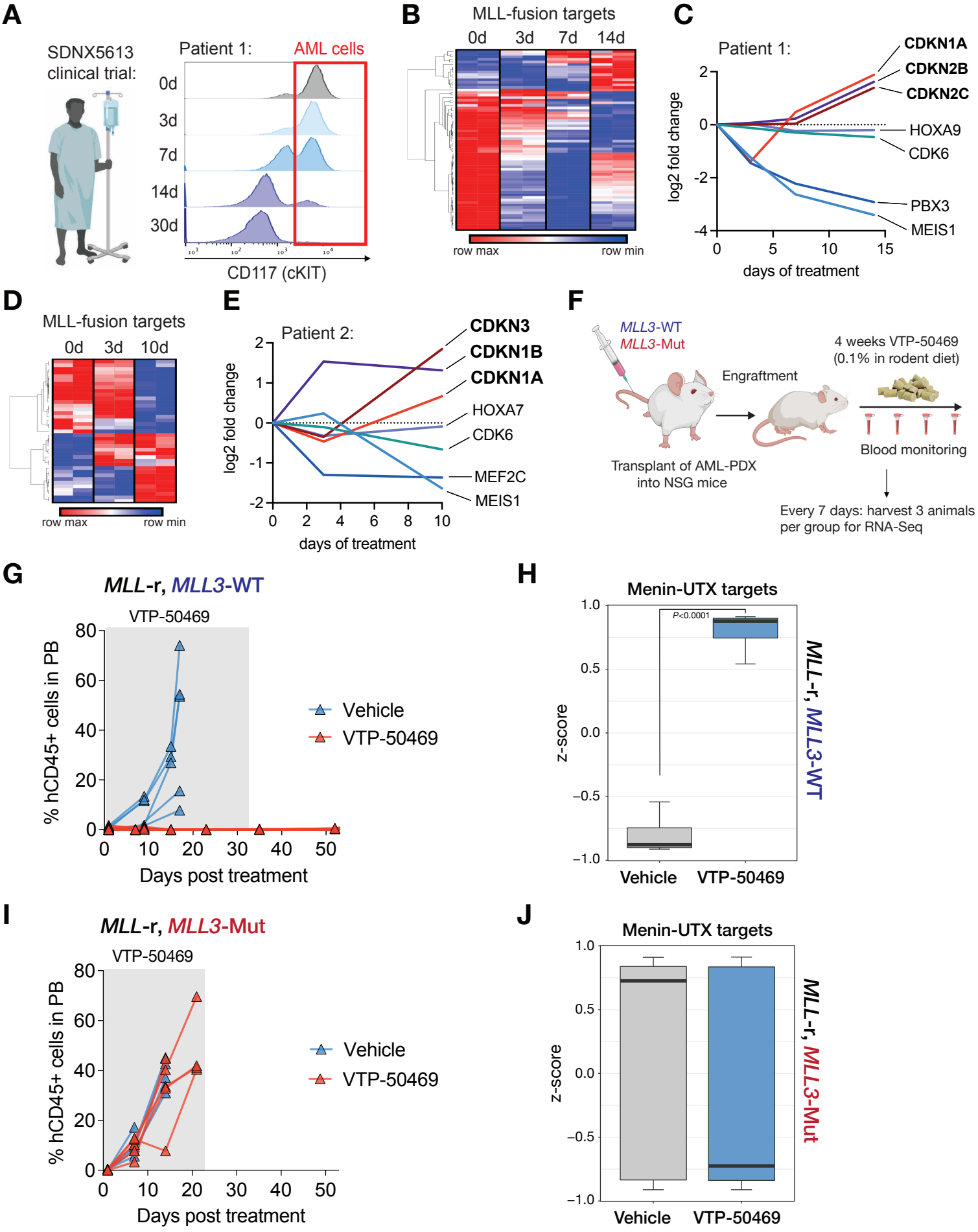

FIGURE 6 - Molecular switch between the mammalian MLL complexes dictates cellular response to Menin-MLL inhibition

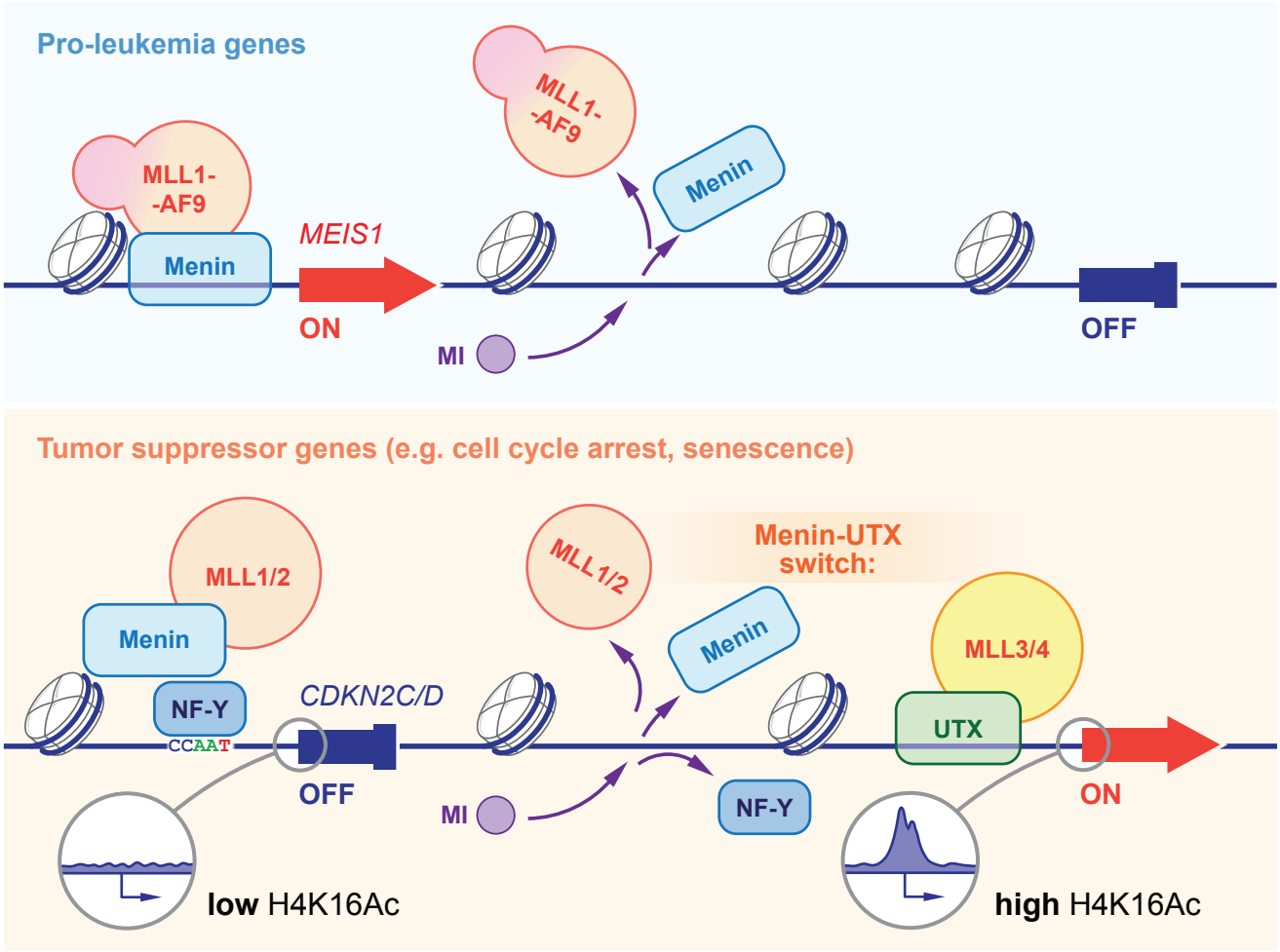

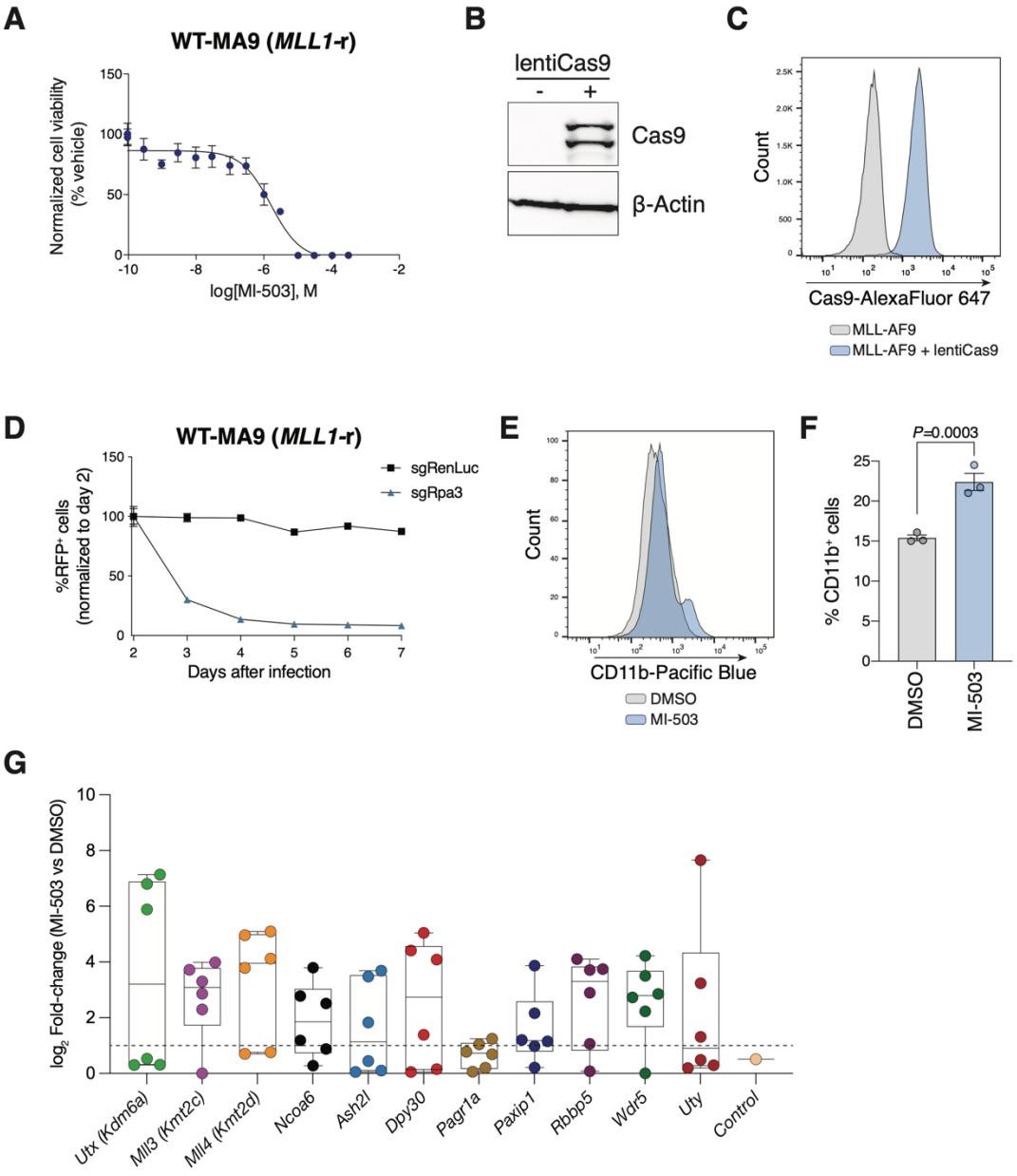

Extended Figure 1. Characterization of Cas9-expressing mouse MLL-AF9 leukemia cells. **(A)** Dose response curve analysis of mouse MLL-AF9 leukemia (WT-MA9) cells treated with DMSO (vehicle) or MI-503 (Menin inhibitor) for 96 hours (mean±SEM, n=3 replicates). **(B)** Western blot analysis of Cas9-expressing mouse MLL-AF9 leukemia cells. **(C)** Distribution of Cas9-expressing MLL-AF9 leukemia cells determined by intracellular staining of Cas9 and flow cytometry. **(D)** Growth competition assay to determine enzymatic activity of Cas9 in mouse MLL-AF9 leukemia cells. **(E)** CD11b cell surface expression measured by flow cytometry after DMSO

(grey) or MI-503 (blue) treatment of MLL-AF9 leukemia cells for 96 hours. **(F)** Quantification of %CD11b positive cells after DMSO or MI-503 treatment for 96 hours (mean±SEM, n=3 replicates, *P*-value calculated by Student's t-test). **(G)** Log_2-fold change of individual sgRNAs from MI-503-treated vs DMSO-treated CRISPR screens in mouse MLL-AF9 leukemia cells.

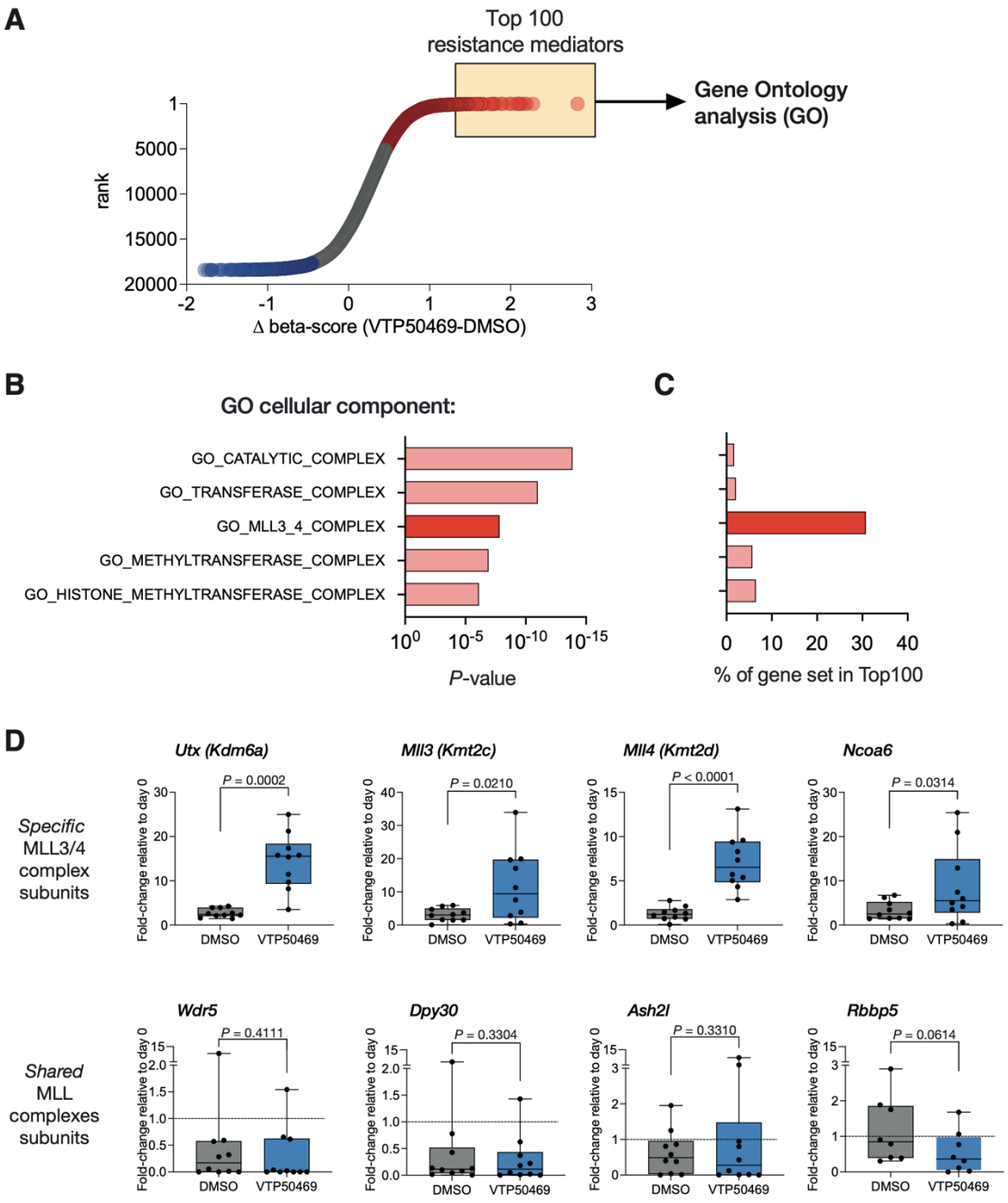

Extended Figure 2. Genome-wide CRISPR screening identifies the MLL3/4-UTX complex as a determinant of response to Menin-MLL inhibition. (A) Genome-wide screening data showing gene-level ranking based on differential enrichment of sgRNAs under Menin-MLL inhibitor treatment (VTP-50469) relative to vehicle (DMSO). Differential (Δ) beta-score between VTP-50469 and DMSO conditions was calculated using MaGeCK. A positive Δ beta-score

denotes enrichment of specific gene-targeting sgRNAs. A negative Δ beta-score denotes depletion of specific gene-targeting sgRNAs. Red circles denote genes represented by enriched sgRNAs (genes whose inactivation promotes resistance to Menin-MLL inhibition). Blue circles denote genes represented by depleted sgRNAs (genes whose inactivation promotes sensitivity to Menin-MLL inhibition). The top 100 candidate mediators of resistance were selected for gene ontology (GO) analysis. **(B)** Top-scoring GO categories based on *P*-values obtained from GO analysis. **(C)** Percentage of genes within a given gene set that scored among the top 100 candidate mediators of resistance. **(D)** Fold change of individual sgRNAs relative to T0 from either VTP-50469-treated or DMSO-treated cells (*P*-value calculated by Student's t-test).

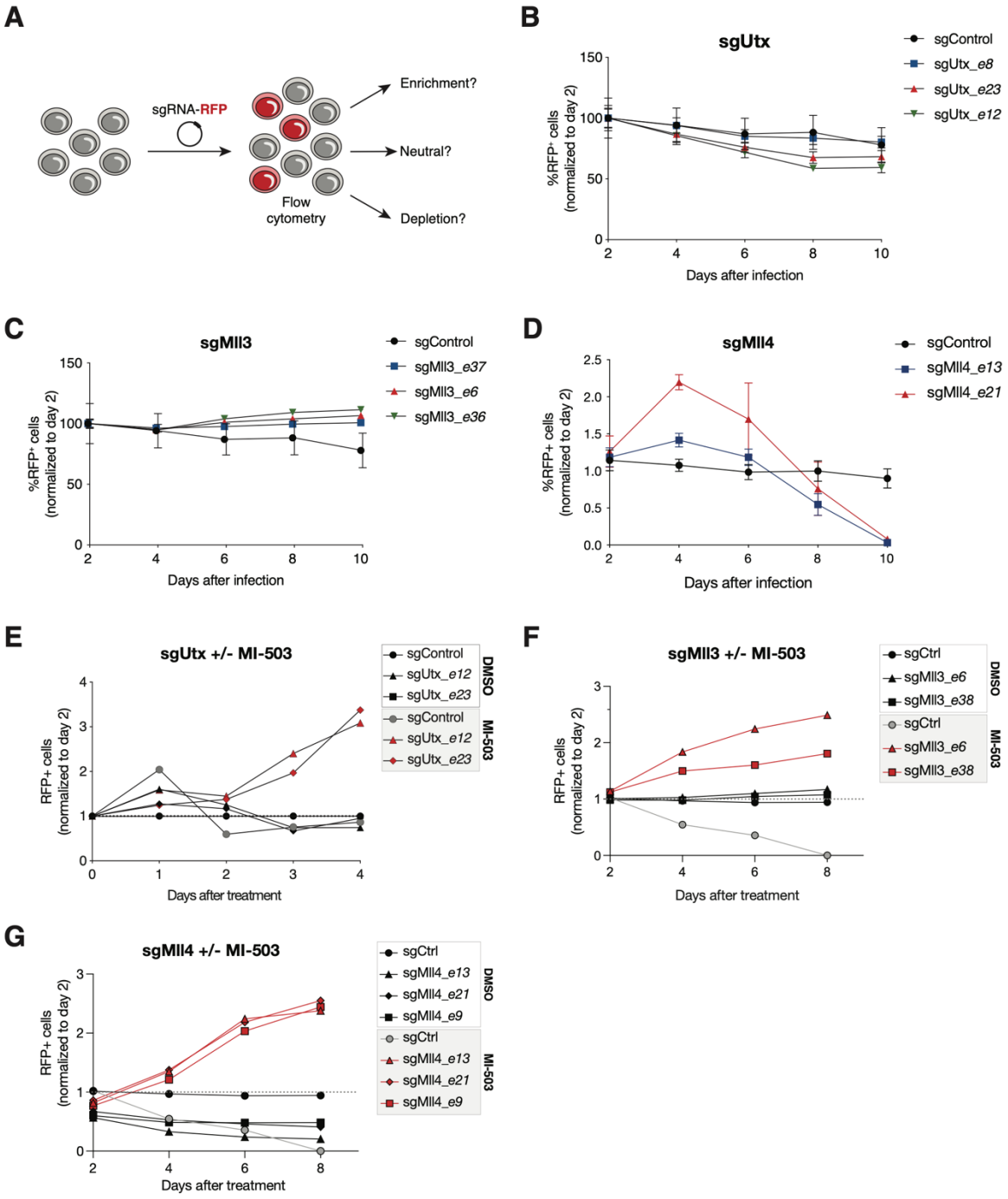

Extended Figure 3. The MLL3/4-UTX complex dictates therapeutic outcome of Menin-MLL inhibition. (A) Layout of growth competition assay to assess the effect of genetic loss of *Utx*, *Mll3*, or *Mll4* in MLL-AF9 leukemia cells in response to Menin-MLL inhibition. **(B)** Growth competition assay in mouse MLL-AF9 (WT-MA9) cells. Graph shows the relative growth of cells

infected with RFP-tagged *Utx* (*Kdm6a*) sgRNAs measured by flow cytometry (mean±SEM, n=3 infection replicates). sgControl targets a non-genic region in chromosome 8 as negative control. **(C)** Growth competition assay in mouse MLL-AF9 (WT-MA9) cells. Graph shows the relative growth of cells infected with RFP-tagged *Mll3* (*Kmt2c*) sgRNAs measured by flow cytometry (mean±SEM, n=3 infection replicates). sgControl targets a non-genic region in chromosome 8 as negative control. **(D)** Growth competition assay in mouse MLL-AF9 (WT-MA9) cells. Graph shows the relative growth of cells infected with RFP-tagged *Mll4* (*Kmt2d*) sgRNAs measured by flow cytometry (mean±SEM, n=3 infection replicates). sgControl targets a non-genic region in chromosome 8 as negative control. **(E)** Relative percentage of sgUtx-expressing (RFP+) cells over time after transduction of MLL-AF9 cells treated with MI-503 or DMSO. **(F)** Relative percentage of sgMll3-expressing (RFP+) cells over time after transduction of MLL-AF9 cells treated with MI-503 or DMSO. **(G)** Relative percentage of sgMll4-expressing (RFP+) cells over time after transduction of MLL-AF9 cells treated with MI-503 or DMSO.

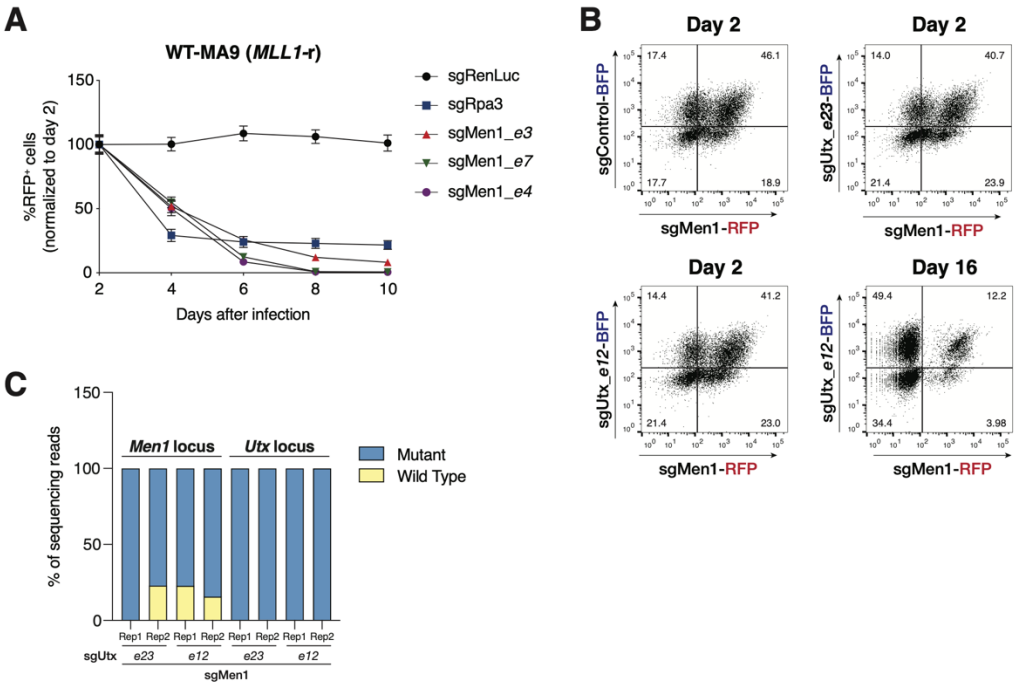

Extended Figure 4. *Utx* deletion rescues the lethality associated with *Men1* deletion. (A) Growth competition assay in mouse MLL-AF9 (WT-MA9) cells. Graph shows the relative growth of cells infected with RFP-tagged *Men1* sgRNAs measured by flow cytometry (mean±SEM, n=3 infection replicates). sgRenilla Luciferase (RenLuc) and sgRpa3 were positive and negative controls, respectively. **(B)** Plots from flow cytometry analysis of leukemia cells co-expressing sgMen1-RFP and sgUtx-BFP (*e12* and *e23*) 2 and 16 days post-infection. **(C)** Amplicon sequencing results of the mouse *Men*1 and *Utx* loci from leukemia cells co-expressing sgMen1 and sgUtx (*e12* and *e23*). R1 and R2 represent two infection replicates for each genotype.

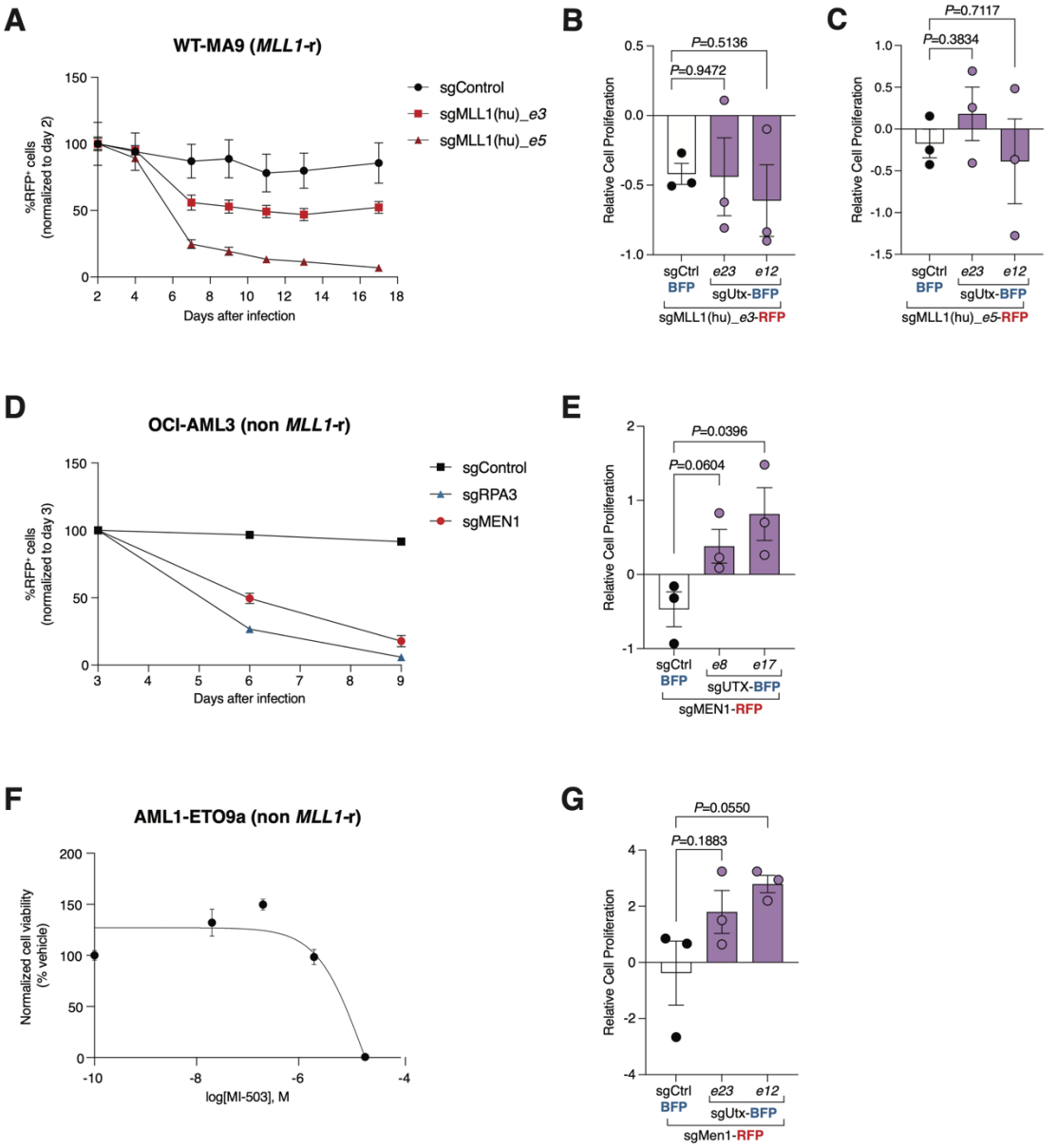

Extended Figure 5. *Men1* and *Utx* epistasis is independent of the MLL-fusion. (A) Growth competition assay in mouse MLL-AF9 (WT-MA9) cells. Graph shows the relative growth of cells infected with RFP-tagged human (hu) *MLL1* (*e3* = exon 3, *e5* = exon 5) sgRNAs measured by flow cytometry (mean±SEM, n=3 infection replicates). **(B)** Differential fitness of mouse WT-MA9 cells is shown as the relative fitness of double positive cells (sgMLL1(hu)_*e3*-RFP + sgUtx-BFP or sgMLL1(hu)_*e3*-RFP + sgControl-BFP) to single positive cells (sgMLL1(hu)_*e3*-RFP) 16 days post-infection measured by flow cytometry (mean±SEM, n=3 infection replicates, *P*-value

calculated by Student's t-test). **(C)** Differential fitness of mouse WT-MA9 cells is shown as the relative fitness of double positive cells (sgMLL1(hu)_*e5*-RFP + sgUtx-BFP or sgMLL1(hu)_*e5*-RFP + sgControl-BFP) to single positive cells (sgMLL1(hu)_*e5*-RFP) 16 days post-infection measured by flow cytometry (mean±SEM, n=3 infection replicates, *P*-value calculated by Student's t-test). **(D)** Growth competition assay in human non *MLL1*-r (OCI-AML3) cells. Graph shows the relative growth of cells infected with RFP-tagged sgRNAs measured by flow cytometry (mean±SEM, n=3 infection replicates). **(E)** Differential fitness of human OCI-AML3 cells is shown as the relative fitness of double positive cells to single positive cells 20 days post-infection measured by flow cytometry (mean±SEM, n=3 infection replicates, *P*-value calculated by Student's t-test). **(F)** Viability of mouse AML1-ETO9a leukemia cells treated with MI-503 for 96 hours. **(G)** Differential fitness of mouse AML1-ETO9a leukemia cells is shown as the relative fitness of double positive cells to single positive cells 15 days post-infection measured by flow cytometry (mean±SEM, n=3 infection replicates, *P*-value calculated by Student's t-test).

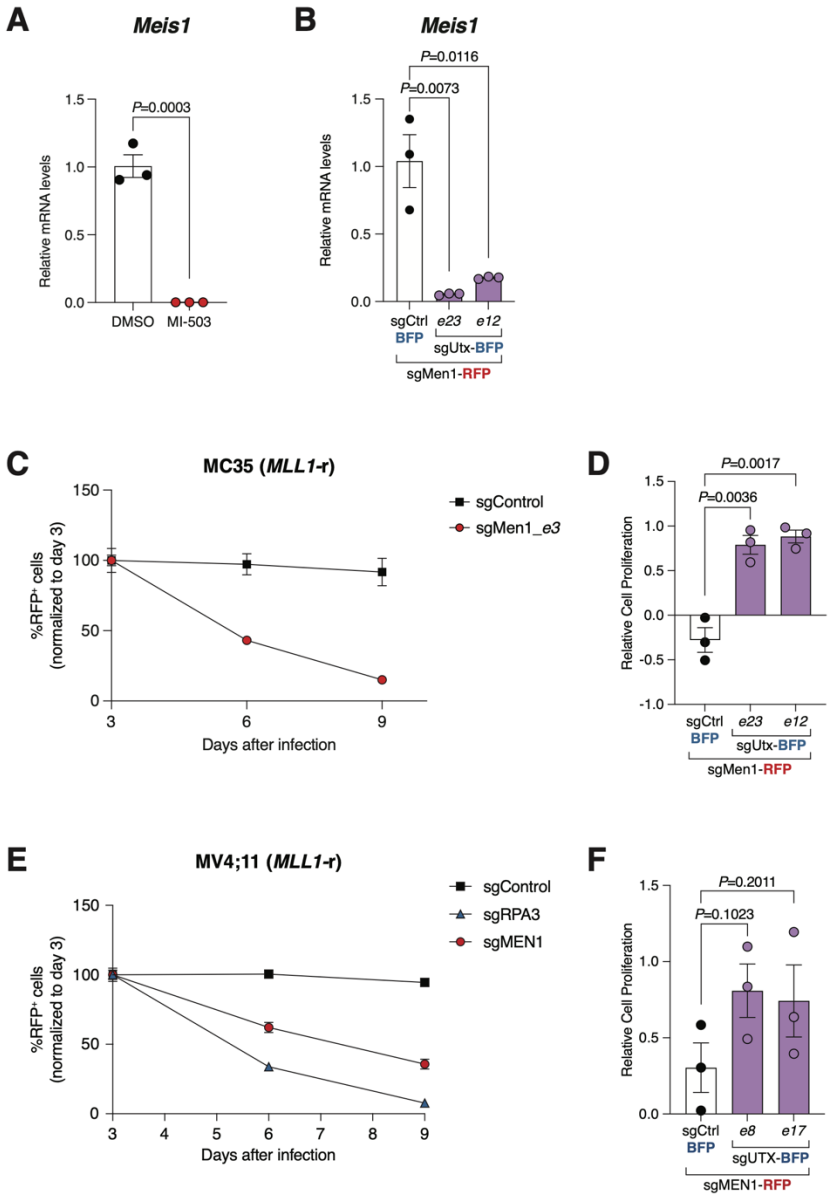

Extended Figure 6. *Meis1* expression is dispensable for proliferation of *Men1^{KO};Utx^{KO}* double-knockout MLL-AF9 leukemia cells. (A) qPCR analysis for *Meis1* expression in mouse MLL-AF9 leukemia cells treated with DMSO (vehicle) or MI-503 for 96 hours (mean±SEM, n=3 replicates, *P*-value calculated by Student's t-test). **(B)** qPCR analysis for *Meis1* expression in mouse MLL-AF9 leukemia cells co-expressing sgMen1-RFP and sgUtx-BFP, or a control sgRNA (mean±SEM, n=3 replicates, *P*-value calculated by Student's t-test). **(C)** Growth competition assay in mouse MLL-AF9 (MC35) cells. Graph shows the relative growth of cells infected with

RFP-tagged sgRNAs (sgControl and sgMen1_*e3*) measured by flow cytometry (mean±SEM, n=3 infection replicates). **(D)** Differential fitness of mouse MC35 cells is shown as the relative fitness of double positive cells (sgMen1-RFP + sgUtx-BFP or sgMen1-RFP + sgControl-BFP) to single positive cells (sgMen1-RFP) 9 days post-infection measured by flow cytometry (mean±SEM, n=3 infection replicates, *P*-value calculated by Student's t-test). **(E)** Growth competition assay in human MLL-AF4 (MV4;11) leukemia cells. Graph shows the relative growth of cells infected with RFP-tagged sgRNAs measured by flow cytometry (mean±SEM, n=3 infection replicates). **(F)** Differential fitness of human MV4;11 leukemia cells is shown as the relative fitness of double positive cells to single positive cells 20 days post-infection measured by flow cytometry (mean±SEM, n=3 infection replicates, *P*-value calculated by Student's t-test).

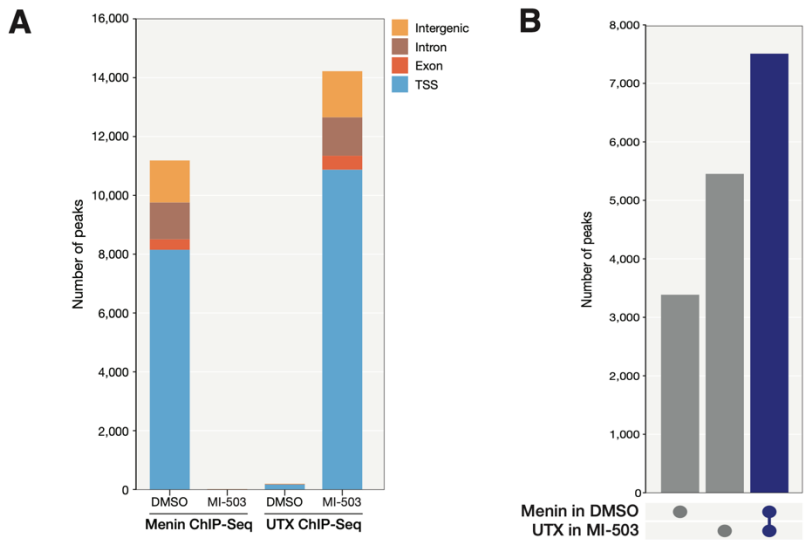

Extended Figure 7. Genomic distribution of Menin and UTX is different in the context of MI-503 treatment. (A) Genomic distribution of Menin and UTX ChIP-Seq peaks from mouse leukemia cells treated with DMSO or MI-503 for 96 hours. **(B)** Upset plot showing a comparison between the genomic distribution of UTX ChIP-Seq peaks in MI-503, the genomic distribution of Menin ChIP-Seq peaks in DMSO, and the overlap between UTX ChIP-Seq peaks in MI-503 and Menin ChIP-Seq peaks in DMSO.

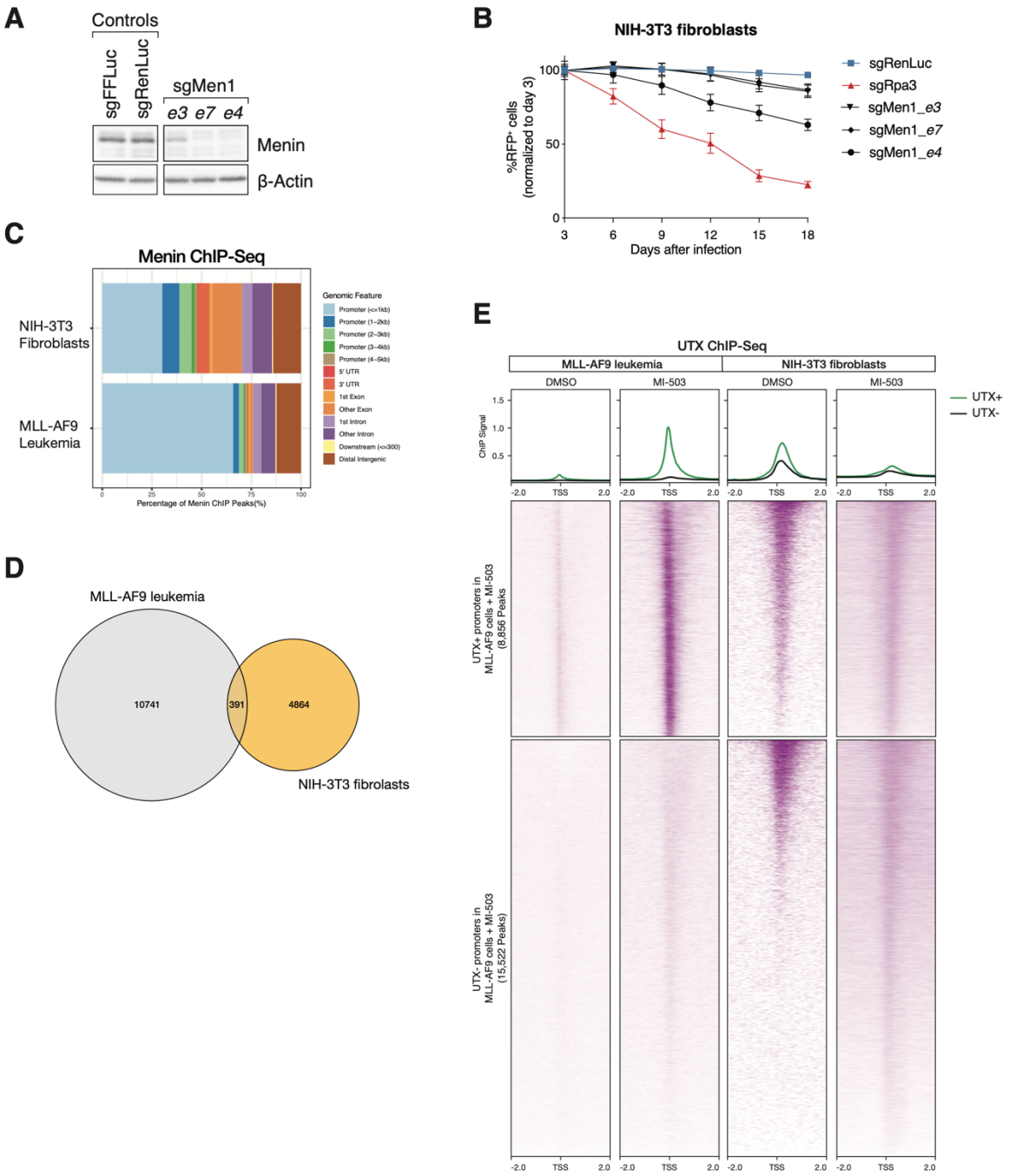

Extended Figure 8. Menin-independent mammalian cells do not exhibit chromatin changes associated with the Menin-UTX molecular switch. (A) Western blot analysis of Cas9-expressing mouse fibroblast (NIH-3T3) cells expressing different controls and *Men1* sgRNAs. **(B)** Growth competition assay in mouse fibroblast cells. Graph shows the relative growth of cells infected with RFP-tagged sgRNAs measured by flow cytometry (mean±SEM, n=3 infection

replicates). **(C)** Genomic distribution of Menin ChIP-Seq peaks from mouse fibroblasts (top) or mouse MLL-AF9 leukemia cells (bottom). **(D)** Venn diagram comparing the number of Menin peaks detected in mouse MLL-AF9 leukemia cells versus NIH-3T3 fibroblasts. **(E)** Heatmaps displaying UTX (purple) ChIP-Seq signals mapping to a 4-kb window around TSSs. Data is shown for mouse MLL-AF9 cells (left) and NIH-3T3 mouse fibroblasts (right) treated with DMSO or MI-503 for 96 hours. Metaplot represents the average ChIP-Seq signal for UTX at promoters that are known to be bound by UTX (green) or not (black) in MLL-AF9 cells treated with MI-503.

A

Overlap Menin (DMSO) and UTX (MI-503) in MLL-AF9 leukemia

Rank	Motif	Name	*P*-value	% of Target	% of Background
1		**NFY**	$1e^{-130}$	44.97%	9.13%
2		Sp5	$1e^{-63}$	54.14%	23.85%
3		Sp1	$1e^{-50}$	32.69%	11.10%
4		KLF5	$1e^{-45}$	50.74%	25.05%
5		KLF14	$1e^{-41}$	59.47%	33.75%

B

Menin ChIP in NIH-3T3 fibroblasts

Rank	Motif	Name	*P*-value	% of Target	% of Background
1		CBF1	$1e^{-69}$	41.25%	1.86%
2		ARG80	$1e^{-69}$	40.62%	1.76%
3		TBX5	$1e^{-67}$	43.12%	2.35%
4		TEIL	$1e^{-64}$	42.50%	2.45%
5		HLH-2	$1e^{-62}$	40.00%	2.12%

C

UTX ChIP in NIH-3T3 fibroblasts

Rank	Motif	Name	*P*-value	% of Target	% of Background
1		VND	$1e^{-19}$	0.48%	0.00%
2		GFI1	$1e^{-16}$	0.43%	0.00%
3		RLR1	$1e^{-16}$	0.43%	0.00%
4		HOX2A	$1e^{-16}$	0.43%	0.00%
5		ARID5A	$1e^{-16}$	0.48%	0.00%

D

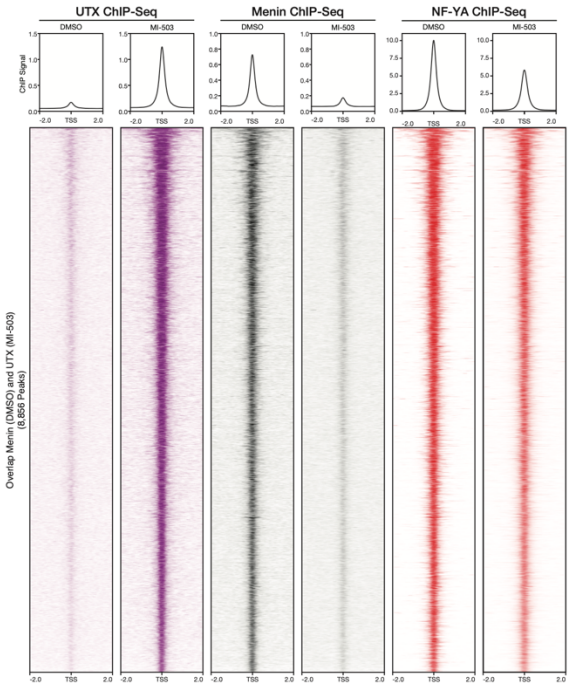

E

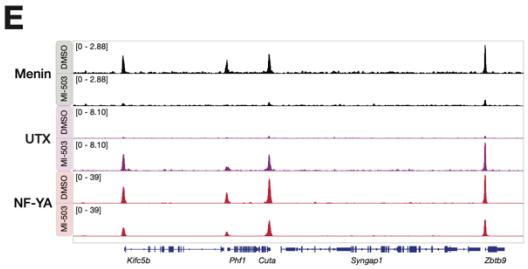

F

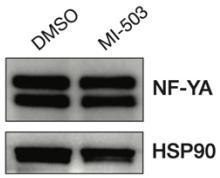

Extended Figure 9. NF-Y restricts chromatin occupancy of UTX at promoter regions. (A) Motif analysis of overlapping ChIP-Seq peaks between Menin (DMSO) and UTX (MI-503) in mouse MLL-AF9 leukemia cells. **(B)** Motif analysis of Menin ChIP-Seq peaks detected in NIH-3T3 mouse fibroblasts. **(C)** Motif analysis of UTX ChIP-Seq peaks detected in NIH-3T3 mouse fibroblasts. **(D)** Heatmaps displaying UTX (purple), Menin (black), and NF-YA (red) ChIP-Seq signals mapping to a 4-kb window around TSSs. Data is shown for DMSO and MI-503-treated cells for 96 hours. Metaplot represents the average ChIP-Seq signal for each protein at promoters. **(E)** Genome browser representation of ChIP-Seq normalized reads (average RPKM) for representative loci bound by Menin (black), UTX (purple), and NF-YA (red) in cells treated with

DMSO or MI-503 for 96 hours. **(F)** Western blot analysis of NF-YA and HSP90 proteins (loading control) upon MI-503 treatment of mouse MLL-AF9 leukemia cells after 96 hours.

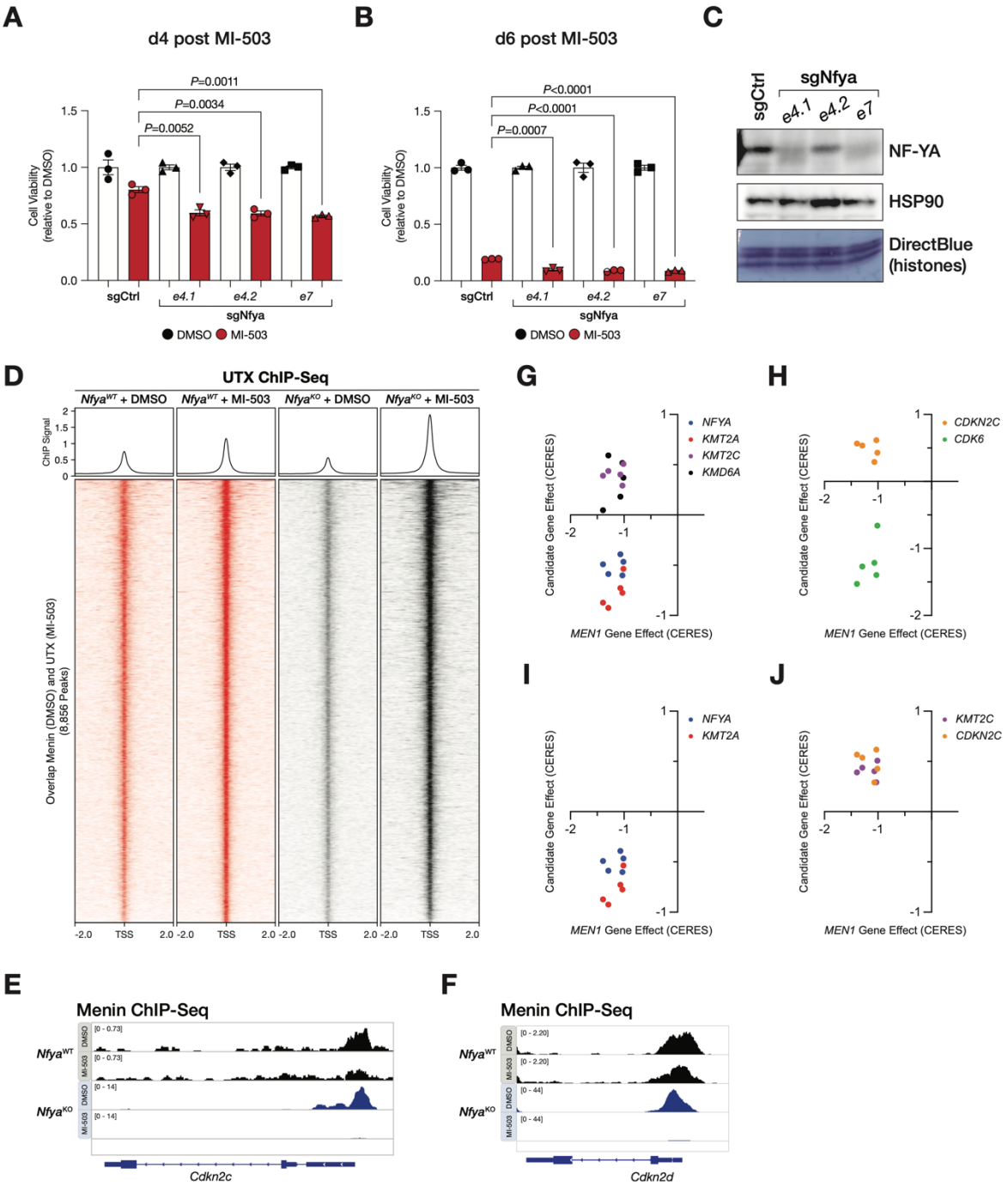

Extended Figure 10. NF-Y facilitates promoter regulation by Menin. (A) Cell viability assay from cells treated with DMSO (vehicle, black) or MI-503 (red) after 4 days (mean±SEM, n=3 infection replicates, *P*-value calculated by Student's t-test). sgCtrl, control sgRNA targeting a non-genic region on chromosome 8. **(B)** Cell viability assay from cells treated with DMSO (vehicle,

black) or MI-503 (red) after 6 days (mean±SEM, n=3 infection replicates, *P*-value calculated by Student's t-test). sgCtrl, control sgRNA targeting a non-genic region on chromosome 8. **(C)** Western blot analysis of NF-YA and HSP90 proteins (loading control) in mouse MLL-AF9 leukemia cells transduced with a control sgRNA (sgCtrl) or three independent *Nfya*-targeting sgRNAs. Direct blue staining of histones (bottom) serves as an additional loading control. **(D)** Heatmaps displaying UTX ChIP-Seq signals mapping to a 4-kb window around TSSs in $Nfya^{WT}$ (red) or $Nfya^{KO}$ (black) MLL-AF9 leukemia cells treated with DMSO or MI-503 for 96 hours. Metaplot represents the average ChIP-Seq signal for each protein at promoters. **(E) - (F)** Genome browser representation of Menin ChIP-Seq normalized reads (average RPKM) for representative loci bound by Menin in $Nfya^{WT}$ (black) or $Nfya^{KO}$ (blue) MLL-AF9 leukemia cells treated with DMSO or MI-503 for 96 hours. **(G)** Co-essentiality scatter plot showing relationship between *MEN1* loss-of-function and dependency to *NFYA*, *MLL1* (*KMT2A*), *MLL3* (*KMT2C*), and *UTX* (*KDM6A*). **(H)** Co-essentiality scatter plot showing relationship between *MEN1* loss-of-function and dependency to *CDKN2C* and *CDK6*. **(I)** Co-essentiality scatter plot showing relationship between *MEN1* loss-of-function and dependency to *NFYA* and *MLL1* (*KMT2A*). **(J)** Co-essentiality scatter plot showing relationship between *MEN1* loss-of-function and dependency to *MLL3* (*KMT2C*) and *CDKN2C*.

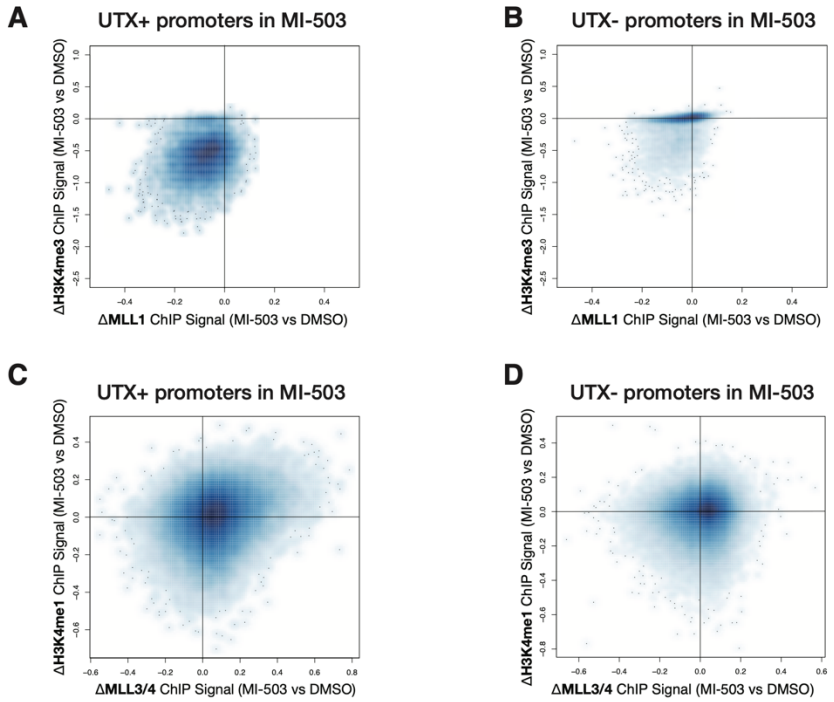

Extended Figure 11. Disruption of Menin-MLL1 leads to targeting of MLL3/4-UTX to sites normally bound by the MLL1-Menin complex. (A) Density plot showing correlation between H3K4me3 and MLL1 ChIP-Seq signals (MI-503 vs DMSO). Signals correspond to summed signal ±2kb around TSSs that overlap with UTX peaks in MI-503 condition. **(B)** Density plot showing correlation between H3K4me3 and MLL1 ChIP-Seq signals (MI-503 vs DMSO). Signals correspond to summed signal ±2kb around TSSs that do not overlap with UTX peaks in MI-503 condition. **(C)** Density plot showing correlation between H3K4me1 and MLL3/4 ChIP-Seq signals (MI-503 vs DMSO). Signals correspond to summed signal ±2kb around TSSs that overlap with UTX peaks in MI-503 condition. **(D)** Density plot showing correlation between H3K4me1 and MLL3/4 ChIP-Seq signals (MI-503 vs DMSO). Signals correspond to summed signal ±2kb around TSSs that do not overlap with UTX peaks in MI-503 condition.

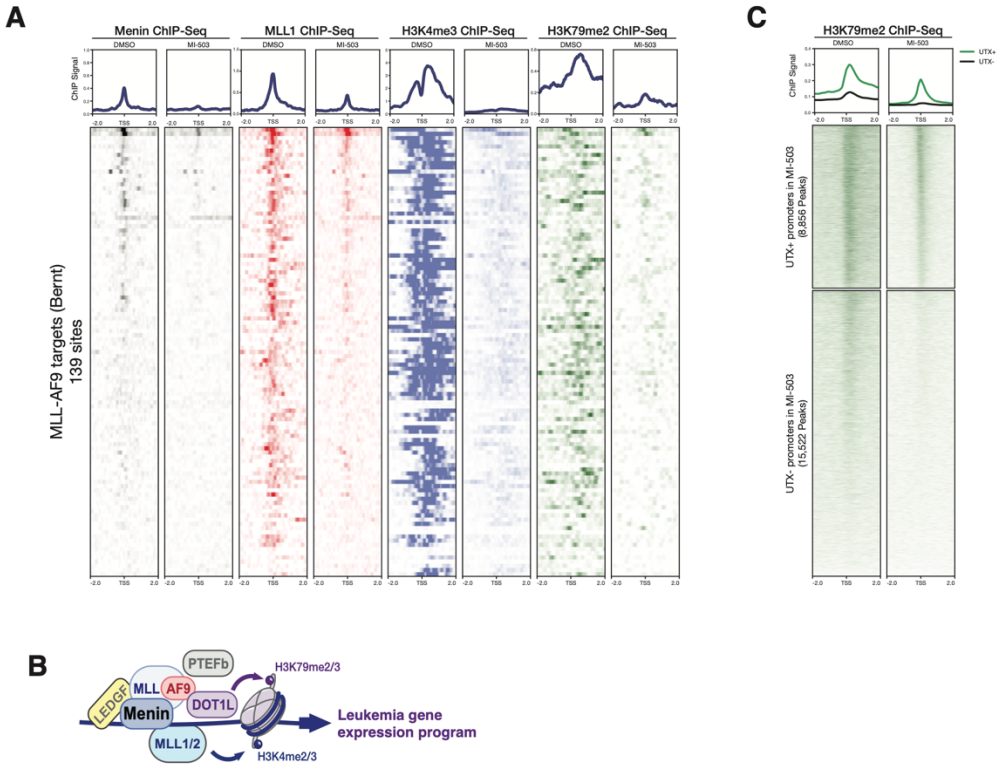

Extended Figure 12. MLL1-Menin targets are distinct genomic loci from MLL-FP targets. **(A)** Heatmaps displaying Menin (black), MLL1 (red), H3K4me3 (blue), and H3K79me2 (green) ChIP-Seq signals mapping to MLL-AF9 target loci (139 sites) from MLL-AF9 leukemia cells treated with DMSO or MI-503 for 96 hours. Metaplot represents the average ChIP-Seq signal for each protein at promoters. **(B)** Schematic representation of ectopic chromatin complexes that are formed by MLL-FPs. **(C)** Heatmaps displaying H3K79me2 ChIP-Seq signals mapping to a 4-kb window around TSSs in MLL-AF9 leukemia cells treated with DMSO or MI-503 for 96 hours. Metaplot represents the average ChIP-Seq signal for H3K79me2 at promoters that are known to be bound by UTX (green) or not (black) in MLL-AF9 cells treated with MI-503.

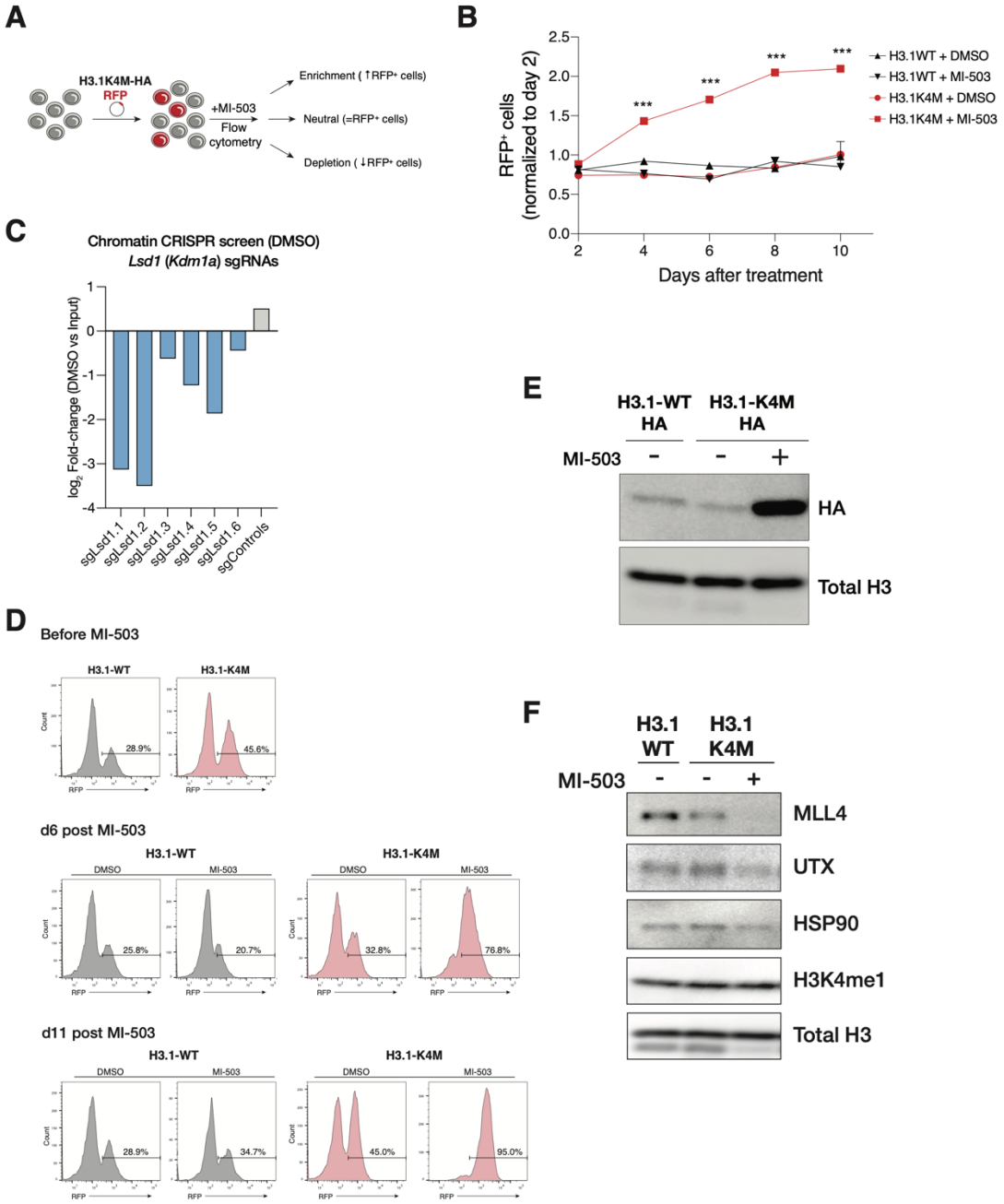

Extended Figure 13. Destabilization of the MLL3/4-UTX complex is sufficient to blunt cellular responses to Menin-MLL inhibition. (A) Layout of growth competition assay to assess the effects of expressing a H3.1K4M mutation in MLL-AF9 leukemia cells in response to Menin-MLL inhibition. **(B)** Relative percentage of RFP+ transgene (H3.1WT or H3.1K4M) cells over time after transduction of MLL-AF9 cells treated with MI-503 or DMSO (mean±SD, n=3 replicates, *P*-value calculated by Student's t-test, $P < 0.001$ = ***). **(C)** Log_2-fold change of individual

Lsd1(Kdm1a)-targeting sgRNAs from DMSO-treated vs Input (T0) cells. Note that LSD1 (also known as KDM1A) is a histone H3K4me1/2 demethylase. **(D)** Expression of H3.1WT-RFP or H3.1K4M-RFP in mouse MLL-AF9 leukemia cells treated with DMSO or MI-503 was monitored over time by flow cytometry. **(E)** Western blot analysis of HA-tag from MLL-AF9 leukemia cells expressing H3.1WT-HA or H3.1K4M-HA and treated with DMSO or MI-503 for 6 days. **(F)** Western blot analysis of MLL4, UTX, HSP90 (loading control), H3K4me1, and total H3 (loading control) from MLL-AF9 leukemia cells expressing H3.1WT or H3.1K4M and treated with DMSO or MI-503 for 6 days.

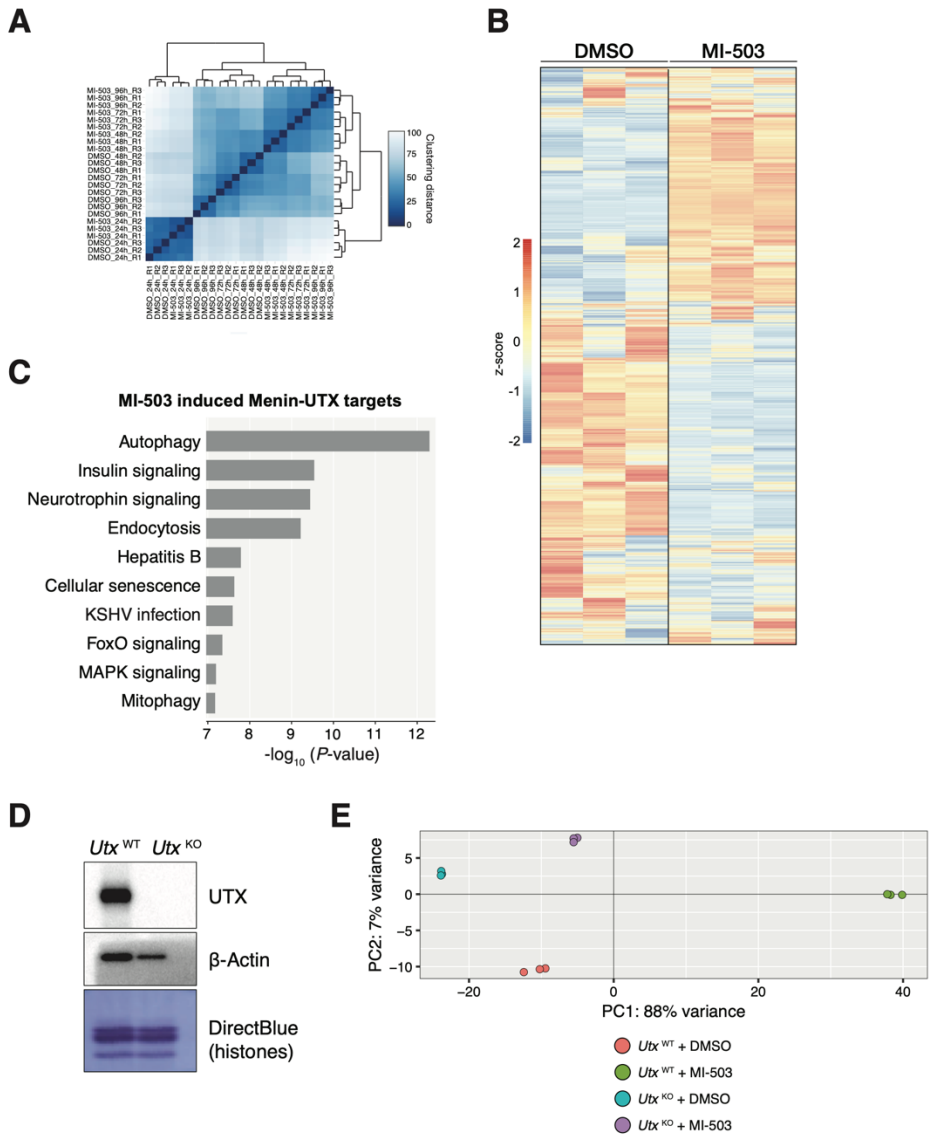

Extended Figure 14. Transcriptional assessment of *Utx*-deficient MLL-AF9 leukemia cells. **(A)** Heatmap showing the Pearson correlation between mouse MLL-AF9 leukemia samples treated with DMSO or MI-503 at different time points, and following normalization of gene expression across samples as measured by RNA-Seq. **(B)** Heatmap showing differential gene expression in mouse MLL-AF9 leukemia cells treated with DMSO or MI-503 for 96 hours, as measured by RNA-Seq. **(C)** Gene ontology (GO) analysis of Menin-UTX targets using RNA-Seq data from MLL-AF9 leukemia cells treated with DMSO or MI-503 for 96 hours. Top 10 GO categories based on statistical significance are shown. **(D)** Western blot analysis of UTX and β-

actin (loading control) from *Utx*^{WT} and *Utx*^{KO} mouse MLL-AF9 leukemia cells. **(E)** Principal component analysis (PCA) using RNA-Seq gene expression data from *Utx*^{WT} and *Utx*^{KO} cells treated with DMSO or MI-503 for 96 hours.

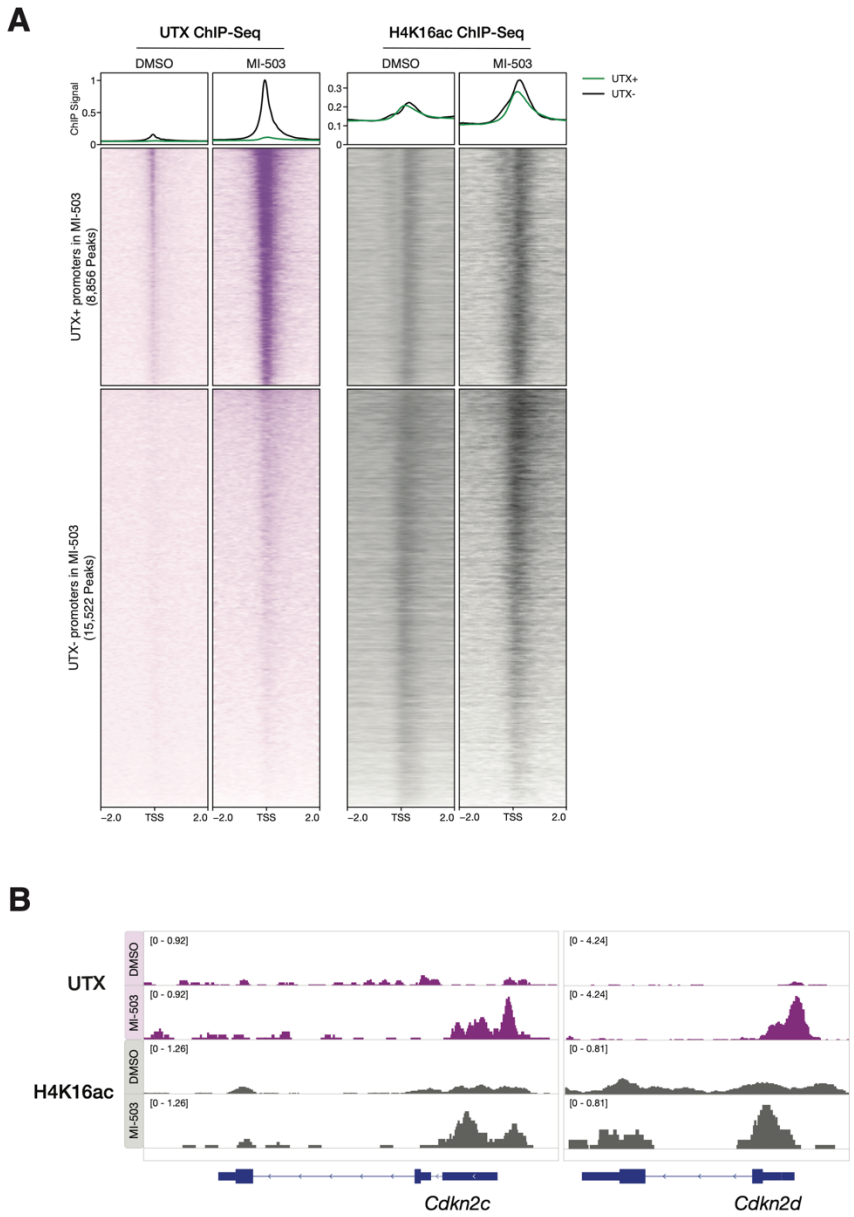

Extended Figure 15. Induction of the Menin-UTX molecular switch upon Menin-MLL1 inhibition in human leukemia cells. (A) Heatmaps displaying UTX (purple) or H4K16ac (black) ChIP-Seq signals mapping to a 4-kb window around TSSs in MLL-AF9 leukemia cells treated with DMSO or MI-503 for 96 hours. Metaplot represents the average ChIP-Seq signal for each protein at promoters that are known to be bound by UTX (green) or not (black) in mouse MLL-AF9 leukemia cells treated with MI-503 for 96 hours. **(B)** Genome browser representation of ChIP-Seq

normalized reads (average RPKM) for UTX (purple) or H4K16ac (grey) at *Cdkn2c* and *Cdkn2d* loci from MLL-AF9 cells treated with DMSO or MI-503 for 96 hours.

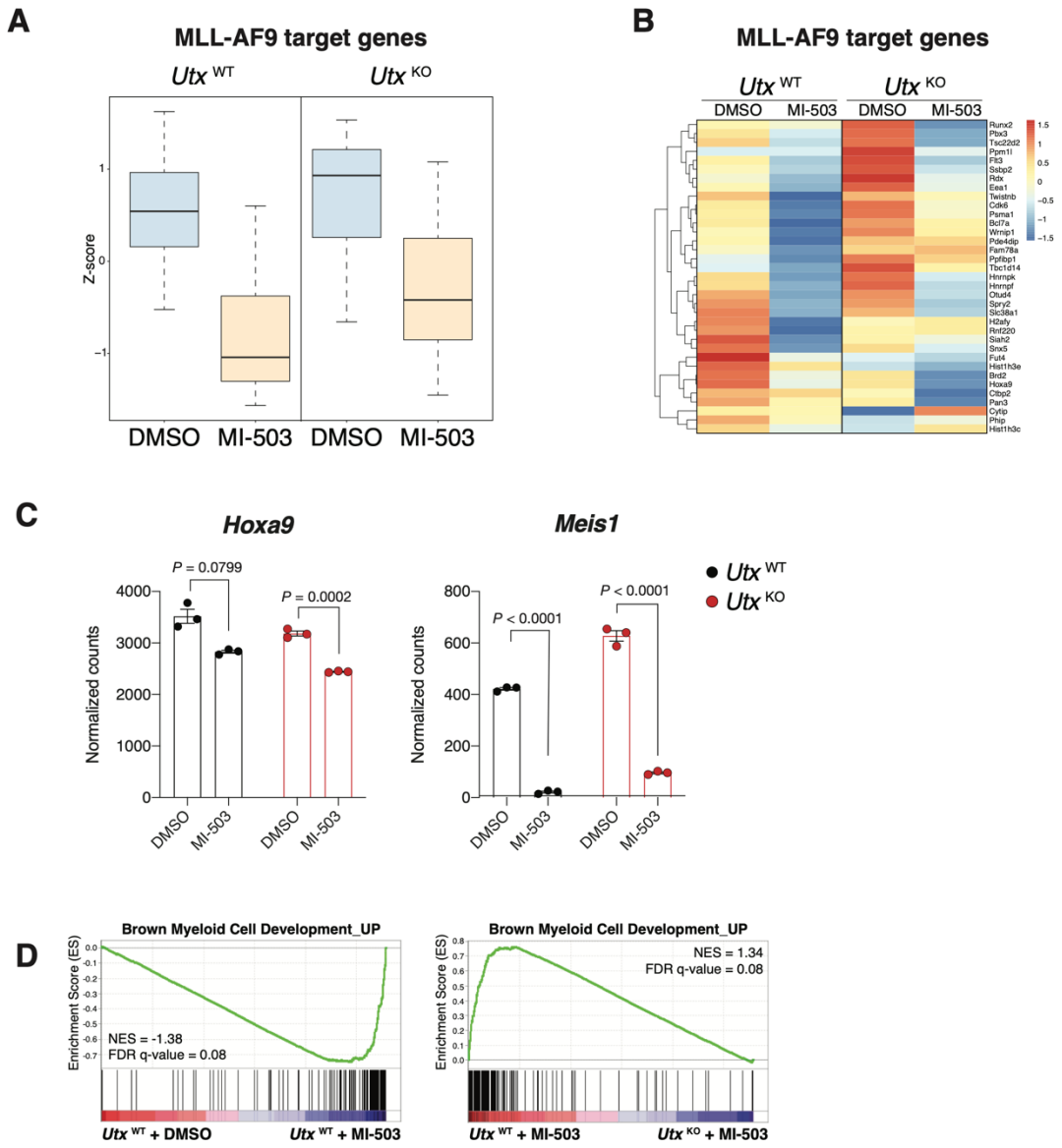

Extended Figure 16. MLL-AF9 target genes are not regulated by the Menin-UTX molecular switch. (A) Boxplot showing expression levels of MLL-AF9 target genes, which are suppressed by the MI-503 treatment after 96 hours. Expression levels are shown for *Utx*^{WT} (left panel) and *Utx*^{KO} (right panel) mouse leukemia cells. **(B)** Heatmap of Z-scores for expression of MLL-AF9 target genes from *Utx*^{WT} and *Utx*^{KO} leukemia cells treated with DMSO or MI-503 for 96 hours. **(C)** Mean normalized read counts for MLL-AF9 target genes *Hoxa9* (left) and *Meis1* (right) across three RNA-Seq replicate samples from *Utx*^{WT} and *Utx*^{KO} leukemia cells treated with DMSO or MI-503 for 96 hours. **(D)** GSEA plots showing changes in regulation of myeloid cell differentiation in

genes induced by MI-503 after 96 hours. FDR, false discovery rate; NES, normalized enrichment score.

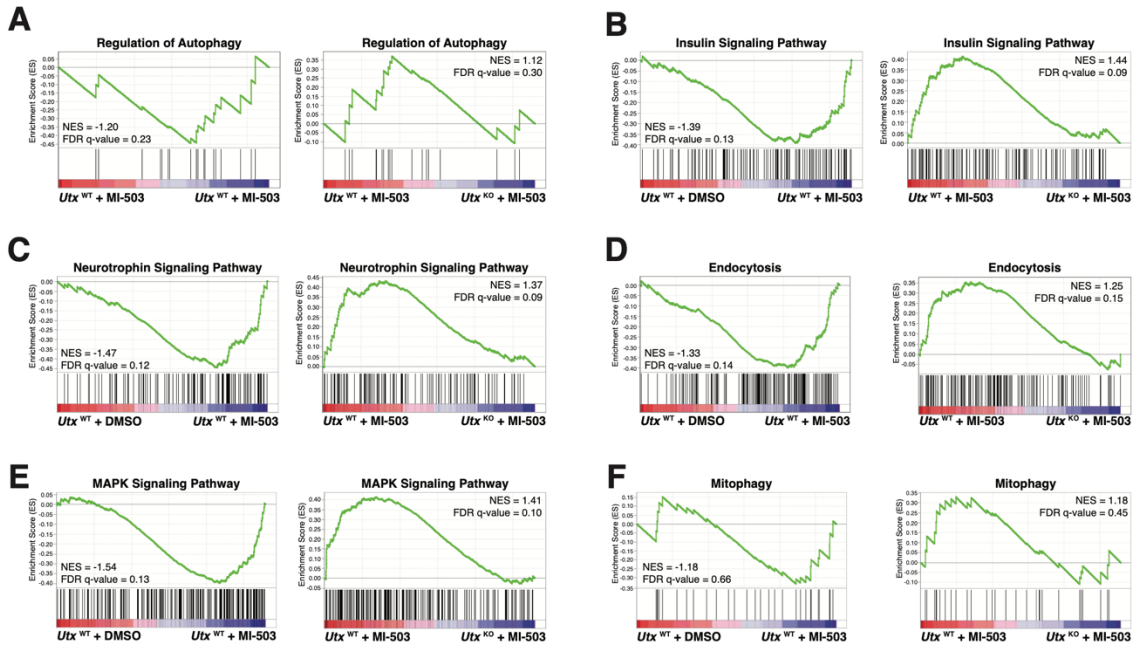

Extended Figure 17. GSEA analysis of Menin-UTX target genes. (A) GSEA plots showing changes in regulation of autophagy genes induced by MI-503 treatment after 96 hours. FDR, false discovery rate; NES, normalized enrichment score. **(B)** GSEA plots showing changes in insulin signaling pathway genes induced by MI-503 treatment after 96 hours. **(C)** GSEA plots showing changes in neurotrophin signaling pathway genes induced by MI-503 treatment after 96 hours. **(D)** GSEA plots showing changes in endocytosis genes induced by MI-503 treatment after 96 hours. **(E)** GSEA plots showing changes in MAPK signaling pathway genes induced by MI-503 treatment after 96 hours. **(F)** GSEA plots showing changes in mitophagy genes induced by MI-503 treatment after 96 hours.

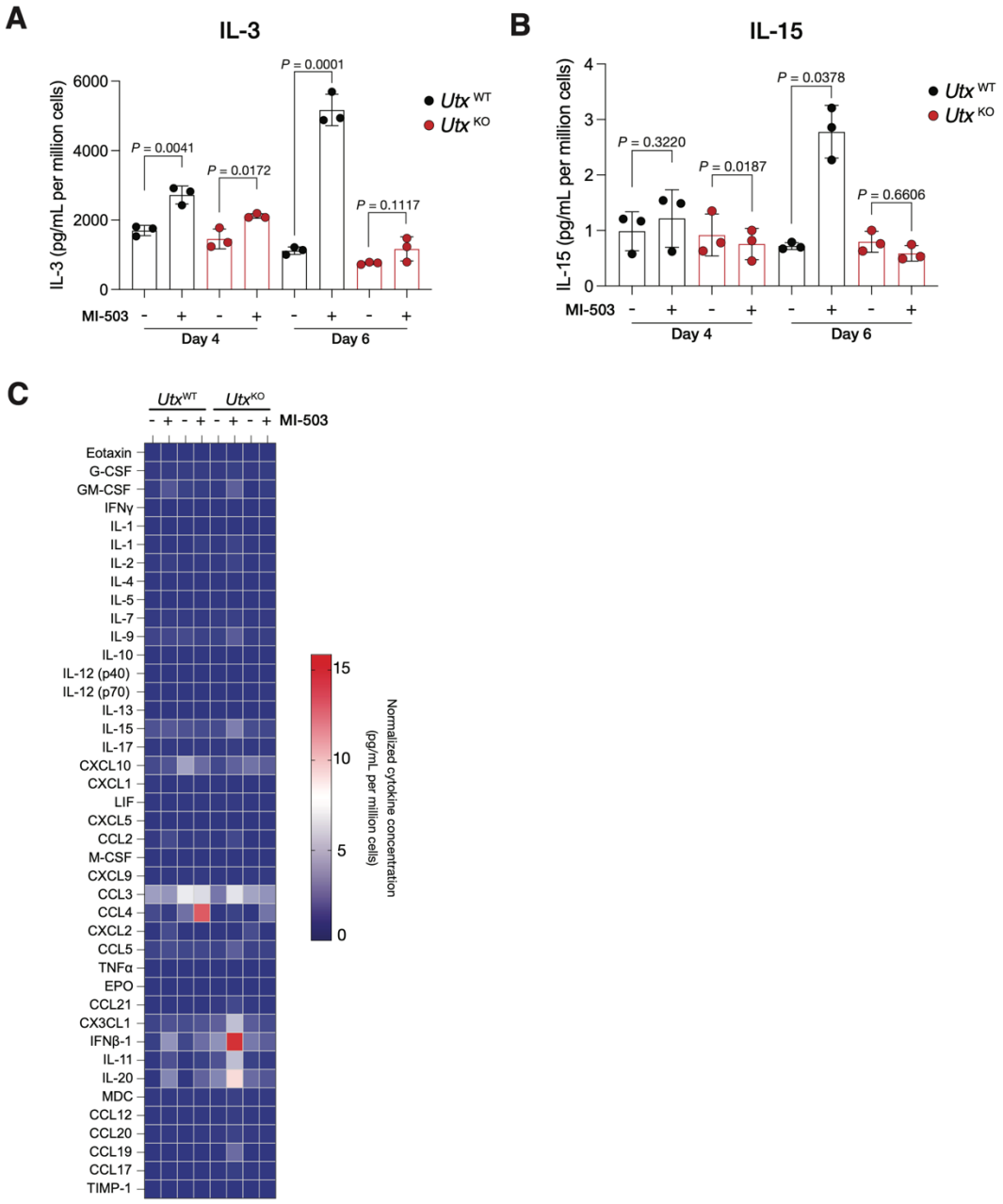

Extended Figure 18. MLL3/4-UTX-dependent induction of SASP cytokines upon Menin-MLL inhibition. (A) Secreted levels of IL-3 in *Utx*^{WT} and *Utx*^{KO} MLL-AF9 leukemia cells treated with Menin inhibitor (MI-503) or vehicle (DMSO) after four or six days. Data are quantified as pg/mL of secreted cytokine per million cells and represent the mean of three biological replicates. **(B)** Secreted levels of IL-15 in *Utx*^{WT} and *Utx*^{KO} MLL-AF9 leukemia cells treated with Menin inhibitor (MI-503) or vehicle (DMSO) after four or six days. Data are quantified as pg/mL of secreted

cytokine per million cells and represent the mean of three biological replicates. **(C)** Heat map of cytokine array results from *Utx*^{WT} and *Utx*^{KO} MLL-AF9 leukemia cells treated with Menin inhibitor (MI-503) or vehicle (DMSO) after four or six days. Data are quantified as pg/mL of secreted cytokine per million cells and represent the mean of three biological replicates. Note that the very high levels of IFNβ-1 secretion relative to the rest of the cytokines measured affect the dynamic range of data visualization.

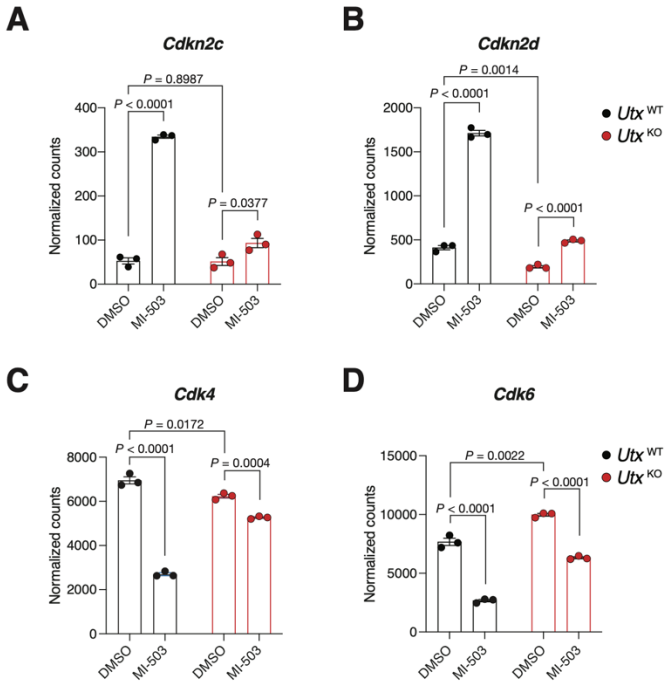

Extended Figure 19. Induction of the Menin-UTX molecular switch regulates expression of the CDK inhibitors *Cdkn2c/d*. (A) - (B) Mean normalized read counts of the cyclin-dependent kinases inhibitors, *Cdkn2c* and *Cdkn2d*, across three RNA-Seq replicate samples from *Utx*^{WT} (black) and *Utx*^{KO} (red) leukemia cells treated with DMSO or MI-503 for 96 hours. **(C) - (D)** Mean normalized read counts of the cyclin-dependent kinases, *Cdk4* and *Cdk6*, across three RNA-Seq replicate samples from *Utx*^{WT} (black) and *Utx*^{KO} (red) leukemia cells treated with DMSO or MI-503 for 96 hours.

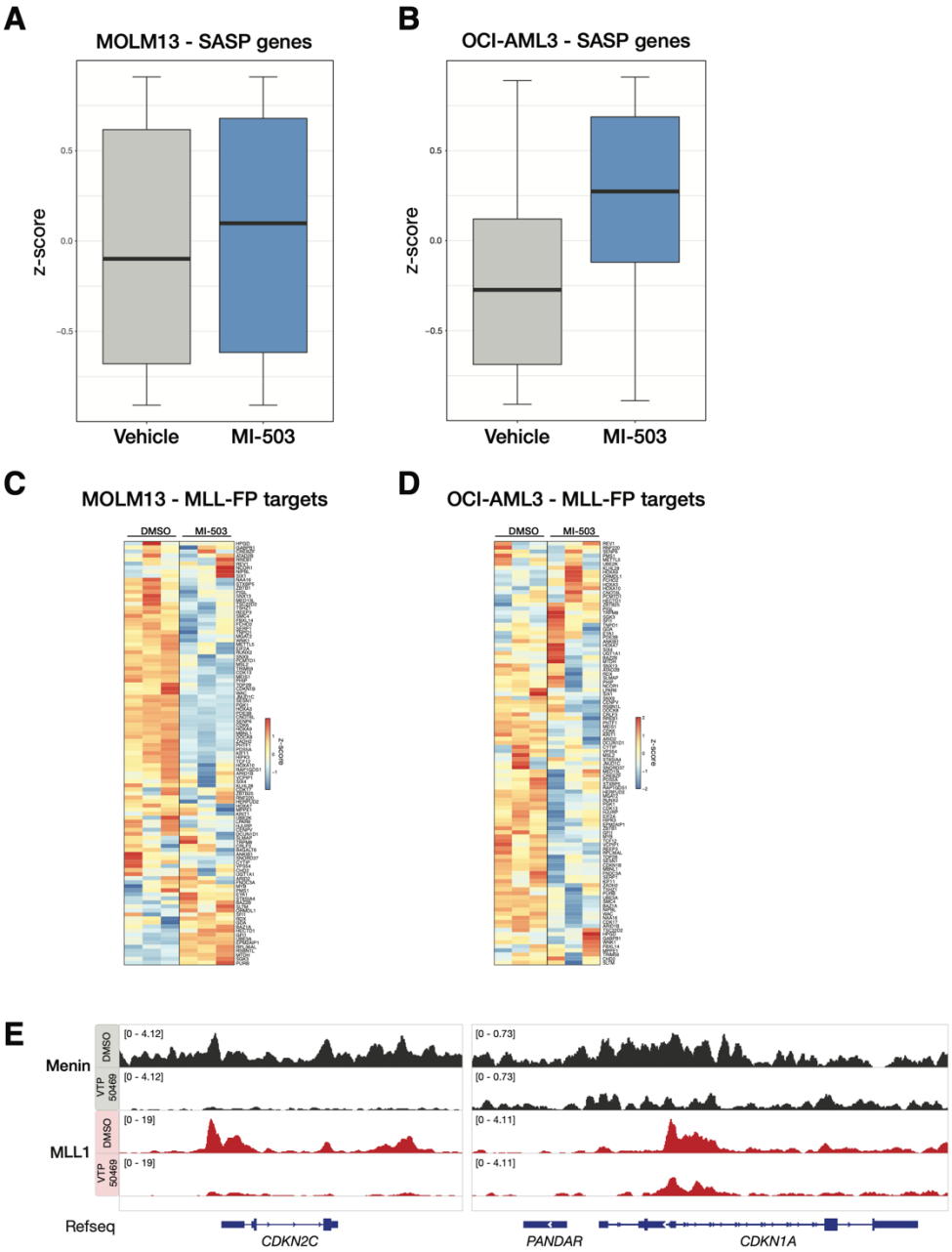

Extended Figure 20. Induction of the Menin-UTX molecular switch upon Menin-MLL1 inhibition in human leukemia cells. (A) Boxplot showing expression levels of SASP genes in MOLM13 human leukemia cells treated with DMSO or MI-503 for 96 hours. **(B)** Boxplot showing expression levels of SASP genes in OCI-AML3 human leukemia cells treated with DMSO or MI-503 for 96 hours. **(C)** Heatmap of Z-scores for expression of MLL-FP target genes from MOLM13 human leukemia cells treated with DMSO or MI-503 for 96 hours. **(D)** Heatmap of Z-scores for

expression of MLL-FP target genes from MOLM13 human leukemia cells treated with DMSO or MI-503 for 96 hours. **(E)** Genome browser representation of ChIP-Seq normalized reads (average RPKM) for Menin (black) or MLL1 (red) at *CDKN2C* and *CDKN1A* loci from MOLM13 human leukemia cells treated with DMSO or VTP-50469 for 7 days.

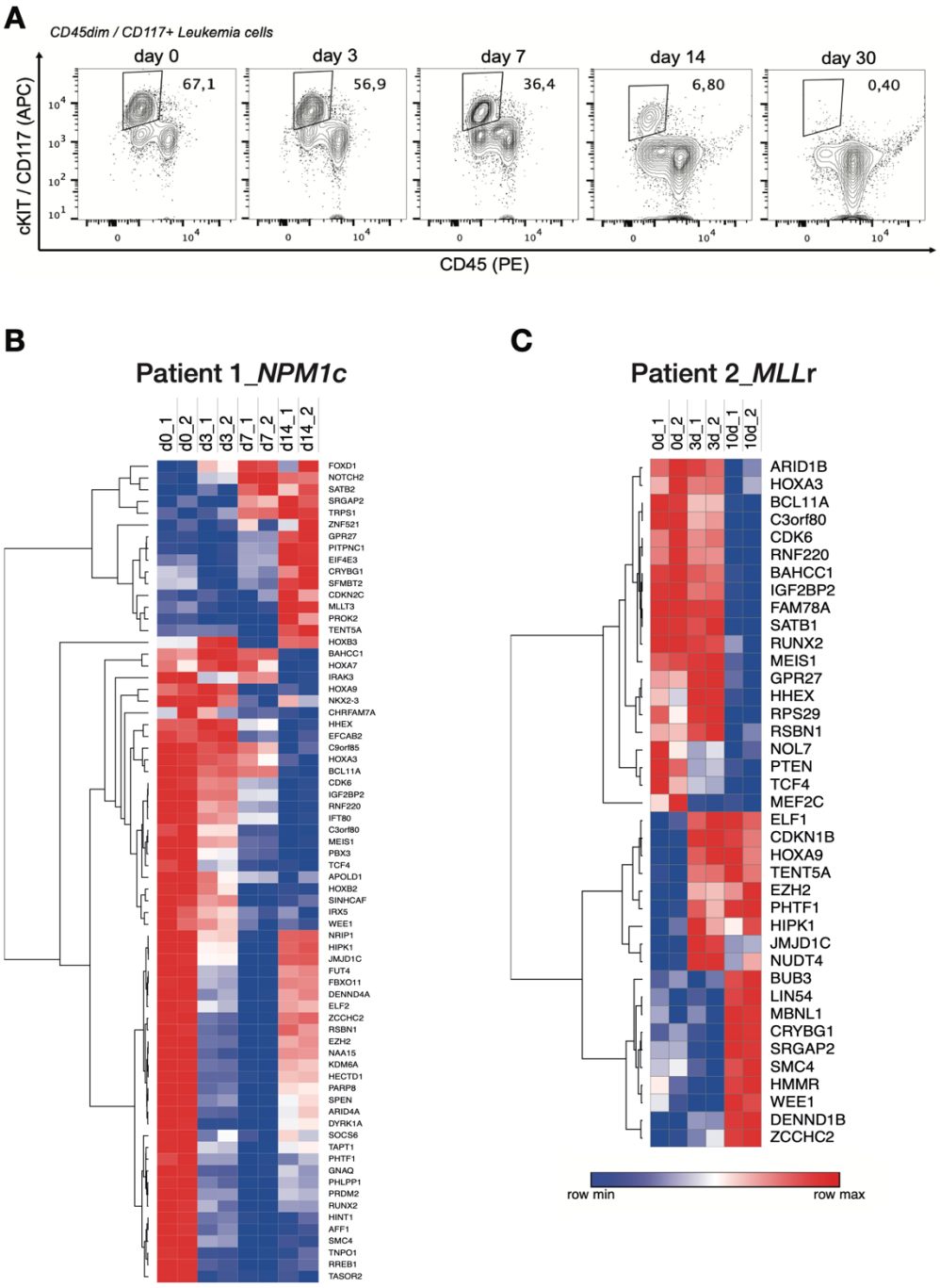

Extended Figure 21. Primary human AML samples from patients participating in the Syndax Phase I Menin-MLL inhibitor trial. (A) Immunophenotyping of primary human AML cells isolated from Patient 1 (*NPM1c* mutant AML) during treatment cycle 1 of SDNX-5613 as part of the AUGMENT-101 clinical trial (NCT04065399). **(B)** Heatmap representation of Z-scores from longitudinal gene expression analysis of AML cells derived from Patient 1 (*NPM1c*-mutant AML)

treated with SNDX-5613. **(C)** Heatmap representation of Z-scores from longitudinal gene expression analysis of AML cells derived from Patient 2 (*MLL*-rearranged AML) treated with SNDX-5613 as part of the AUGMENT-101 clinical trial (NCT04065399).

A

PDX Sample	*MLL*-r	*MLL3* status
DFAM68555	MLL-AF9	wild-type
MSK042D	MLL-AF4	mutant

B

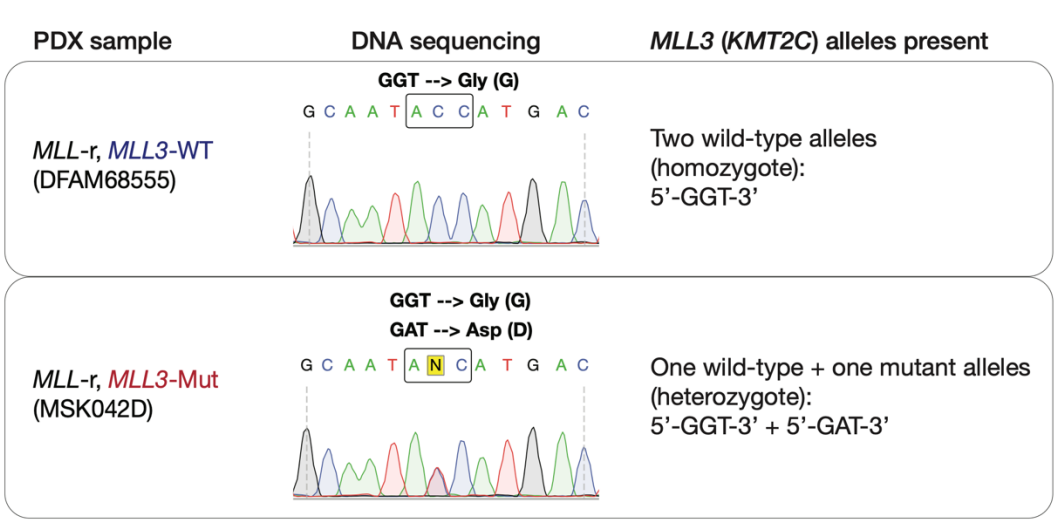

Extended Figure 22. Modeling Menin-MLL inhibitor responses in patient-derived xenografts. (A) Characteristics of PDX samples analyzed in this study. **(B)** DNA sequencing-based validation of *MLL3* status in PDX samples.

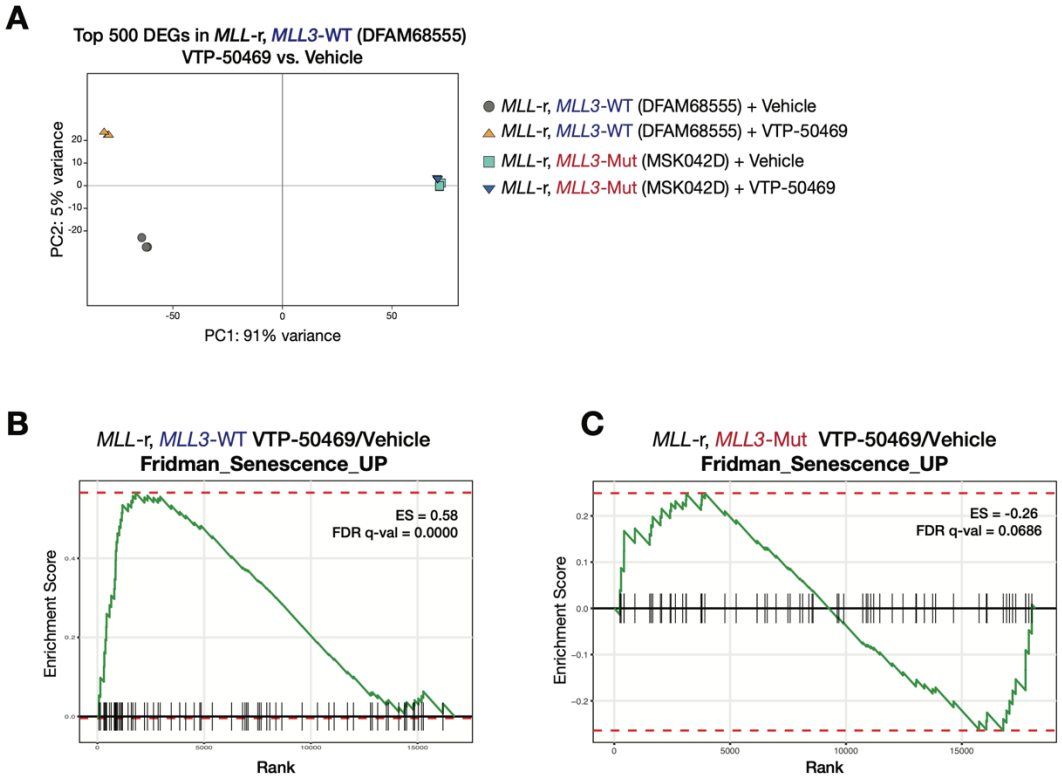

Extended Figure 23. Transcriptional characterization of Menin-MLL inhibitor response in patient-derived xenografts. (A) PCA using RNA-Seq gene expression data obtained from *MLL3*-WT (DFAM68555) and *MLL3*-Mutant (MSK042D) PDX samples treated with DMSO or VTP-50469. PCA was performed using the top 500 differentially-expressed genes upon treatment of *MLL3*-WT PDXs with VTP-50469. Note that *MLL3*-Mutant PDX samples are virtually overlapping independent of the condition, suggesting that the induction of the Menin-UTX molecular switch is impaired in the context of *MLL3* mutation. **(B)** GSEA showing that Menin-MLL inhibition using VTP-50469 leads to induction of cellular senescence in *MLL3*-WT PDX. **(C)** GSEA showing that Menin-MLL inhibition using VTP-50469 fails to induce cellular senescence in *MLL3*-Mutant PDX.